Three-dimensional dose verification of adaptive radiotherapy at an MR-linac

A thesis submitted for the degree of
Doctor of Philosophy

Filipa Alexandra Pina Barrento da Costa

Joint Department of Physics

The Institute of Cancer Research and
The Royal Marsden NHS Foundation Trust

University of London

I, Filipa Alexandra Pina Barrento da Costa, confirm that the work presented in this thesis is my own. Where information has been derived from other sources, I confirm that this has been indicated in the work.

Abstract

The vision of accurate real-time image-guided radiotherapy (RT) has led to the development of MR-Linacs consisting of MRI scanners integrated within RT treatment units. The safe clinical operation of these devices requires to calculate and verify complex clinical dose distributions in patients exposed to the static magnetic field of the MR-scanner. The effects of the magnetic field on patient dose are particularly pronounced at tissue-air interfaces where an increase in dose occurs due to the electron return effect (ERE). State of the art Monte-Carlo (MC) dose calculation algorithms account for this effect, and form the basis for the implementation of unprecedented on-line adaptive treatment strategies. Of particular concern are the treatment sites involving the lung and the pelvic region where the ERE can impact significantly on the dose. In this thesis, I have developed 3D-dosimetry techniques based on PRESAGE® dosimeters for the validation of these novel techniques.

In contrast to most conventional radiation detectors, this dosimeter is not affected by the magnetic field and provides uncompromised 3D dose information, suitable for end-to-end testing of adaptive workflows in MRI-guided RT. The hitherto inability of retrieving dose using the 3D dosimeters periphery was solved, enabling for the first time, measuring the ERE in 3D and benchmarking the results with MC calculations. By exploiting the full volume of PRESAGE® dosimeters and using a commercial phantom, I developed a reproducible and versatile methodology that was easily adapted to perform a variety of tests at the Elekta MR-linac. Different treatment sites and clinically available workflows were assessed, and excellent 3D agreement between calculations and measurements

confirmed their correct implementation. With the same methodology, I performed the first dose verification of MLC-tracked RT at the Elekta MR-linac.

Acknowledgements

This thesis would not have been possible without the help and support of numerous people to whom I want to express my gratitude.

Firstly, I am very grateful for the help provided by my supervisors. To Uwe Oelfke, for his support, understanding and for challenging me with new research ideas. To Simeon, thank you for your advice and problem-solving skills. Also, thank you for always being so quick correcting my work and getting back to me. To Ian Hanson, for the exciting discussions about dosimetry and treatment planning system. Thank you for making me aware of the clinical implications of my work. Also thank you for the constant support with the dosimetry experiments, treatment planning system and helping me through my struggles. To Simon Doran, for always being available to meet and helping make sense of my results with the 3D dosimeters. Thank you for your advice and for always being so enthusiastic about my results. To Antje Knopf, for your valuable feedback during the first two months of my PhD.

I also want to thank everyone at the National Physical Laboratory (NPL) in the UK, for the fantastic time I spent there and for introducing me to the world of dosimetry. To Simon Duane and Ilias Billas for allowing for the interesting discussions about dosimetry and for allowing me to perform experiments not only at NPL but also at the Netherlands Cancer Institute in the Netherlands. To David Shipley for his enormous help when I started learning how to work with EGSnrc and performing Monte Carlo Simulations. To Ileana Patallo for the lovely chats at NPL and your feedback on film dosimetry.

To Ciara McErlean for your patience showing me how to work with the

Contents

Contents

Contents

Contents

List of Figures

List of Tables

List of Abbreviations

2D   two-dimensional

3D   three-dimensional

AAPM   The American Association of Physicists in Medicine

AP   anterior-posterior

ATP   adapt to position

ATS   adapt to shape

BEV   beam's eye view

CB   cone beam

CBCT   cone beam computed tomography

CMOS   complementary metal-oxide semiconductor

CT   computed tomography

DF   dark-field

dpi   dots per inch

DVH   dose-volume histogram

ED   electron density

E2E   end-to-end

EPID   electronic portal imaging device

List of Abbreviations

ERE	electron return effect
IAEA	International Atomic Energy Agency
ICR	The Institute of Cancer Research
IGRT	image-guided radiotherapy
IMRT	intensity modulated radiotherapy
IPEM	Institute of Physics and Engineering in Medicine
linac	linear accelerator
LED	light-emitting diode
LF	light-field
LR	left-right
MLC	multileaf collimator
MU	monitor units
MRI	magnetic resonance imaging
FFF	flattening filter free
FOV	field of view
OAR	organs at risk
OD	optical density
ODR	offline dose reconstruction
OSLD	optically stimulated luminescence detector
PDD	percentage depth dose
PV	pixel value
ph-sp	phase space
PMMA	polymethylmethacrylate

List of Abbreviations

QA	quality assurance
RF	radiofrequency
RGB	red, green, blue
RMH	The Royal Marsden Hospital NHS Foundation Trust
RI	refractive index
ROI	region of interest
SBRT	stereotactic body radiotherapy
SI	superior-inferior
SSD	source to surface distance
TLD	thermoluminescent detector
TPS	treatment planning system
VMAT	volumetric modulated arc therapy

Chapter 1

Introduction

"If you can't see it, you can't hit it, and if you can't hit it, you can't cure it."

Harold Johns

Radiotherapy (RT) has been used to treat cancer for more than 100 years with its earliest reported use back in 1895 with the discovery of X-rays [50, 102]. It aims to maximize the probability of tumour control while minimizing complications to healthy surrounding tissues. The most widely employed form of RT is external-beam RT (EBRT) with a linear accelerator (linac), which is used to irradiate a patient from different directions to reach a tumour with a desired dose distribution [85, 185]. After the diagnosis, an image, usually a computed tomography (CT) scan, of the patient is acquired and used by the radiation oncologist to define the gross tumour volume. Additional margins to that volume are delineated to define the target volume, to take into account the microscopic spread of the tumour and geometric uncertainties during delivery. A treatment planning system (TPS) is then used to design a plan that attempts to deliver the required radiation dose to the target volume whilst sparing healthy tissues. The calculated dose is then delivered to the patient throughout different session days, named fractions.

Image-guided RT (IGRT), which uses imaging before or during each treatment

session to assess the target's position, has become essential for the delivery of complex RT [23, 206]. Several imaging modalities are conventionally used for position verification, including planar MV, planar kV panels or cone-beam CT and ultrasound [95, 206]. These techniques allow the correction of patient set-up errors. Unfortunately, these imaging techniques provide limited visibility of the tumour itself, particularly in regions where soft tissue contrast is essential for a better tumour definition [33]. The use of magnetic resonance imaging (MRI) for IGRT has been proposed as a way to overcome these issues [115]. Compared to X-ray based imaging, MRI offers several benefits. It produces high-quality soft-tissue contrast images, that can be acquired from different orientation planes, and does not rely on ionizing radiation [137].

Integrated MRI scanners with radiation delivery machines [66, 105, 117, 147, 166] have recently been developed. They can be used to adapt treatment plans based on the anatomy of the patient, immediately before and during treatment [69, 112, 142, 208]. The first integrated system, the ViewRay® (Cleveland, OH), started treating patients in 2014 [147]. It consists of a low-field MRI scanner together with three cobalt sources [147]. Shortly afterwards, an Elekta MR-linac was developed at the UMC Utrecht, where the first patients were treated in 2017 [117, 165]. Such a system was installed at the Royal Marsden Hospital (RMH) and the Institute of Cancer Research (ICR) in Sutton in 2016, and the first patient was treated in 2018.

The Elekta MR-linac consists of a 7MV linear accelerator which rotates in a ring around a 1.5T MRI system. In this design, there is a constant magnetic field perpendicular to the beam direction [162–164, 167]. The primary photon beam is not affected by the magnetic field, but the resultant secondary electrons are deflected by the Lorentz force which acts perpendicularly to their motion. In homogeneous tissue, the dose distribution from one beam displays a shifted and asymmetric penumbra and a reduced build-up distance [167] when compared to the same beam on a conventional linac. At tissue-air interfaces, the effects are more evident as electrons that exit the tissue will describe a circular path in air

and re-enter the tissue. This electron return effect (ERE) is responsible for a substantial dose increase (or decrease) at the interfaces between air and tissues [163]. The ERE depends on the energy of the secondary electrons, the magnetic field strength and direction, as well as on the interface shape and material. This effect can increase the complexity of radiation delivery in treatment sites near air cavities, such as the rectum, sinus and trachea, or in low-density tissues like the lungs.

A new Monte Carlo (MC) dose calculation platform has been updated and included in the treatment planning system (TPS) of the Elekta MR-linac [20, 81]. This dose engine accounts for the magnetic field effect on the path of the electrons, while still providing fast and accurate dose calculations [20, 81]. However, the correct dose calculation and its delivery by the MR-linac need to be validated. This process might not be as straightforward as for conventional linacs. The detectors typically used in RT such as ionization chambers or diodes are affected by the magnetic field, and therefore can only be used in combination with correction factors. The typically used detectors in RT such as ionization chambers or diodes are affected by the magnetic field, and therefore can only be used in combination with correction factors. These factors depend on the magnetic field strength and orientation, along with the detector type and geometry [138, 152, 153, 189]. In addition, the detector arrays of ionization chambers and diodes that are commonly used for patient-specific QA and as end-to-end (E2E) tests, to verify both treatment planning system (TPS) dose calculation and dose delivery, also have their drawbacks [188, 203]. In particular, these detectors have finite resolution providing only discrete dose information. The superior target accuracy provided by an MR-linac will contribute to the increasing use of small fields and steep dose gradients. These small fields would not be accurately validated with these arrays of detectors. Besides, these dosimeters do not resemble human geometry or allow mimicking or measuring at heterogeneous regions where the influence of the magnetic field is more substantial due to the ERE. As an alternative, E2E tests can be performed with anthropomorphic phantoms with thermoluminescence

dosimeters (TLDs) or radiochromic films [36, 91]. However, these detectors are also limited to a few measurement planes. They, therefore, would not be able to measure in 3D the dose distributions at the interfaces of the tissue/phantom and air.

Chemical 3D dosimeters were developed to overcome the aforementioned limitations of the conventionally used detectors, as they provide full 3D dose information with high spatial resolution [145, 181]. PRESAGE® 3D dosimeters (Heuris Pharma, NJ, USA) are radiochromic dosimeters which undergo optical density changes with accumulated dose. These changes can be measured with an optical-CT scanner in order to obtain a 3D absorption map of the sample [57]. The excellent results that have been obtained with PRESAGE® samples to validate complex RT treatments prompted their use in the field of MR guided RT (MRgRT) [155, 177, 197]. In contrast to other chemical 3D dosimeters, the response to dose of PRESAGE® samples is not affected by the presence of oxygen. They also need not be enclosed within a container, which makes them a good choice for measurements at the interface between the dosimeter and air [2, 108].

Their use as E2E test objects will be of particular relevance for the MR-linac since additional dose verification, such as patient-specific quality assurance (QA), cannot be performed. It is not possible to measure the treatment plan, to be delivered to a patient, on a phantom, before its delivery to the patient, as a new plan is always re-calculated or re-optimized while the patient is still on the couch. Consequently, the treatment plan adaptation workflows should be validated with high resolution (<1mm) and accurate 3D detectors (within 3%) to ensure they will perform as expected (distance to agreement and absolute dose difference within 3mm and 3% respectively [96]). In the future, the MR-linac will allow real-time treatment adaptation by tracking the position of the target. Its correct operation also needs to be investigated, preferably using 3D dosimeters as well. Furthermore, MR-linacs are a new technology with no historical record of their performance, so additional confidence-building measurements are desirable.

The use of 3D dosimeters for MRgRT applications is being investigated by

different groups [61, 122, 123, 169]. An Initial study using a cylindrical sample of PRESAGE® with a hole, under a 1.5T magnetic field, was able to identify the ERE [35, 123]. Yet, quantitative dose distributions could not be obtained due to artefacts around the sample cavity.

1.1   Aim and outline of the thesis

This PhD aims to develop methodologies using PRESAGE® 3D dosimeters for the verification of dose distributions delivered with the Elekta MR-linac. Measurements of the ERE effect are of interest to make sure the TPS of the MR-linac is correctly modelling the magnetic field. This way, the dose distribution of treatment sites with interfaces between tissues with high-density differences can be calculated with confidence. E2E tests are conducted to ensure the treatment adaptation options of the MR-linac are performing as expected. Dose verification is performed with PRESAGE® dosimeters together with phantoms to mimic both simple geometries and clinical treatments.

The outline of this thesis is as follows:

In Chapter 2, I start with a theoretical background on the basics of RT modalities and techniques. Focus is given to QA methodologies and the use of detectors in both conventional RT and with an MR-linac, and how they differ due to the presence of a constant magnetic field. The chapter concludes with an overview of chemical 3D dosimeters and their use in MRgRT systems, with particular attention to PRESAGE® dosimeters, which optical density changes with dose are read out using optical-CT scanners.

In chapter 3, I describe the methodologies and the systems that I use to scan PRESAGE® samples for all the experiments performed in the subsequent chapters.

In Chapter 4, I describe an initial sample's characterization that demonstrates the suitability of using PRESAGE® dosimeters in a magnetic field. As I aimed to use PRESAGE® samples to verify dose distributions delivered by the MR-linac,

it was essential to characterize their response to dose. In this same chapter, I demonstrate that, for the first time, cylindrical samples of PRESAGE® could accurately measure the ERE, by comparing the results with MC simulations. These experiments were performed at the National Physical Laboratory (NPL) in the UK using an electromagnet and a cobalt source. These cylindrical samples, however, showed a non-uniform response radially from their centre to their edges. Hence, dose information could only be reliably obtained at the centre of the samples and the ERE measured using their flat surface.

In chapter 5, I investigate the spatial non-uniform dose response of PRESAGE® samples, and develop a correction methodology to compensate for these effects. This correction was then applied to samples irradiated using 3D-CRT and IMRT plans in both a conventional linac and at the MR-linac, making measurements at the dosimeter's axial edges possible. The work developed in this chapter was fundamental for the successful dose verification of adapted treatment plans delivered at the MR-linac and described in the following chapters of this thesis.

In chapter 6, I use PRESAGE® samples to perform E2E tests to verify the overall accuracy of the Monaco (Elekta AB, Stockholm, Sweden), TPS of the MR-linac. In particular, to validate the plan-adaptation workflows, which are being used clinically to treat patients. Samples were used together with a phantom to be representative of clinical scenarios as, a treatment of a tumour in the lungs or in the pelvic region. PRESAGE® samples were irradiated surrounded by air or water, with and without an air cavity.

In chapter 7, I irradiate PRESAGE® samples under motion to validate tracked multileaf collimator (MLC) dose delivery at a conventional linac and the MR-linac, both used in research mode. In the future, real-time MLC-tracked RT will be implemented clinically at the MR-linac to compensate for tumour motion.

Finally, in chapter 8, the main findings of this thesis and their contribution in the field of MRgRT and 3D dosimetry are discussed, and future work in the field is explored.

Chapter 2

Background

This chapter provides background information for the subsequent chapters of this thesis. I started by presenting the basics of RT modalities and techniques, also describing the benefits and challenges of using MRI for IGRT. Special focus was given to QA methodologies and the use of detectors in both conventional RT and at an MR-linac. The chapter ends with an overview of chemical 3D dosimeters and how these systems can provide superior spatial dose information when compared to the conventionally used detectors.

2.1   Radiotherapy

Cancer consists of a collection of diseases that occur as a consequence of an abnormal growth of malignant cells, that can be confined within a body region or can travel through the lymphatic and vascular system reaching distant organs [182]. Treatment consists of radiotherapy (RT), chemotherapy, immunotherapy, hyperthermia, surgery or a combination of these, which will be employed depending on the stage and location of the cancerous cells.

RT aims to deliver a therapeutic dose of ionizing radiation to a tumour, destroying its cells by damaging their DNA, while sparing the surrounding healthy tissues. It is estimated that two-thirds of all cancer patients worldwide receive radiation therapy during the course of treatment, mainly with external-beam RT (EBRT) with photons [50]. This consists of directing high energy X-rays, generated by a linear accelerator (linac), into the patient's body [85]. Although photons are the most common form of EBRT, treatment is also possible with electrons, protons, or heavy ions. An alternative method of RT is brachytherapy, where radioactive sources are placed inside the body close to the tumour.

RT dose is not delivered all at once, instead it is performed over several days, known as fractionation. Amongst other effects, this gives the healthy tissues time to recover whilst most of tumour cells are unable to repair [132]. A RT treatment consists of a combination of steps which are described in the subsequent chapters.

2.1.1   Radiotherapy treatment pathway

After the clinical assessment and therapeutic decision to treat a cancer with RT, a pre-treatment image of the patient is acquired. Immobilization devices are frequently used for a reproducible patient set-up as well as to reduce patient's external motion. Tattoo marks are drawn on the patient's skin, or on the immobilization device, which are used to align the patient with lasers. These lasers are present in both imaging and treatment rooms (for RT with conventional linacs). This way, the patient can be set-up in the same position in both the treatment

room and imaging room (typically within 1-5mm uncertainty depending on the treatment site and if pre-treatment imaging is used or not) [161]. A CT scan is the most commonly used imaging modality. It provides 3D visualization of the tumour and its surrounding tissues as well as the attenuation coefficient for each material, which can then be converted to electron density [204]. This density information is required for dose calculation.

The acquired CT image is then transferred to a treatment planning system (TPS) where the radiation oncologist manually contours the tumour volume. This volume is usually referred to as gross tumour volume (GTV) and consists of the visible extent of the tumour mass [118]. The ability to define the target volume can be enhanced with the use of contrast or by combining a CT scan with other imaging modalities such as, MRI, positron emission tomography (PET), single-photon emission computed tomography (SPECT) or ultrasound images [206].

Non-visible microscopic spread of the tumour is accounted for by adding margins to the GTV and creating a new volume referred to as the clinical target volume (CTV). Intra and inter-fractional internal organ motion from e.g. respiration, bowel movement and filling of the bladder and rectum can be taken into consideration by the internal target volume (ITV). The dose is prescribed to the planning target volume (PTV), to compensate for geometric uncertainties during the treatment delivery (e.g. patient positioning and organ motion between fractions) [119]. Uncertainties should be mitigated to avoid unnecessary large PTV margins that will result in more dose being delivered to surrounding healthy tissue. Nearby organs to the target, which are sensitive to radiation, are referred to as organs at risk (OAR), and need to be contoured for consideration during the TPS dose optimization.

A treatment plan is then created and optimized to calculate a 3D dose distribution to be delivered to the patient (see subsection 2.1.2). It aims to deliver the prescribed dose to the PTV while minimizing the dose to the OAR.

2.1.2   Dose delivery techniques and calculation

Historically, RT was performed using rectangular fields, delivered with wedges or shaped blocks, to collimate and shape the dose delivered to the PTV. The development of the multi-leaf collimator (MLC), which consists of several high-density leaves that move independently of each other, allowed faster treatments in which the beam's eye view (BEV) of the target could be matched without the need for shaped blocks [23].

In conformal 3D planning (3D-CRT) a set of parameters such as the number of beams, their angles, shape, etc., are defined by the planner to obtain a desirable dose distribution (forward planning). Intensity-modulated RT (IMRT) emerged as a way to address the limitations of 3D-CRT and treat more complex target shapes. Typically multiple ($\geq$5) beams are used, with each beam being divided into multiple small beamlets to which a different fluence is assigned [205]. This technique was improved by the use of inverse treatment planning which allowed generating fast IMRT plans. For this approach, the planner specifies a set of dose-volume constraints, targets/objectives to the PTV and OARs. The beam parameters (MLC shapes, fluence) are then varied iteratively using an algorithm until a dose distribution is achieved which satisfies the planning criteria. An alternative to IMRT is volumetric modulated arc therapy (VMAT). Whilst IMRT uses discrete beams delivered from given angles, with VMAT the radiation is delivered continuously while the gantry rotates around the patient [156] and the MLC is moving.

Stereotactic body RT (SBRT) (also referred to as stereotactic ablative RT (SABR) when very high doses are used), can be delivered through IMRT and VMAT techniques [16]. In these treatments, high doses are delivered to the target in reduced number of fractions. For this to be possible without a substantial dose to the OAR, PTV margins are reduced and steep dose gradients are used in these regions [16]. SBRT are typically applied to treat smaller size tumours and require more restrictive tolerances of dose delivery and more rigorous patient positioning

[23]. Due to the reduced PTV margins, and increased dose delivered to the PTV, failing to deliver the dose to the target may lead to the delivery of high dose to the healthy tissues.

2.1.3   Image-guided radiotherapy (IGRT)

In image-guided RT (IGRT) an image of the relevant internal anatomy of the patient on the treatment couch is taken prior to, or during, each treatment, to assess the location of the target and OAR. The incorporation of this step in the RT treatment chain has enabled the correction of positional set-up errors, by repositioning the patient if necessary, and has given confidence in the use of reduced PTV margins [132]. Achievable systematic and random setup errors where found to be less than 2mm for head and neck and 3mm for general pelvis [89].

Electronic portal imaging devices (EPID) are a standard on modern RT linacs, and can be used to obtain 2D planar images using the treatment beam as an imaging source. Another frequently used method of pre-treatment image verification is kV cone beam CT (CBCT) in which a 3D image is acquire to match with the treatment planning CT. In this system a conventional X-ray tube is mounted on the linac gantry, perpendicular to the beam axis and opposite to an X-ray detector [73, 132].

Non-radiation based systems can also be used for pre-treatment patient position verification, such as ultrasound imaging or camera-based system that take a surface imaging of patients [47]. Alternatively, radiofrequency (RF) systems can be employed to track electromagnetic transponders in real-time (e.g. Calypso, Varian Medical Systems) implanted within the tumour [26]. For lung motion, breathing control devices can also be used to restrict and control the patient's breathing pattern [136].

The implementation of IGRT has allowed treatment plan adaptation. As opposed to irradiating the patient using the same plan throughout the RT treatment, a new plan can be created to adapt the dose to the patient anatomy at the
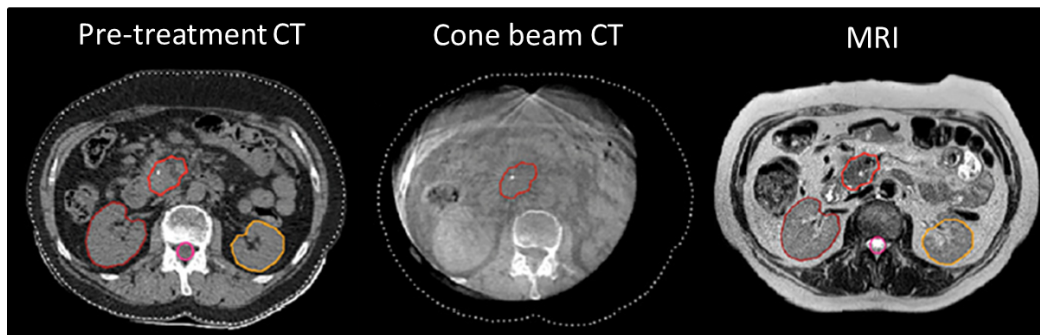
Figure 2.1: Axial view of a patient with a pancreatic tumour imaged with a conventional CT scan used for planning (pre-treatment CT). The poor soft-tissue contrast in the CT and the CBCT images required the use of implanted fiducials to locate the tumour position accurately. On the MRI, there is a direct visualization of the tumour, which avoids the need for fiducials (Figure from [30]).

time of their treatment. Options include calculating a new treatment plan offline when a patient undergoes substantial anatomy changes that can compromise PTV coverage or lead to unnecessary dose to the healthy tissues, by acquiring a new CT scan [77]. Another option of treatment plan adaptation is to use the plan of the day protocol. In this case, multiple plans are generated using the pre-treatment CT scan. The one that most closely matches the current anatomy of the patient is selected for the RT treatment on that day (e.g. different bladder fillings) [79].

These pre-treatment image techniques minimize patient set-up errors and in some cases, even allow monitoring the tumour motion in real-time. However, they provide limited visibility of the tumour itself, or they might require the use of surrogates for the identification of the target position [26, 47], particularly for tumours in the abdominal region (Figure 2.1). The use of MRI for patient position verification and RT adaptation was implemented to overcome the mentioned issues. Hence, the position of the tumour and OAR could be visualized prior and during a RT treatment. Details on MRgRT are in subsection 2.3.1.

2.2   Quality assurance in radiotherapy

When a new linac is installed, acceptance tests are executed by the supplier and customers to make sure the equipment is performing as detailed in its specifications.

Radiotherapy steps

Treatment planning imaging (CT, MRI, SPECT,..)	Image registration	Delineation of target and OAR	Treatment planning	Patient immobilization, pre-treatment image	Dose delivery
• Geometric • Imaging devices • Image resolution • CT number accuracy	• Registration • Image resolution • Distortions (if MRI)	• Target and OAR delineation Biological: associated with CTV definition • Geometric: related to CTV and PTV margins.	• Dose calculation • Dose voxel size selection • Optimization routines	• Patient set-up, • Registration with pre-treatment image • Patient anatomy changes per fraction	• Machine performance and calibration • Beam profile, energy, MLC, monitor chamber reproducibility

Figure 2.2: RT steps and examples of associated uncertainties. Adapted from [145].

This process is followed by the linac commissioning, which consists of a set of geometric, mechanical and dosimetric tests to ensure the linac is working as expected [125]. The dosimetric measurements required for the implementation of the TPS beam model, are also performed. Reference values and tolerance levels are also defined at this stage, which are then periodically verified during routine quality assurance (QA). A QA program is essential to ensure the processes and the equipment are working within the defined tolerance levels. The tests to be performed are commonly provided by national guidelines [111, 125].

In Figure 2.2, a summary of the most frequent sources of uncertainty in each step of the RT chain are described. With the advances of delivery systems and better imaging techniques, the accuracy in the dose delivered to the target has significantly improved. However, these improvements have made the task of QA more challenging. Making sure the dose reaches the intended target has become even more critical for hypofractionated treatments (where the dose per fraction is >2Gy as opposed to 1.8 to 2Gy used conventionally) to avoid unacceptable normal tissue toxicity.

2.2.1 Dosimetry

A linac uses RF waves to accelerate electrons to high kinetic energies until they collide with a high-atomic-number metal target, thus generating high energy X-rays (MV photons) via the Bremsstrahlung effect. When the photons leave the linac, they interact with the material along their path. They can undergo different types of interactions, of which the most relevant for the range of energies

used in RT are the photoelectric effect, Compton scattering and pair production [161]. When photons interact with matter, they transfer part or all their energy to secondary electrons, which in turn deposit their energy in the tissues.

The sum of the kinetic energy, released by all charged particles liberated by uncharged ionizing radiation in a material per unit of mass, is known as Kerma (kinetic energy released in matter). However, the quantity of interest in RT is the quantity of energy deposited per unit of mass of tissue due to ionizing radiation. This quantity is known as absorbed dose and is given in Gy (1Gy = 1J/Kg). The measurement of that quantity is known as dosimetry [132, 161]. Calculated dosimetric quantities are used to estimate the dose that is delivered to a patient in RT, but are also employed in other fields, such as radiology and radiation protection.

Dosimetry can be classified in terms of reference (absolute) or relative, and different types of radiation detectors can be used depending on their application (see subsection 2.2.2) [184].

In reference dosimetry, absolute dose measurements are performed using a specific, well-defined standard set-up and protocol. Reference dosimetry is performed using a detector, normally an ionization chamber that can be traceable to a standard dosimetry laboratory. The dose output of the linac is defined for specific reference conditions. For example, in the UK 1cGy/MU is usually defined for 10 x 10cm^2 field at 100cm source-to-surface distance (SSD) at the point of dose maximum (dmax) in water [9, 126, 148].

In relative dosimetry one is concerned with the normalized dose distribution regarding a reference point. Relative dose measurements are performed during the linac commissioning to establish beam characteristics, including the percentage depth dose (PDDs) (Figure 2.3a), lateral dose profiles at different depths (Figure 2.3b) and relative measurements of beam output factors for different field sizes [44, 125, 161].

a

b
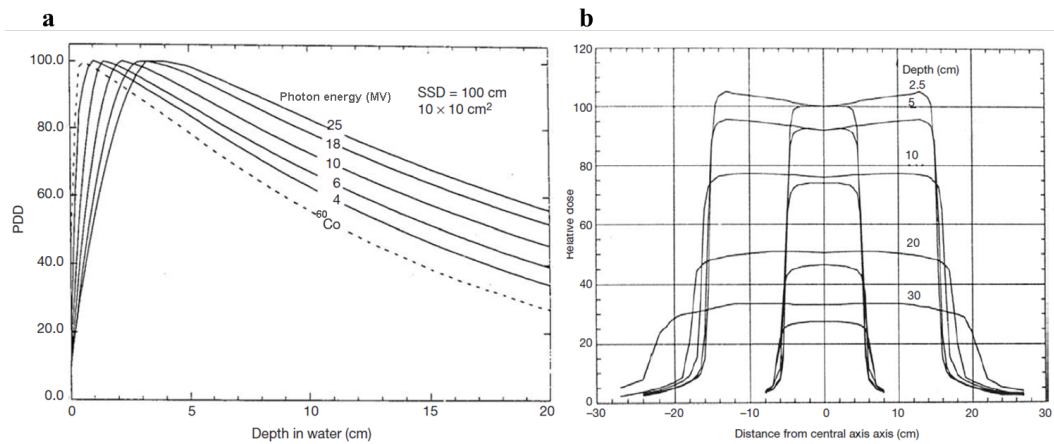
Figure 2.3: (a) PDD curves in water for a 10 x 10cm^2 field at an SSD of 100cm for various MV photon beams energies and a Cobalt-60 (^{60}Co) [161]. (b) Example of normalized lateral beam profiles for two field sizes (10 x 10cm^2 and 30 x 30cm^2) for a 10MV photon beam at various depths in water. The central axis dose values are normalized based on the PDD value of the corresponding fields [161].

2.2.2 Methods of radiation measurements

An ideal detector should provide accurate, precise and reproducible measurements and should not have directional, energy or dose-rate dependency. Moreover, it should preferably have a high spatial resolution, have a real-time response that is linear with dose, be water equivalent, re-usable and be able to measure dose in 3D [145]. These characteristics are not easily achievable, and, despite manufacturers' attempts at producing such a detector, there is currently no detector system that fulfils all these conditions. Different detectors can be used together instead to achieve most of the mentioned characteristics. The most widely used detectors for RT applications are ionization chambers and diodes for absolute and relative dose measurements, respectively. Radiochromic films are commonly used when dose measurements in 2D are desirable. Here I only describe the detectors used in this thesis.

2.2.2.1 Ionization chambers

Ionization chambers consist of a gas-filled cavity enclosed by a conductive outer wall (cathode) and a central collecting electrode (anode). Secondary electrons,

EBT3 gafchromic films
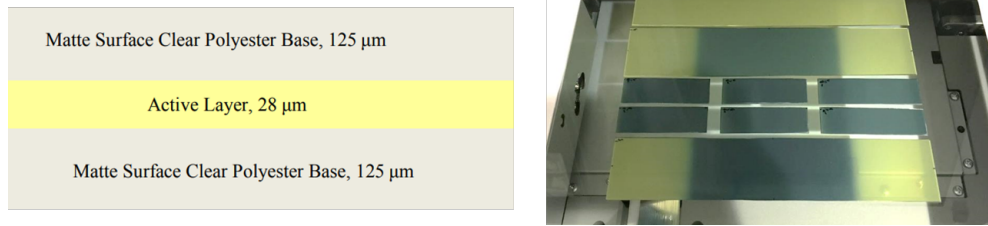
Figure 2.4: Gafchromic EBT3 films (Ashland Inc., Wayne, NJ, USA) structure and irradiated samples placed on a flatbed scanner (Epson model 10000XL).

which are generated both inside and outside the chamber, ionize the atoms and molecules of the gas, creating ion pars. The amount of ionization produced is proportional to the energy delivered to the medium and can be measured based on the charge created in the gas. When connected to an electrometer, a potential difference is generated between the anode and the cathode which leads to a collection of the ions in the chamber. The motion of the ions travelling between the electrode generates a measurable electronic signal [161, 185]. There are different types of ionization chambers which are used for distinct purposes. Free air ionization chambers are used by national standards laboratories to calibrate reference standards chambers [126], which are then used to calibrate ionization chambers used in the clinic. The most widely used chamber of this type is the Farmer chamber. They provide high-precision, reproducible and accurate absolute dose measurements within 1%. They are typically used for beam calibration (absolute dose measurements) but cannot give a good indication of the position of a dose measurement in high dose gradients as they suffer from volume averaging.

2.2.2.2   Chemical detectors

Radiation creates chemical changes in some materials, such as in radiochromic films, which are the most commonly used chemical dosimeters in RT (Figure 2.4b). 3D chemical dosimeters have been gaining popularity over the years and are described in detail in section 2.4

Films provide high spatial 2D dose information, have high sensitivity and are

nearly tissue-equivalent [55]. Radiochromic films are self-developing films that undergo a colour change when exposed to ionizing radiation, originated by the polymerization of dyes embedded in their active layer (Figure 2.4) [161]. The transmission of light through the film can be imaged with an optical scanner, and the optical density (OD) measured and related to dose by selecting different colour channels (red, green and blue (RGB)). The basics of film dosimetry consists of taking the raw pixel value (PV) from the, usually, red channel (location of the peak of maximum absorption of films) and converting it into net OD (netOD) [171]:

$$\text{net } OD = OD_{\text{irradiated}} - OD_{\text{non-irradiated}} = -\log_{10}\left(\frac{PV_{\text{irradiated}}}{PV_{\text{non-irradiated}}}\right) \qquad (2.1)$$

where the relationship between absorbed dose and netOD can be determined by irradiating several films with different dose levels. A calibration can be obtained by relating the dose values against the netOD. Alternatively, more reliable absolute dose measurements can be obtained by calculating the OD based on all three R, G and B channels. This method eliminates the non-dose related changes in the films [144], which covers changes due to film coating and scanner artefacts, noise, and some effects caused by dust particles in the scanner. The FILMQA Pro software (Ashland, NJ, USA) that was developed to analyse films for both absolute and relative dose determination, provides dose calculation based on this approach. The most commonly used films in RT are the Gafchromic EBT3 films which are shown in Figure 2.4. The netOD uncertainty of these films is typically around 1%, and their overall accuracy in dose determination is better than 4% [171].

2.2.3   End-to-end (E2E) tests and pre-treatment QA

E2E tests are generally performed after the commissioning of new equipment, the implementation of complex delivery techniques, or as part of audits [36]. They

verify the overall geometric and dosimetric accuracy of each RT step by assessing if the final dose distribution is delivered as calculated by the treatment plan. A phantom/dosimeter set-up is CT-scanned, a treatment plan is created, and then the dose is delivered to the phantom in the same way as it would be delivered to a patient [36, 91].

Errors due to TPS calculation, transferring the data to the linac and technical limitation in the delivery of the plan (e.g. incorrect collimation, gantry rotation, MLCs leaves moving too slow) can be identified by these verification measurements. If an agreement between the measured and the calculated dose distribution is poor then, specific tests focused on each step in the RT pathway will be required to identify the discrepancy.

Before the start of the first patient's RT fraction a pre-treatment QA measurement can be performed. This is a type of E2E test in which the treatment plan, that has been optimized on the patient's planning CT, is re-calculated on the CT scan of the phantom.

Nowadays, arrays of ionization chambers or diode detectors are normally used for E2E tests, particularly for pre-treatment QA. Examples of commercially available arrays of detectors are shown in Figure 2.5. 2D and 3D dose information can be obtained using these detectors by reconstructing the measured dose obtained from different gantry angles. These phantoms are provided with software that allows comparing the reconstructed dose distributions with the TPS calculated doses using the gamma criteria. This is a metric used in RT to compare measured and simulated dose distributions (see subsection 2.2.4). These detectors have high linearity and repeatability but only provide discrete dose information. This limitation has an impact on the accuracy of the dose measurements, in particular in steep dose gradient regions. Furthermore, the use of detector arrays has been shown to fail to detect systematic errors (e.g. MLC leaves positioning, gantry position) [149].

For a more realistic and accurate dose verification, anthropomorphic phantoms can be used instead along with radiation detectors such as films or TLDs. These

IC Profiler

OCTAVIUS 4D + PTW 1500

Delta4

ArcCHECK
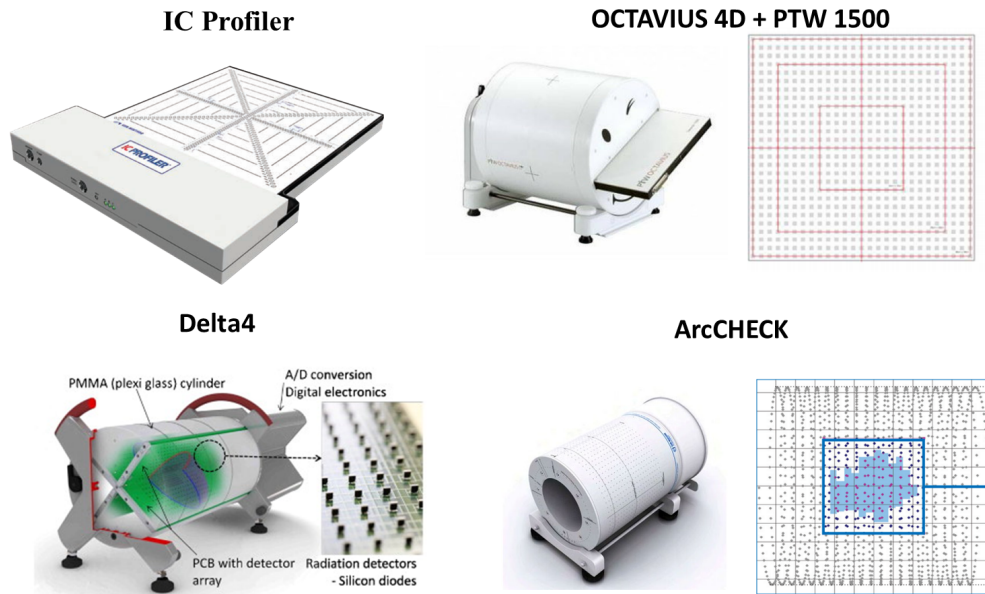
Figure 2.5: The IC Profiler (Sun Nuclear Corporation, Melbourne, FL USA) consists of 251 parallel plate ionization chambers each with sensitive volume of $(0.05\text{cm})^3$, mounted in four arrays within an area of 32 x 32cm^2 separated by 5mm [186]. The PTW 1500 IC array (PTW, Freiburg, Germany), consists of 1405 ion chambers with $(0.0026 \text{ cm})^3$ positioned in a grid as shown. It can be placed within the OCTAVIUS 4D phantom to obtain 3D dose maps [25]. The Delta4 (ScandiDos AB, Uppsala, Sweden) phantom is a cylindrical polymethylmethacrylate (PMMA) phantom containing two orthogonal detector boards with a total of 1069 p-type Si-diodes, each with 0.8 x 0.8mm^2 active measuring area [151]. The ArcCHECK (Sun Nuclear, Melbourne, FL) consists of a cylindrical water-equivalent phantom with 1386 diode array, arranged in a spiral pattern, with each detector separated by 10mm [195]. These devices rely on interpolation and extrapolation algorithms to provide a 3D dose distribution that can be directly compared to the treatment plan. Pictures of devices were taken from the manufacturer's website.

phantoms are not practical for pre-treatment QA but their use is recommended for E2E tests during linac commissioning and TPS QA [36, 90].

MV EPIDs mounted on most modern linacs, can also be used as an alternative to phantom arrays for treatment plan dose verification. They have a linear response to dose, have high spatial resolution and provide the results in real-time. Depending on the software used, EPID images can be reconstructed as 2D or 3D dose distributions, which can then be compared to the calculated dose distribution by the TPS [64]. EPIDs can also be used to perform QA tests, such as MLC leaf position verification.

2.2.4   Gamma analysis

Gamma analysis is a widely used metric that is standard procedure for patient pre-treatment dose verification. It is used to compare two dose distributions (a reference and a test) in terms of their percentage dose difference (DD) and their distance to agreement (DTA) [53, 127]. An acceptance criteria needs to be defined so that the gamma index can be calculated. Different reports have suggested distinct gamma criteria for the comparison between measured and simulated dose distribution in clinical RT. The International Atomic Energy Agency (IAEA) suggests a global gamma of 3%/2mm and 20% threshold with films when compared with the TPS [36]. The Institute of Physics and Engineering in Medicine (IPEM) report 96, considers a 3% absolute DD and 3mm DTA, for at least 95% of the measured points, as an adequate passing criteria [96]. The IAEA also supports this statement [93]. Nevertheless, the report advises that appropriate levels must be locally determined as the tolerance values are not transferable between treatment sites and clinics. Tighter gamma criteria may be applied to treatments with steep dose gradients, or to investigate possible deviations during IMRT/VMAT commissioning, which would otherwise be obscured with more relaxed criteria. In the gamma evaluation, all points with a measured dose below a given threshold (typically 10-20% of the prescription dose) are usually discarded to avoid false positives due to low signal to noise in the low dose area.

The selection of the criteria to apply does not only depend on the field size and dose gradients but it is also dependent on the resolution of the detector used. Studies have shown that for the same delivered plan, the use of different detectors produces distinct passing rates, which might be explained by different detector resolutions [191, 210].

2.3   MRI-guided RT (MRgRT)

MRI has several advantages over X-ray based imaging. When compared to a CT image, it provides high resolution and high soft-tissue contrast images

exceptionally effective to visualize most tumours. It has been shown to improve inter and intra-observer variability in tumour contouring when compared to CT, reducing systematic errors found on contours based solely on CT images [174]. In addition, MRI allows for functional imaging and does not rely on ionizing radiation. Functional MRI can identify regions of the tumour that might require an additional dose (dose painting) or be used to determine early nonresponders [13, 78].

Nevertheless, the use of MRI in RT also has its limitations. One is the absence of electron density information and therefore the attenuation coefficient of the tissues which is used for dose calculation. There are methods to overcome this issue, such as by generating synthetic CTs (pseudo-CTs) from MRI [76, 98, 199].

Another issue is that MRI is affected by geometric distortions that originate from both system hardware and the magnetic properties of the patient, which can lead to treatment uncertainties. System-related distortions can be corrected for, but the issue becomes more complex when the patient is the cause, as different patients have different magnetic properties. Regardless, most vendors provide geometric distortion correction algorithms that achieve overall geometric accuracy within 2mm [193, 207]. The use of mapping of the constant magnetic field has also been investigated to help reduce artefacts created by the linac gantry [198].

2.3.1   MRgRT systems

Integrated MRI and radiation delivery machines take advantage of MRI capabilities, allowing visualizing the tumours and OAR before and during the RT treatment [115]. MR Linac systems can also allow a treatment to be adapted both before and during a RT fraction [142, 208]. MR-guidance is of particular interest for RT where the tumour position is impacted by motion, as a tumour in the lungs [88]. RT of abdominal organs such as kidney, pancreas and liver can also benefit from the use of MRI as the treatments are still hindered by poor tumour identification with the standard X-ray based IGRT that usually require implanted fiducials, as shown in Figure 2.1 [30].

Table 2.1: Properties of the current four MRgRT systems. The MRIndian from Viewray [147], the Aurora-RT [66], the Australian MRI-linac [105], and the Elekta MR-linac which is available at the RMH/ICR [166]. Note that the Viewray system had initially 3 cobalt sources instead of a 6MV linac. Table obtained from Jelen et al., 2019[97].

System (vendor)	Magnet properties			Orientation	Radiation beam properties		
	Type	Strength	Opening		Energy	SID	Field size / leaf width
MRIdian (Viewray)	split, super-conducting	0.35 T	70 cm bore	perpendicular	6 MV	0.9 m	27.4×24.1 cm / 4.15 mm
Aurora-RT (MagnetTx)	biplanar, high temp. super-conducting	0.5 T	110 (W) × 60 (H) cm	parallel (perpendicular possible)	6 MV	1.22 m	30 cm / 5 mm
Australian MRI-linac	open, super-conducting	1.0 T	62 cm bore, 50 cm gap	parallel (perpendicular possible)	4 & 6 MV	1.9–3.3 m	30–50 cm / 9.5–16.5 mm
Unity (Elekta)	closed, super-conducting	1.5 T	70 cm bore	perpendicular	7MV	1.435 m	22×57.4 cm / 7.2 mm

SID – source-to-isocentre

The drawbacks of using integrated MRgRT systems are: the longer time required to acquire an MRI image (when compared to CBCT) that can lead to blurred images and longer overall treatment time; the reduced treatment field size when compared to conventional linacs, which limits the size of tumours that can be treated. The constant magnetic field present in the MRgRT systems has also an impact on the dose distribution that cannot be ignored. This effect will be discussed in detail in subsection 2.3.3.

There are currently five separate designs integrating an MRI scanner and an RT treatment device [66, 105, 117, 147, 166]. These designs differ in the method of radiation delivery (linac or cobalt unit), the orientation of the main magnetic field (B) (parallel or perpendicular to the radiation beam) and the magnetic field strength (0.35T to 1.5T). The different characteristics of each systems are shown in Table 2.1.

The first commercially available MRgRT system was developed by ViewRay Inc. (Cleveland, OH, USA), and started treating patients in 2014 [147]. It consisted of three cobalt sources mounted on a ring, and a 0.35T MRI. The cobalt sources were recently replaced by a 6MV linac. The Elekta MR-linac is the first commercial high field (1.5T) MR-linac system. The first patients were treated in 2017 [165]. A prototype was used as a proof of concept for this integration using a 6MV beam

[166]. The higher field strength of the MR-linac system creates images with better signal to noise ratio (SNR) that will likely improve tumour localization [116].

2.3.2   The Elekta MR-linac

In 2016, an Elekta MR-linac was installed at the RMH/ICR in Sutton, and the first patient was treated in 2018 for prostate cancer. It consists of a flattening filter-free (FFF) 7MV linear accelerator, which rotates in a ring around the outside bore of the magnet (Figure 2.6). The MRI scanner is a 1.5 T Philips Achieva with a close bore that has been modified to remove gradient and main B field coils within its central region in order to allow the radiation beam to pass through. This region is 15cm long, allowing a maximum field size of 22cm at the isocentre in the superior-inferior (SI) direction and a maximum of 57cm in the left-right (LR) directions. The isocente is at a fixed position and the couch cannot be moved in the LR or in the anterior-posterior (AP) direction inside the bore of the MR-linac. The beam is collimated by a MLC which travels only in the SI direction, and consists of with 160 leaves of 7.1mm width at the isocentre. The magnetic field strength is approximately zero at the location of the electron gun of the accelerator is achieved through shielding, to avoid interactions between the MRI and the accelerator [117, 166]. The couch moves only in the SI direction and a laser is available to align the patient in the LR direction. The typical lasers used to align the patient in the SI and AP directions on a conventional linac room are not available or needed for this integrated system as each treatment plan is adapted based on the patient position on the couch. Detailed explanation on the Elekta MR-linac treatment adaptation workflows is in chapter 6.

2.3.3   The effect of magnetic field on dose distributions

The combination of an MR with a RT device imposes not only engineering [166] but also dosimetric challenges. A magnetic field perpendicular to the beam direction affects the secondary electrons generated as a result of photons interactions [163,
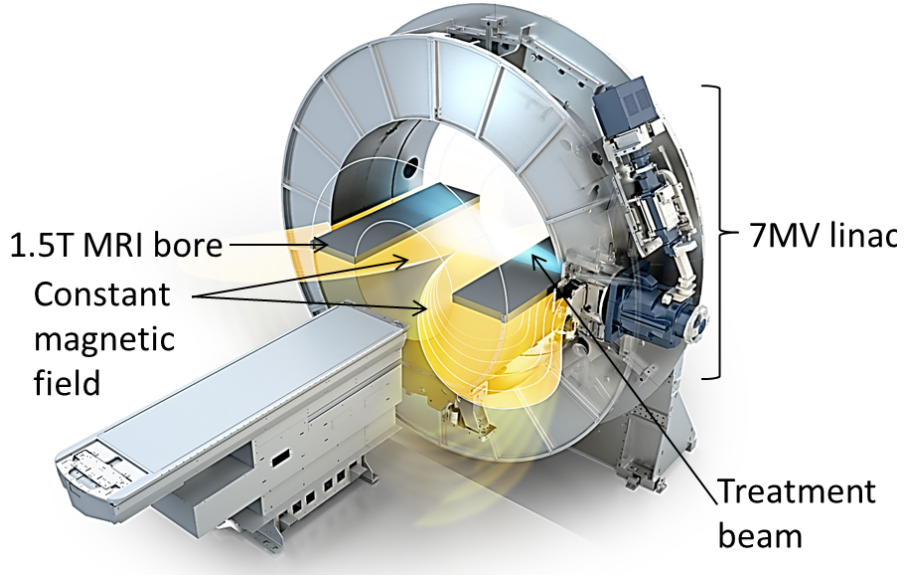
Figure 2.6: Schematic representation of the Elekta MR-linac. The different components of the linac, as well as both the treatment beam and the magnetic field, are shown.

164, 167]. This is due to the Lorentz force , caused by the constant magnetic field perpendicular to the beam direction, as per the equations:

$$\vec{F} = q(\vec{E} + \vec{v} \times \vec{B}) \tag{2.2}$$

$$R = \frac{mv}{qB} \tag{2.3}$$

where q refers to the charge of a particle, moving with velocity $\vec{v}$, through an electric field $\vec{E}$, and a magnetic field $\vec{B}$. When the velocity of the charged particle is perpendicular to $\vec{B}$, the particle follows a circular trajectory with a radius R given by Equation 2.3.

The main magnetic field of the Elekta MRL is perpendicular to the beam direction. Consequently, the cascade of secondary electrons will be deflected by the Lorentz force, which changes the deposited dose distribution [167]. For a 6MV beam irradiating an homogeneous medium, this effect leads to a reduced build-up distance by 5mm, a shifted and asymmetric penumbra in the direction orthogonal to the beam direction of 1mm and, a shift of the whole radiation field by approximately 0.7mm in the same direction (Figure 2.7b) [167].
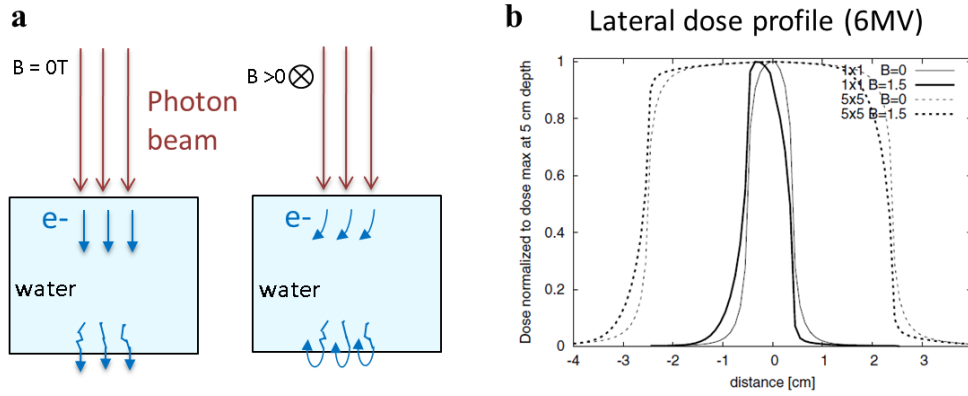
Figure 2.7: (a) Representation of the secondary electron path in water and in air with and without a magnetic field. (b) Asymmetric penumbra visible for the lateral dose profile measured at a depth of 5cm (in a water phantom) irradiated by a 6MV photon beam with a 1 x 1cm^2 and 5 x 5cm^2 fields, in presence of a 1.5T magnetic field perpendicular to the beam direction. The same profiles obtained at a 0T magnetic field are shown. Figure obtained from [167].

This effect was a matter of concern for treatment sites with high density differences, such as at the interfaces of tissue and air. The average distance travelled by an electron in air is much longer than in tissue, and as a result, electrons that would normally deposit their energy outside the tissue of interest can complete their curved path and return into the tissue (Figure 2.7a). This effect is known as electron return effect (ERE) and it is responsible for a dose increase (hot spots) at the proximal side of air cavities and a dose decrease (cold spots) at their distal side [163]. The effect on the dose distribution will be different depending on the beam energy, the magnetic field strength and direction, but also depending on the interface shape and material [163, 164]. The ERE has been studied using Monte Carlo (MC) simulations with simple geometries, for a better understanding of the implications in RT with the Elekta MR-linac [163, 164]. These studies also supplied relevant information for the other integrated MRgRT systems.

2.3.4   The effect of air cavities in MRgRT

Raaijmakers et al.,2015 [163] characterized the effects of air gaps on dose distributions and reported a dose increase of up to 40% due to the ERE (Figure 2.8a) in the presence of a 1.5T magnetic field perpendicular to the beam direction (irradiation of two 4cm long blocks of water separated by a 2cm air cavity). This dose increase could be reduced with the use of opposing beams [163] (Figure 2.8b). The ERE on dose distribution was also investigated for clinically relevant scenarios. Increased skin dose was observed for breast IMRT in the presence of a magnetic field [80]. Menten et al., 2016 [141] studied the effect of magnetic field in lung SBRT. They showed that clinically accepted lung SBRT treatments could be obtained by taking into account the magnetic field as part of the treatment optimization process. Clinically acceptable IMRT dose distributions were also achieved for cancer sites adjacent to air cavities (laryngeal and oropharyngeal tumours), providing that the magnetic field was also taken into consideration during dose optimization [162]. Other tumour sites, such as the pancreas, head and neck were also investigated, using patient CT scans with actual air cavities. This study draws attention to the fact that large dose differences can occur (15% in the pancreas case in the duodenum) if the magnetic field is not taken into consideration [31]. In all these studies, the magnetic field produced an increase in the patients' skin dose.

However, air cavities which are visible in the planning CT might not be present on the day of treatment, and if accounted for during planning they can lead to higher doses on the tissue where these cavities were. This situation occurs on RT treatments at conventional linacs, but the effects are expected to be more pronounced on the MR-linac due to the ERE. These changes to the dose distributions are difficult to predict because they depend on the shape and location of the air cavities. Treatment sites in the pelvic region might create challenges for RT in the presence of a magnetic field due to the possible existence of gas in the different segments of the bowel. A study by Bol et al., 2015 [19] suggests that care must be taken when unplanned intra-fractional (dis)appearing air cavities
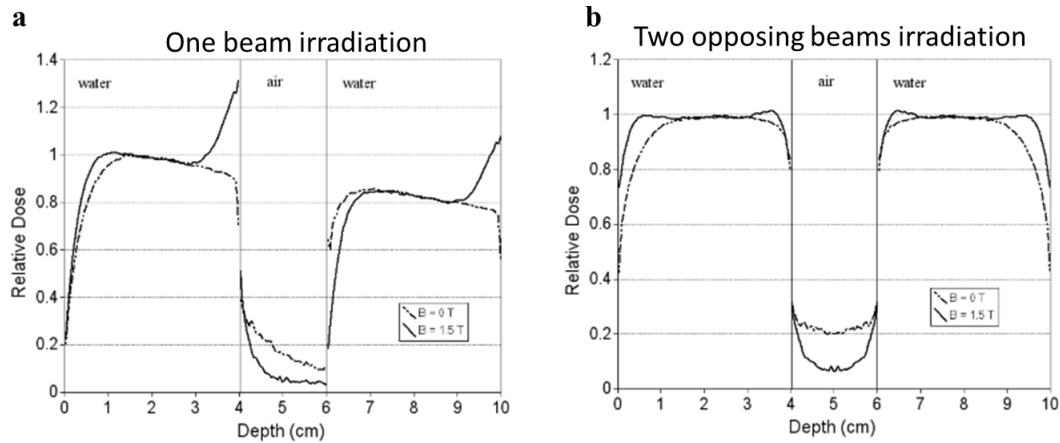
Figure 2.8: (a) PDD profiles on the central axis of a phantom with an air gap, with and without the presence of a 1.5T magnetic field. (b) PDD profile on the central axis when using two opposing beams on the same phantom, again with and without the presence of a 1.5T magnetic field showing the reduction of dose at the interfaces of the phantom. Figures taken from Raaijmakers et al., 2006 [163].

exist, showing absolute difference higher than $\pm 2\%$. The study only simulates instantaneous transition from tissue to air, but gradual transition as the ones occurring in the tissues, have been shown to reduce the size and magnitude of the ERE at air cavities [200]. This study, which investigated the effect of air cavities in the rectum within a fraction by artificially creating air cavities in selected patients CT scans for rectal cancer RT, showed that 2cm and 5cm diameter cavities resulted in an increase in dose of up to 2.8% and 5.3% respectively.

To account for the presence of the magnetic field a GPU-based Monte Carlo dose (GPUMCD) calculation engine was developed [81, 82]. This algorithm is available as part of the Monaco TPS (Elekta CMS, Maryland Heights, MO), used with the Elekta MR-linac. The Viewray system has also developed a fast and accurate MC based dose calculation engine to simulate the effect of magnetic fields [52, 147]. The accurate modelling of the magnetic field and the ERE by these TPS require validation.

2.3.5   QA for the MR-linac

Before dosimeters such as ionization chamber, diodes, films, (among others) could be used for QA purposes on an MRgRT system, it was essential to understand if and how their response could be affected by the magnetic field.

Given that commonly used ionization chambers in RT are air-filled cavities, the secondary electrons average path length and their trajectories in the chamber change with the B field strength and orientation, thereby affecting the chamber response [138, 189]. In addition, air gaps between the ionization chamber and the phantom material lead to a non-negligible change in the detectors response to dose so dose measurements should be done in water tanks [152]. Other detectors as diodes and diamond are also affected by the magnetic field [172, 192].

The detector arrays that are traditionally used for both E2E and pre-treatment QA were not initially suitable to be placed inside an MR-linac because of their electronic and ferromagnetic components. Updated versions of these arrays of detectors, covered in section subsection 2.2.3 and shown in Figure 2.5, have been developed to be MRI compatible. Their performance has been evaluated to assess whether their response has changed with the effect of the Lorentz force. Normalized profiles were found to be comparable to the ones obtained with radiochromic films using both the IC profiler [188] and the STARCHECK MAXI MR [160](figure not shown). However, it was recommended that care must be taken when performing absolute dose measurements. MR compatible versions of both the ArcCHECK and Delta4 did not show significant differences in performance when used at the MR-linac [86, 203]. For MRgRT, these systems still have their place as part of the linac commissioning and TPS QA. However, for the Elekta MR-linac, these systems do not have much utility as pre-treatment QA. As the treatment plan is adapted at each treatment fraction, the correct delivery of a dose distribution can only be verified at the end of a RT session and not before the patients' treatment [86, 124]. Some studies have investigated the performance of radiochromic films at different beam energies, in different magnetic field strength and orientation

in relation to the B field [14, 18, 173, 178]. Magnetic fields have been shown to affect the polymerization process in radiochromic films. Initial publications on this matter presented contradicting data. Some discrepancies could be partly explained by the different beam energies used and types of films (EBT2 and EBT3). To clarify the inconsistencies in the literature, a study by Billas et al., 2019 [18] was recently published in which films were irradiated in different orientations and magnetic field strengths. The authors found a small effect on the sensitivity of the films which, if not corrected for, can lead to errors on the measurement of absorbed dose that could vary from -0.6% at 0.5T up to 2.4% at 2T. A 1.5% error was found for a 1.5T magnetic field, which is within the film uncertainty. The magnitude of the changes agree with other studies [14, 178].

2.4   3D gel/plastic dosimeters

3D dosimeters can play an important role in RT as they have been useful in commissioning and QA of treatment machines and TPS, and also as a method of pre-treatment specific QA [180]. The ability to measure 3D doses is desirable for dose verification of complex treatment plans. This verification might be even more relevant for the MRgRT system, as dose perturbations due to the ERE can occur for targets near air interfaces. Films can provide relevant dose information, but they are unable to identify dose differences that occur out of the plane of their measurements.

2.4.1   Fricke gels

Fricke (ferrous sulphate) gels consist of acidic oxygenated aqueous solution of ferrous ion (Fe2+) that, when irradiated, and after several reactions, are converted to ferric ions (Fe3+) [71]. The different ions have different spin-lattice parameters of relaxation time (T1) of the protons in water molecules, which can then be measured using an MRI. A dose distribution can be obtained by relating the absorbed dose to the spin-lattice relaxation rate R1 (= 1/T1) [10]. Optical CT
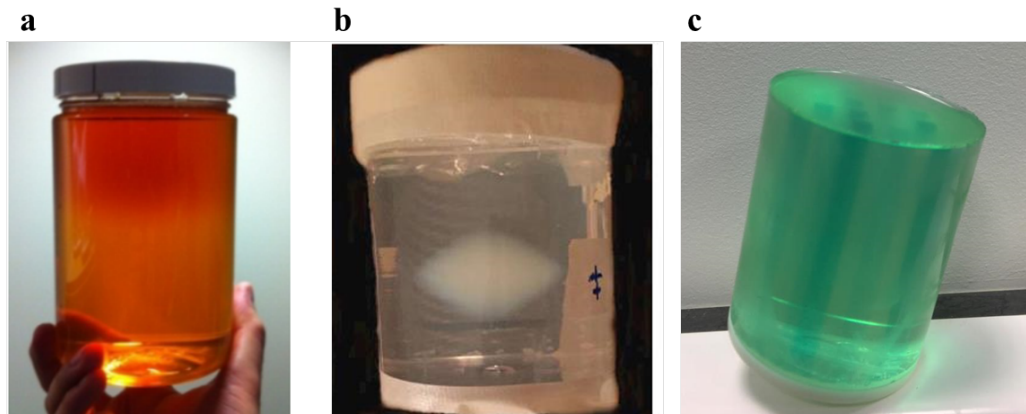
Figure 2.9: (a) Colour change of a Fricke-xylenol-orange-gelatin dosimeter irradiated with a12 MeV electron beams [181]. (b) Polyacrylamide polymer gel dosimeter showing an increased scatter in the high dose areas radiated using a ^{60}Co beam. (c)PRESAGE® dosimeter showing darker colour on the irradiated regions of the sample.

(optical-CT) scanners were proposed, initially to be used together with polymer gels [72], as a faster and cost-effective alternative to the use of MRI scanners. Shortly after, Fricke gels were modified so that they could also be readout with these optical-CT systems [107] (see Figure 2.9a). Fricke gels can provide excellent results, but their utility has been hindered by diffusion problems that influences their spatial accuracy stability and gives the dosimeters a limited time of only a few hours to be readout after being irradiated [72, 179].

2.4.2   Polymer gels

Polymer gels consist of monomers, which are converted to polymers following a radiation-induced free radical polymerization [157]. Most of the polymer gel dosimeters require around 24h for this reaction to stabilize. Polymer gels that can be readout within 12h or less, have been only recently developed [32, 158]. The polymerized regions of the gels display a turbid white colour as a result of the light-scattering from the polymer microparticles generated by the radiation (Figure 2.9b). These particles can be imaged with an optical-CT, as the visible scattered light is attenuated proportionally to the polymer density. An MRI can also be used as the hydrogen atoms of monomers and polymers have different

relaxation times [67]. Although polymer gels are a reliable candidate for 3D dosimetry and are commercially available from both MGS Research Inc. (Guilford-Madison, CT, USA) and RTSafe (Athens, Greece), they have some drawbacks. Oxygen acts as a radical initiator, so these gels must be manufactured in a deoxygenated environment and then poured into a container impermeable to oxygen (glass or Barex®) [145].

2.4.3   Radiochromic 3D dosimeters

Radiochromic dosimeters were introduced in 2004 with the creation of PRESAGE® by John Adamovics [2–4]. PRESAGE® is commercialized by Heuris Pharma (Skillman, NJ, USA), and consists of a polyurethane matrix, a leuco dye (leucomalachite green) and a radical initiator. When the samples are irradiated a halocarbon radiolysis occurs, producing free radicals that oxidize the leucomalachite green into malachite green, which creates a colour change with the light peak absorption maximum at a wavelength of around 633nm (Figure 2.9c) [75]. The change in OD can be measured using an optical-CT, but the dosimeter itself is practically invisible on an MRI [74]. Radiochromic 3D dosimeters were created as a way to overcome some of the mentioned problems of Fricke and polymer gels. They can be fabricated in any desired shape without the need of an external container [2, 12], the measured signal does not suffer from diffusion problems over time like Fricke gels and they are also less prone to optical artefacts when readout with an optical-CT. Contrary to polymer gels that are a scattering media, PRESAGE® absorptive radiation-induced contrast is linearly relatable to the absorbed dose. This is an advantage when optical-CT is used as light scattering is known to affect the contrast and resolution of the images and increase the noise [74, 155]. In addition to the polyurethane-based dosimeters, radiochromic micelle gel dosimeters have been developed [99, 201] which have evolved to deformable versions [48].

The use of PRESAGE® 3D dosimeters in RT applications has undergone a swift development, with several publications showing reliable dose measurements

when compared to simulated data. PRESAGE® had been used to verify IMRT [155, 176, 177], VMAT [196], respiratory-gated treatments [24] and was of particular use in brachytherapy for high resolution measurements of steep dose gradients [5, 202].

2.4.4   Use of 3D dosimeters in MRgRT

There are no ideal dosimeters to QA MRgRT systems, but 3D dosimeters are the only ones that in theory allow obtaining 3D dose information with a high spatial resolution (in the order of a few microns) while enabling measurements at the interfaces between materials with two different densities. These characteristics of 3D dosimeters make them ideal to measure dose distributions affected by the ERE. However, the response of these dosimeters in the presence of a magnetic field needs to be assessed before they can be used for that aim.

Considering that PRESAGE® samples get darker as a consequence of the oxidation of leuco dyes, resulting from the free radicals produced by the radiolysis of hydrocarbons, their response may be affected by a constant magnetic field. In 2014, a study reported an underdosage of 9% and 10%-12% in the absolute dose-response of PRESAGE® (radiochromic plastic) at a 1.5T magnetic field [35, 131]. However, a later manuscript showed that a 1.5T magnetic field has a minimal effect on the absolute dose of PRESAGE® [121]. The same results were found for other radiochromic and polymer gels, which were tested in the same study.

The first study which attempted using a 3D sample of PRESAGE® to measure the ERE in 3D, used a cylindrical sample with an air cavity and irradiated the dosimeter with one beam at a 1.5T magnetic field. The results were promising but quantitative measurements of the ERE were prevented by streaking artefacts around the cavity [35, 92, 123]. Further studies used samples of PRESAGE® (∼9.5cm diameter) as part of the commissioning process of the ViewRay® system, showing very good agreement with simulated data (≥98% points passing a 3% and 3mm global 3D gamma with a 10% threshold)[169]. The study used only

homogeneous samples and did not investigate dose distributions near the edges of the dosimeters.

3D gels readout using MRI, have been investigated for dose measurements in MRgRT system. Both Fricke-type and polymer gels (MGS Research, CT, USA) have shown potentialities to be used for real-time dose accumulation using an MR-linac [90, 122]. Recently, polymer gels from RTSafe (Athens, Greece) have been used to obtain quantitative and qualitative measurements, immediately after irradiating a gel with an MR-linac [158]. Fricke-type gels were also developed with an air cavity to be irradiated and imaged by an MR-linac [123]. E2E tests performed with these dosimeters showed high passing rates for quite large gamma criteria of 7%, 4mm [120]. Preliminary results were also obtained with heterogeneous versions of these gels, with both water and lung equivalent densities [133]. Furthermore, polymer gels have been used successfully for measurements required during commissioning of MRgRT system, specifically to verify MRI-based distortion and to access the alignment between the imaging and the radiation isocentre [61, 62]. Although these dosimeters have the advantage of using the same system, an MR-linac, for both irradiation and dose readout, when compared to an optical-CT these MR readout images have both lower resolution and signal-to-noise ratio (SNR).

2.4.5   Optical-CT scanner for 3D dosimetry

A variety of optical-CT scanners have been developed to readout the dose distribution captured by 3D dosimeters. These systems work in a similar way to X-ray CT scans in that they have a source of radiation, in this case in the form of visible light, which is directed across the dosimeter, so that the attenuation through it can be measured.

The first generation of optical-CT scanners was developed by Gore et al., 1996 [72] and allow measuring doses in the range 0 to 10Gy with accuracy better than 5% and a spatial resolution of about 2mm. It consisted of a laser beam which scans the sample in step and shoot mode in the transverse direction and from different
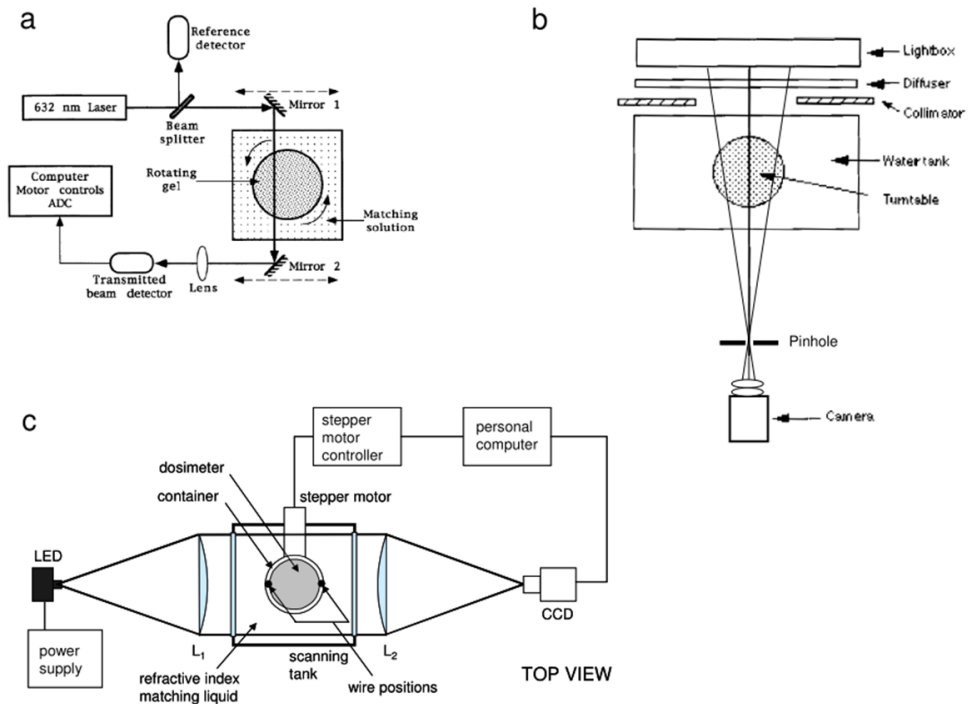
Figure 2.10: Diagrams of different types of optical-CT scanners reproduced from [58]. a) first generation of optical-CT scanners [72]. b) Cone beam CCD scanner [209] and c) parallel beam CCD scanner [114].

angles around the sample (Figure 2.10a), to obtain a 2D attenuation map of a cross-section of the sample. The sample is then moved up or down to obtain a 3D attenuation map. Given that this optical-CT scanner was very slow, over the years, several groups have developed different scanner designs which aimed to speed up the image acquisition process while maintaining or improving the image quality. In 1999 a cone-beam (CB) optical-CT scanner was developed which consists of a 2D array detector, in this case, a charge-coupled device camera, that allows a 2D projection image to be obtained at successive angular increments of the sample rotation [209] (Figure 2.10b). Complementary metal-oxide semiconductor (CMOS) detectors can also be used for this configuration. A 3D attenuation map is obtained by reconstructing the images with filtered back-projection, or with more advanced algorithms [206]. These systems reduce the scanning time from a few hours to a few minutes. In order to reduce secondary light scatter originated on the samples imaged with these scanners, parallel beam scanners were developed

which make use of telecentric lenses (Figure 2.10c) [114].

The way optical-CT scanners work can be understood with the use of the Beer-Lambert Law, which states that there is an exponential relationship between the intensity of the light transmitted through a substance and its attenuation coefficients (μ) and position (x) as given by the equation:

$$I(x) = I_0 e^{-\int_{\text{light path}} \mu(x)dx} \qquad (2.4)$$

where the transmitted light intensity is given by I and the incident light intensity by I_0. Multiple, typically tens to hundreds of projections, need to be acquired around the sample to obtain an OD ($= \log_{10}(I_0/I)$) 3D attenuation map of the original object. Commonly, the projections' images are reconstructed using filtered backprojection. A detailed description of how filtered backprojection is calculated and used in 3D dosimetry with an optical-CT can be found in a report by Doran et al., 2007 [58] and the formal mathematics in texts such as the Physics of Medical Imaging [206].

2.4.6   3D dosimeters' edge effect considerations

The difficulty of measuring near the samples' interfaces is a known issue of 3D dosimeters. Gel dosimeters are enclosed in a container, which prevents measuring dose directly at dosimeter interfaces. Nevertheless, some publications explore the use of low density gels that could offer an alternative to measurements at the interfaces of the dosimeters [46, 133]. PRESAGE® samples do not need a container, but suffer from edge artefacts caused by the optical-CT readout system used due to a refractive index mismatch (RI) mismatch between the matching liquid and the sample [56]. Several groups using 10 to 11cm diameter PRESAGE® samples reported edge artefacts [24, 155, 169, 170, 177], a few mentioning that at least 5mm around the samples edge were not considered due to these artefacts [94, 139, 169, 170]. Additional effects were found to be due to a real non-uniformity of samples of PRESAGE® to dose [49, 139] and will be discussed in more detail in

chapter 5.

Chapter 3

Optical-CT scanners - Methods, materials and samples acquisition optimisation

This chapter describes the methodology applied to scan samples of PRESAGE®. Two different in-house optical-CT scanners were used: a previously developed microscopy optical-CT and a telecentric optical-CT, which I assembled. I describe the components of both systems and their configurations and explain the choice of the hardware components selected for the newly assembled system.

3.1   Introduction and Aim

I used two different optical-CT scanners to image 3D cylindrical samples of PRESAGE®. A microscopy optical-CT scanner, which had been previously developed [60], was used for the initial experiments performed in this thesis (chapter 4). As this system allows imaging only of samples smaller than 2.5cm, due to its reduced field of view (FOV), a new optical-CT system was required. A telecentric optical-CT was assembled for this purpose. This system was used to obtain 3D dose information for the experiments described in chapters 5 to 7 of this thesis. The aim of this chapter is to give an overview of the hardware differences between the two optical-CT systems and explain the methodology required to obtained 3D OD images of cylindrical samples of PRESAGE®, which is fundamentally the same for both systems. The new system was optimized using samples of PRESAGE® as test objects.

3.2   Microscopy optical-CT scanner hardware

The optical-CT microscopy scanner is an updated version of the system described by Doran et al., 2013 [60]. McErlean et al., 2016 [135] improved the system by using a better camera (a complementary metal-oxide semiconductor (CMOS) instead of a charge-coupled device (CCD)), computer and positioning system, and characterized it for microbeam RT applications. This system, which is shown in Figure 3.1, consists of a microscope zoom lens (53-043, Edmund Optics, NJ, USA) attached to a camera (Zyla sCMOS, Andor Technology PLC, Belfast, UK) and a flat panel light-emitting diode (LED) illuminator, (PHLOX-LEDR-BL-100100-S-Q-IR-24 V, PHLOX, Aix-en-Provence, France). This illuminator emits light at 630nm wavelength and it is connected to a power supply (RS Pro IPS-603). The sample to be scanned is positioned between the illuminator and the lens, and attached to a holder connected to a rotation stage (PRS-110 ZSS43, PI miCos GmbH, Eschbach, Germany), which is then placed inside a
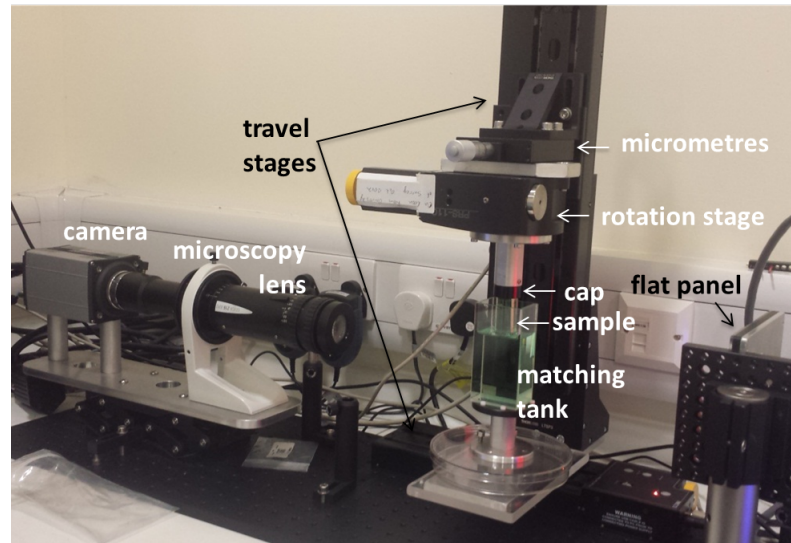
Figure 3.1: Microscopy optical-CT scanner. The sample is lowered down into the tank so that the sample central axis of rotation coincides with the centre of the projection images. Small sample position adjustments in the left-right direction (projections) are done with the micrometre.

glass matching tank (Part 704-002-40-10, Hellma GmbH, Mullheim, Germany). The rotation stage was attached to a long travel stage (LTS-300/M, Thorlabs Ltd., Ely, UK), which was used to move a sample vertically. That stage was mounted over another long travel stage (LTS-150/M, Thorlabs LTD., Ely, UK) to allow changing the position of the sample along the optical axis, between the lens and the lightsource. Sample acquisition was controlled by an in-house developed LabView® (National Instruments Corporation Ltd., Berkshire, UK) code and the images were reconstructed using software previously developed in IDL (see section 3.5 for more details). For the measurements performed in this thesis, the camera magnification was always set to 1 which allow acquiring images with a resolution of 6.5μm. Images obtained by scanning PRESAGE® samples with this system are shown in Chapter 4. The achievable image quality considering both sample and, set-up generated artefacts, are discussed in the same chapter. The acquisition parameters had been previously optimized by a student that assembled this optical-CT [134] to readout PRESAGE® samples irradiated with microbeams. The parameter used are described in section 3.6.
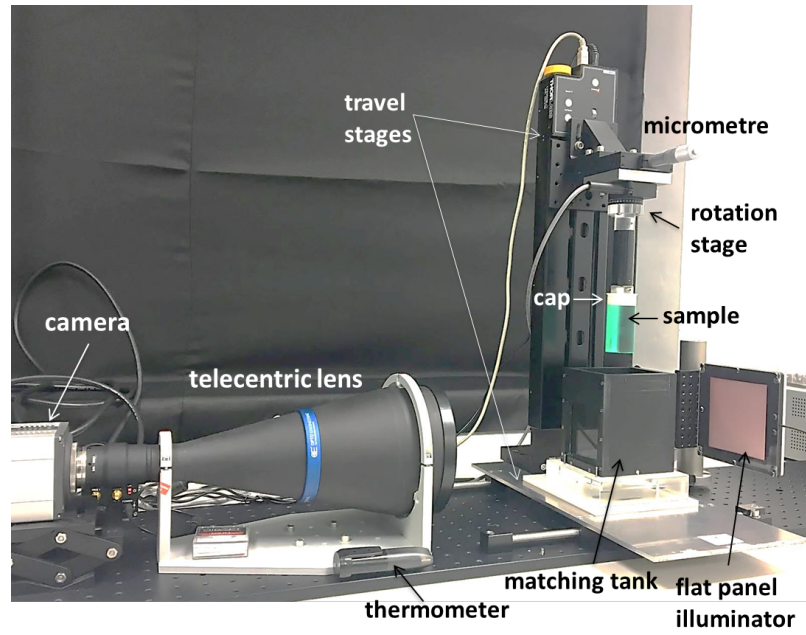
Figure 3.2: Telecentric optical-CT scanner.

3.3   Telecentric optical-CT system hardware

The final version of the telecentric optical-CT system assembled during this PhD is shown in Figure 3.2. The system consists of a new telecentric lens (TC2MHR096-C, 0.137x magnification, Opto-Engineering, Italy), a new rotation stage (CR1/M-Z7K with a controller, Thorlabs Ltd., Ely, UK), and a horizontal travel stage that was assembled in house. The same LED flat panel illuminator used in the previous optical-CT scanner was used in this system, and a new matching tank was built in-house to accommodate larger samples of PRESAGE®. A similar system was first described by Sakhalkar et al., 2008 [175] and later used to commission radiosurgery fields [37] and validate gated RT [24]. A detailed explanation of the choice of the new components and the reasons for maintaining the others are given in subsubsection 3.3.1.1.

3.3.1   Considerations governing choice of hardware

3.3.1.1   Lenses

Telecentric lenses have several advantages compared to conventional lenses when setting up a new system for 3D dosimetry application. With a non-telecentric lens, the size of the object to be imaged changes with its distance from the lens. Moreover, for the same distance, the shape of the object can change when further from the centre of the FOV of the image. Thus, these lenses require significant work to characterize the system optics for different sample sizes and distances from the lens (Figure 3.3). Regardless, the images might be subjected to distortion when using large samples.

Unlike conventional lenses, telecentric lenses only accept incoming rays that are parallel to the optical axis (a typical acceptance angle is $\sim$0.1°). This means images have no perspective, and the object size remains unchanged independently of its position (Figure 3.3). These characteristics eliminate perspective errors and facilitate sample positioning as the effective depth of focus and field (distance between the closest and farthest objects) can be significantly extended. This means the same setting and the position of the sample in relation to the lens can be kept the same independently of samples' dimensions. Compared to conventional lenses, the use of a telecentric lens as part of an optical-CT scanner provides a more flexible, easier to set-up system, which acquires projection images with high spatial accuracy, resolution and with low distortion.

There are a few parameters that were taken into consideration before the acquisition of a new lens. The choice of the lens had to be made not only based on the size and thickness of the sample to be imaged (at least 6.5cm diameter PRESAGE®) but also based on the sensor size, and the type of mount of the camera to which it would be attached to (see Equation 3.1).

$$FOV(mm) = \frac{\text{camera sensor size } (mm)}{\text{lens mag}} \tag{3.1}$$
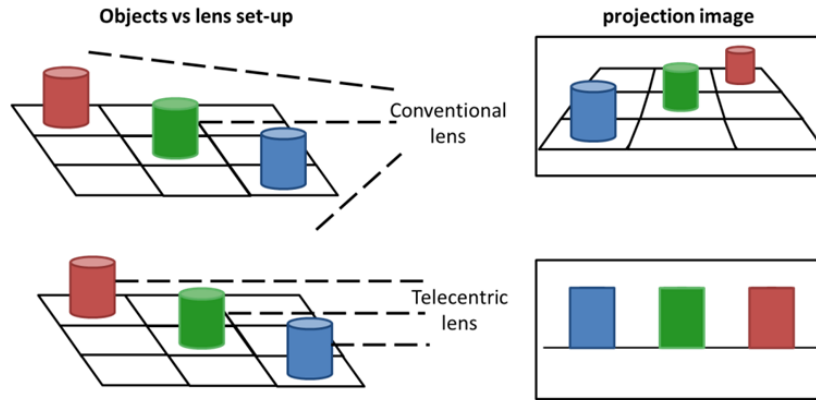
Figure 3.3: Simplified representation of the difference between the resulting projection images obtained with a conventional and a telecentric lens. Conventional lenses give different magnifications depending on the position of the object, while telecentric lenses only have one, provided that the object to be imaged is within a specific range (depth of field (DoF), which is the maximum range where the object appears to be in acceptable focus).

The selection of the lens to be bought was based on the available camera at the ICR and the fact that ideally the samples should be imaged with a larger enough FOV of around 100 x 100mm^2. The telecentric lens, TC2MHR096-C (Opto-Engineering, Italy), which has a 0.1576x magnification (mag) was acquired. The combination of this lens with the camera provides a FOV of 121 x 102mm^2 following Equation 3.1. This lens model allows larger sample sizes to be imaged in the future, without compromising the resolution of the images (smallest pixel size is $(47.9\mu\text{m})^2$). To determine the projection image pixel size, the following equation was applied:

$$\text{Image pixel size (mm)} = \frac{\text{camera pixel size (mm)} \times \text{binning}}{\text{lens mag} \times \text{object mag} \times \text{mount}} \qquad (3.2)$$

Both the object magnification (mag) and C-mount, which is the type of mount of our camera, are equal to 1.

3.3.1.2   Illuminator

The use of a telecentric lens should in theory, be combined with a telecentric illuminator to improve image quality. When using a flat panel lightsource, the rays are diffused and can reach an object with an angle, being reflected at the edges of an object. When using a collimated light (telecentric), the rays are parallel to the optical axis and consequently less reflected from the object. This leads to images with higher edge contrast and accuracy. These systems have been used successfully to image larger samples of PRESAGE® (>10cm) to obtain reliable 3D dose information for clinical RT dose ranges. An example of a system with both telecentric lens and illuminator is the DLOS scanner [197].

I tested two different illuminators, a flat panel used in the previous system and a telecentric lightsource. After imaging a sample of PRESAGE® with both illuminators, the flat panel light proved to be the most adequate for our application of measuring OD changes near the samples' edges. The combination of a telecentric lens and a illuminator creates projection images with an excessive level of detail (thick dark edges and surface marks on the samples as shown in Figure 3.4). Therefore, changes in OD due to accumulated dose could not be accurately measured. I also investigated the use of a light diffusor together with the telecentric lightsource, as performed by other groups [197]. However, it was still not possible to desensitize the "telecentricity" of the system, to the point that one could obtain information at the borders.

3.3.1.3   Additional components

A new rotation stage was ordered for the optical-CT scanner. A new rotation stage (CR1/M-Z7K, Thorlabs Ltd., Ely, UK) was attached to a micrometre which itself was attached to the vertical travel stage (LTS-300/M, Thorlabs Ltd., Ely, UK) for improved sample positioning.

The matching tank assembled in-house consists of black Acetal walls and two high transmission windows of 7.6 x 7.6 x 0.3cm^3 (Edmund Optics, NJ, USA),
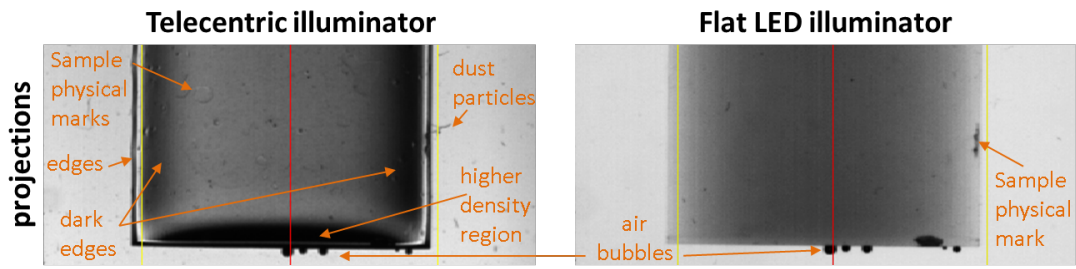
Figure 3.4: Differences in the projection images of a uniformly irradiated PRESAGE®
sample obtained using a telecentric lightsource (LTCLHP096-R, Opto-Engineering, Italy)
and a flat panel lightsource (PHLOX-LEDR-BL-100100-S-Q-IR-24 V, PHLOX, Aix-en-
Provence, France). The sample was not moved during this experiment. Several sample
features are visible on the projections imaged with the telecentric light which are not
present when a flat LED lightsource is used.

which can be removed easily in case they need to be cleaned or exchanged by new
ones. This tank is filled with matching liquid with the same RI as the samples to
reduce deflection of light at the samples' interface. The centre of the tank was
positioned at the nominal working distance of 28cm, by moving the horizontal
travel stage manually. The tank was then left in that position for all the samples
with the same diameter. After setting up the optical-CT, it was necessary to
make sure accurate 3D attenuation map could be obtained by imaging samples of
PRESAGE®.

3.4   Sample preparation and matching liquid

PRESAGE® samples are usually imaged before and after being irradiated (pre
and post-scan respectively), to measure differences only due to dose changes. The
pre-scan provides a baseline map of the OD values, removing image imperfections
coming from the sample.

Before scanning a sample, it needs to be attached to a cap so it can be
suspended on the rotation stage as shown in Figure 3.2. Two options were
available: (i) Liquid silicon glue was used to glue the sample to a cap with a flat
end face, with the sample aligned with the cap using a sleeve (Figure 3.5). This
method was used in chapters 5 to 7. Pros: more reproducible alignment between
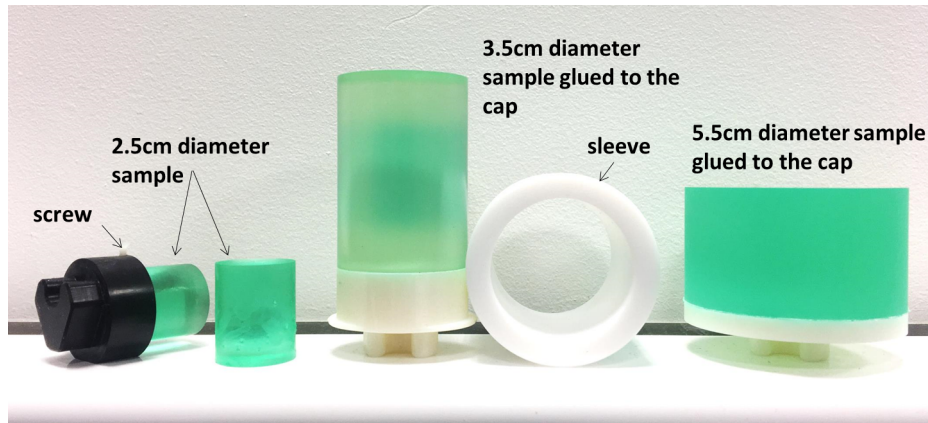
Figure 3.5: PRESAGE⟨R⟩ samples used in this thesis and the different holders attached during scanning and irradiation.

the pre and the post-scans; cons: cap present during irradiation and only one end of the sample can be scanned; (ii) Caps with an indentation that locates approximately 5mm of the sample within the cap, fixed with a screw, as shown in Figure 3.5. Pros: allows scanning both ends of the sample and irradiation of the sample without the cap, which was required for the experiments described in chapter 4; cons: less reproducible sample position in the scanner and the whole volume cannot be scanned in a single experiment.

The dosimeters are typically immersed in a transparent tank, containing a liquid having the same refractive index (RI) as the sample in order to avoid deflection of the light at the sample interfaces.

The matching liquid was created from two components: 2-ethylhexylsalicylate (99%, kosher, SigmaAldrich catalogue no W514500-10KG-K) and 4-methoxycinnamic acid 2-ethylhexylester (Chemos GmbH, Germany) mixing with a ratio of 11:1 as suggested by Rahman et al., 2011 [1]. This ratio provides a good starting point to image PRESAGE⟨R⟩ samples, which have RI of ∼1.54, but as this value is batch dependent, the final mixture is optimized for each batch. The final ratio was obtained by trial and error, by imaging a sample from a specific batch, until the edge of dosimeter is almost unnoticeable when looking at its projection images. This step is essential as different batched of PRESAGE⟨R⟩ can have different RIs. Blue and yellow oil-soluble dyes (Bestoil, FastColours, Huddersfield, UK) are

mixed with the matching liquid, until matching the colour of an irradiated sample of PRESAGE®. This way, the dynamic range of the camera is extended.

3.5   Image Acquisition

The optical-CT scans were performed following the guidelines of Doran, 2013 [56], and the images were acquired using a set of LabView® graphical user interfaces (GUIs). To precisely positioning the sample with a cap, it was connected to the rotation stage sample holder and placed inside a glass tank with the help of the electric control of the vertical stage. This step was essential as the samples require to be placed in the same position during the pre and the post-scan.

To set up the acquisition parameters and to acquire the sample projections with the optical-CT, a set of in-house LabView ® applications were used. For all samples in the thesis, a 1000 projection images were obtained while rotating the sample 180°. Before every scan a light-field (LF) dataset (30 projection images of the tank with the matching liquid but no sample) and a dark-field (DF) dataset (30 projection images taken with the lens covered) were acquired and used to correct light non-uniformities and thermal noise [114], respectively following the equation:

$$correctedProjections(x,y) = log_{10}\frac{LF(x,y) - DF(x,y)}{projections(x,y) - DF(x,y)} \qquad (3.3)$$

Corrected projections were then reconstructed in IDL with filtered back projection and the Ram-Lack filter. The final reconstructed images were exported to Matlab® where the images were analyzed.

3.6   Telecentric image acquisition optimization

After assembling the optical-CT shown in Figure 3.2, it was necessary to make sure the acquisition settings were optimized. To do this, PRESAGE® samples

were used as tests objects to refine the acquisition parameter (e.g. camera binning, exposure time vs light source) to obtain reliable reconstructed images free from unexpected artefacts. I used both irradiated and non-irradiated samples for this process. The lightsource was initially tested in terms of stability over time showing an increase in their intensity over the first 60 minutes and stabilizing after that. This effect was observed but no data was acquired.

The acquisition setting applied to read-out samples using the microscopy optical-CT were applied as a starting point to scan irradiated samples of PRESAGE® at the telecentric optical-CT. All samples imaged with the microscopy optical-CT were scanned with a camera binning of 2 x 2 and the lightsource voltage adjusted so that the dynamic range of the image would have a maximum of 30000 pixel values (this is a relative value for our particular camera). Binning consists of combining small pixels into larger pixels to get a larger signal, trading the spatial resolution of the images for an increase in signal-to-noise ratio. To optimize these settings for the new optical-CT system, the effect of selecting different camera binnings and changing the lightsource voltage was initially investigated.

3.6.1   Camera binning selection

When connected to the available camera, the pixel size of the projection images can range from $(47.9\mu m)^2$ to $(383.0\mu m)^2$. The pixel sizes depend on the selected binning (1 x 1, 2 x 2, 4 x 4 and 8 x 8). I tested how the selection of the binning would affect the image quality of the reconstructed images of an irradiated sample of PRESAGE®. For our application of verifying clinical radiotherapy dose distributions, even the largest binning would result in more than necessary resolution ($47.9\mu m$ for an 8 x 8 binning), as the maximum resolution given by a TPS is usually not less than a millimetre. The results are shown in Figure 3.6. The selection of a 2 x 2 binning or lower appears to be associated with artefacts at the centre of the samples. Reasons for this were not fully understood but it is suspected to be due to the presence of horizontal stripes on the projection images. These stripes usually show up when there is a overexposure of the sample in the
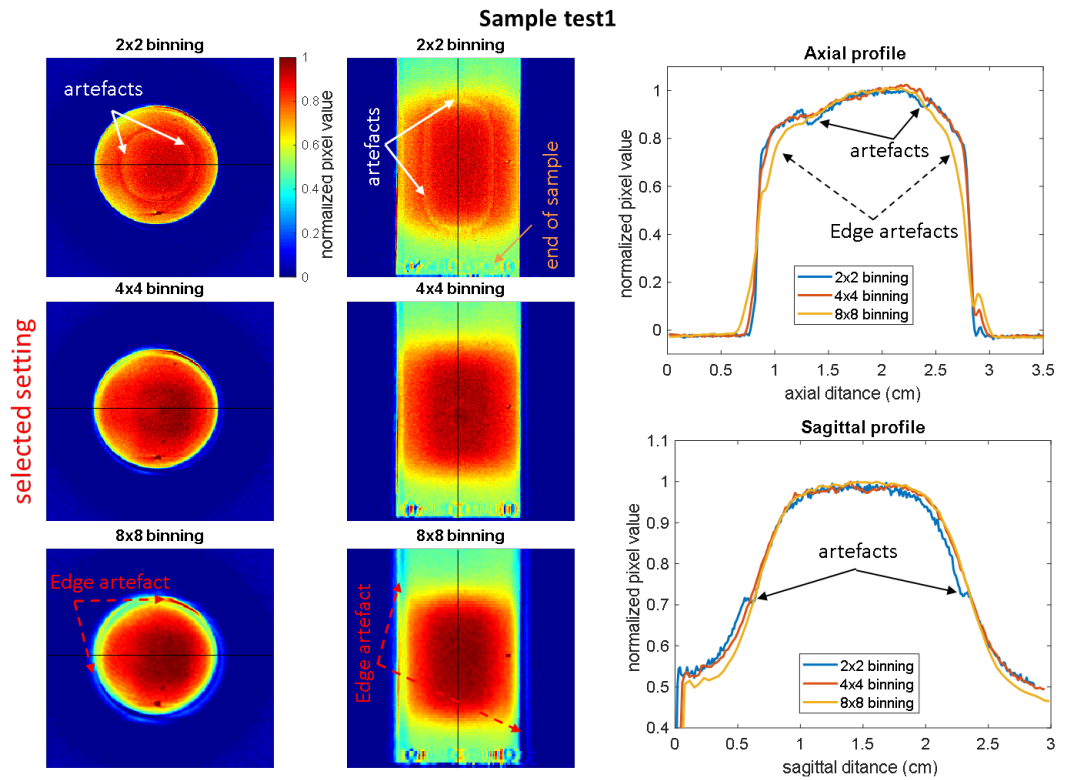
Figure 3.6: The selection of different camera binnings affect the reconstructed images of PRESAGE®. A sample with 2cm diameter and 3.5cm length irradiated with four equidistant beams to target a 1.1cm diameter cylinder was used. 2D axial and sagittal central profiles of the sample show that a 2 x 2 binning result in artefacts at the centre of the sample, which are not visible for higher binning. More pronounced edges artefacts are visible for an 8 x 8 binning. The selection of a 4 x 4 binning produced an optimal image reconstruction. The light voltage was adjusted for each in order to keep the dynamic range the same. Between scans, the sample was always taken out of the tank with matching liquid to acquire LF and DF images.

tank and result in ring artefacts on the reconstructed images. Ring artefacts can be originated by a non-uniform response of the pixels to incident light or the presence of "dead" pixels. Nevertheless, for each binning combination, the light source voltage was adjusted to maintain the dynamic range to the same maximum pixel value (30000 in this study). An alternative explanation is the lower image resolution for higher binning. By using larger binning the artefact in the middle of the sample could still be there but it was not visible when averaged. Selecting an 8 x 8 binning originated reconstructed images free from the artefact in the central region of the sample, but with additional edge artefacts (additional loss of 1mm).
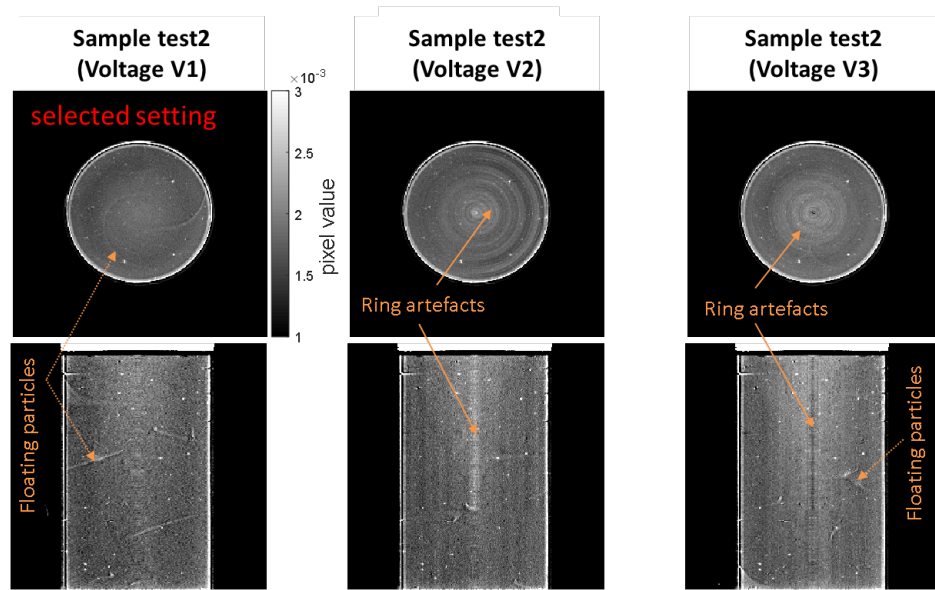
Figure 3.7: A non-irradiated sample of PRESAGE® was scanned with the lightsource at different voltages (V1, V2, and V3), which creates projection images with different dynamic ranges (max of 20000, 30000 and 57000 pixel values, respectively). 2D axial and sagittal profiles obtained at the central slices of the sample are shown. Different lightsource voltages lead changes on the reconstructed images of PRESAGE® samples. Images are displayed in greyscale for better visualization of the ring artefacts. The light diagonal lines in the sagittal views are due to particles of dust moving in the liquid and can be removed by cleaning the matching liquid.

When compared to the other binning options, scanning samples with a 4 x 4 binning produced reconstructed images with fewer image artefacts and better-defined edges when imaging non-uniformly irradiated samples of PRESAGE®. For this reason, a 4 x 4 binning was the selected setting. Note that ring artefacts (not visible in Figure 3.6 for the shown pixel value range) are still visible for all the images in the low dose regions. These artefacts can be visible in more detail in non-uniformly irradiated samples (Figure 3.7 for voltage V2).

3.6.2   Light-source voltage selection

Changing the voltage of the lightsource, and as a result, the dynamic range of the projection images, influenced the presence of ring artefacts as shown in Figure 3.7. After testing several dynamic ranges, for a 4 x 4 binning, a maximum pixel value of around 20000 was found to produce adequate reconstructed images (V1).

As previously suggested, when there is imaging overexposure, white horizontal stripes are visible on the projection images and result in ring artefacts on the reconstructed images. At higher lightsource voltages, darker horizontal stripes are visible on the projection images. By reducing the intensity of the light, these stripes start to fade. For this reason, the dynamic range of 20000 (V1), the lowest tested intensity level, was the one that produced an optimal image, free from ring artefacts.

3.6.3   Matching liquid optimization

After optimization of the binning and the dynamic range of the telecentric optical-CT, reconstructed images of irradiated samples of PRESAGE® were still displaying unexpected results. As shown in Figure 3.8h, by taking a profile along the middle of sample test3 length, different profile shapes are obtained depending on the LF used to correct the projections images. Considering that the sample was irradiated with four equidistant beams, each with a 1.5 x 3cm^2 field size, a flat profile is expected along the sample length. This was verified when the sample was corrected with a LF obtained before the scan was performed (LF initial) or, with a LF acquired 15 minutes after the sample was removed from the liquid (LF 15min after scan). The profiles difference was ~1% (Figure 3.8h). However, if the LF which was acquired 1 minute after the scan was used instead, the same profile becomes asymmetric with differences of up to 4% when compared to the other two profiles. These non-uniformities were found to be due to changes in the matching liquid, as can be seen in Figure 3.8a to f, by subtracting the LF obtained after the scan, and the one obtained before placing the sample in the tank. However, while discrepancies between the three LF projections were initially not visible (Figure 3.8a, b and c), there is a change in the pixel value created by the action of taking the sample out of the matching liquid (Figure 3.8e and f), which influences the reconstructed images. Scanning the sample after 10min (not 15min) was found to be enough (data not shown), provided that the tank is free from dust-particles and that the sample scanning position is far from the surface
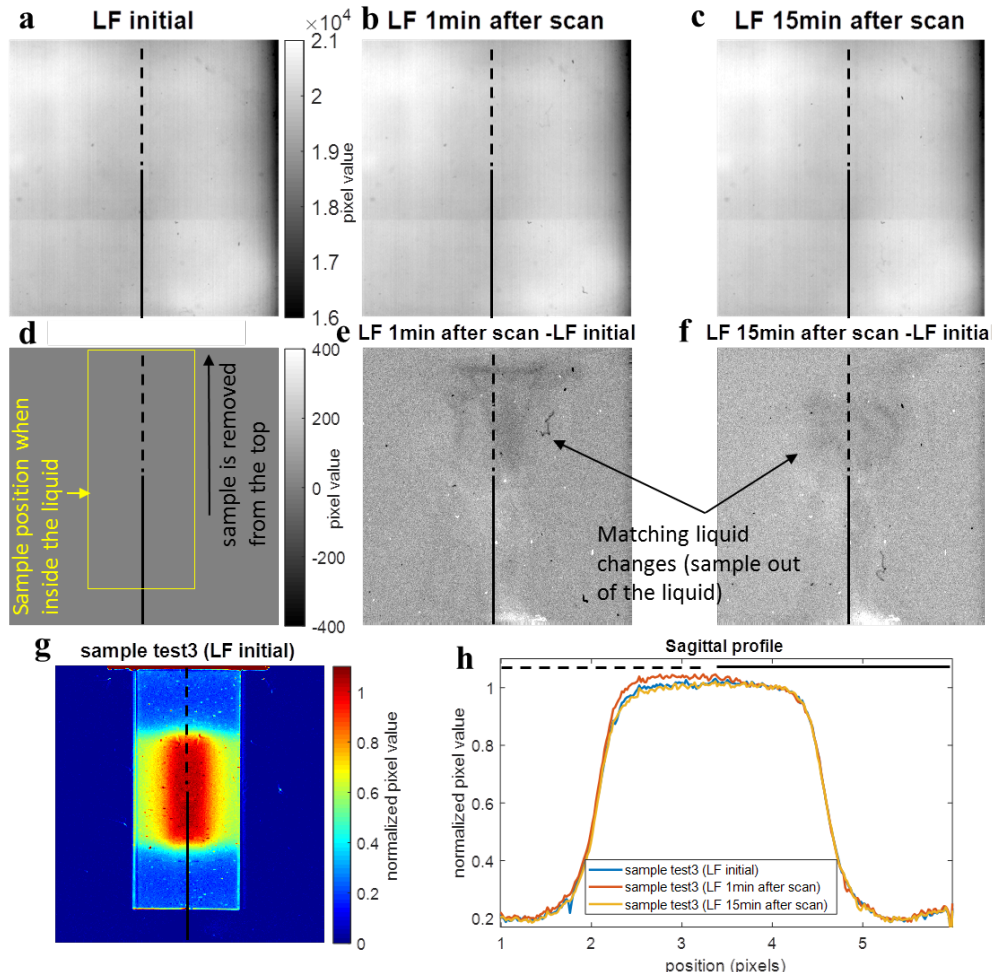
Figure 3.8: Effect of the LF in the PRESAGE® reconstructed images. (a-c) Three different LF projection images, obtained before and after scanning a sample of PRESAGE®. (d) representation of the position of the sample in a projection image, and how it relates to a LF projection. (e-f) The LF images obtained after the sample was scanned, was subtracted from the LF obtained before scanning (LF initial). (g) A sagittal 2D dose distribution is shown and (h) profiles taken along the sample length are plotted for the sample corrected with three different LF correction images. Correcting the reconstructed images using an LF obtained before or 15 minutes after scanning the sample leads to equivalent 3D dose distribution (and profiles).

of the matching liquid (at least 3.5cm to reduce the effect in Figure 3.8).

3.6.4   Optical-CT scanning recommendations

Considered the results described in section 3.6.1-3, all samples where scanned with binning 4x4, lightsource at voltage V1. Additional precautions were taken,

before and after the image acquisition, in order to reduce both noise and artefacts on the reconstructed images:

(i) The light source was always turned on at least 90 min before scanning the sample to give time for the intensity of the light to stabilize. At the same time, samples should be removed from the fridge to give them time to acclimatize to the room temperature. Temperature changes between the sample and the liquid create differences in the RI which are visible when scanning a sample. This last step minimize these differences.

(ii) Scans were only performed 10 min after placing the sample inside the matching liquid to give time for the liquid to settle. This methodology minimized changes in temperature when placing the samples inside the liquid and allowed dust particles to settle, thus reducing artefacts in the reconstructed images. The sample to be imaged should be in the middle of the tank, to avoid proximity with the surface of the liquid and the tank edges, as both subjected to RI changes. These effects are visible by by visually assessing the projection images.

(iii) Before and after each scan, samples should be wiped with a lint-free cloth with matching liquid to remove any particles attached to the sample. Particles in the liquid result in artefacts in the images (floating particles) as shown in Figure 3.7.

3.7   Conclusion

The two optical-CT scanners used in this PhD were described. A telecentric optical-CT which differs from the microscopy optical-CT in its lens and rotation stage was built and optimized to measure 3D dose distribution using PRESAGE® samples as test objects. Good practices to obtain better quality images with less noise and artefacts were also suggested.

Chapter 4

The effect of magnetic field on dose distributions - PRESAGE®️ measurements and Monte Carlo simulations

In this chapter, I performed a study to investigate the effects of magnetic field on dose distributions using PRESAGE®️ dosimeters. An initial investigation of the characteristics of these samples was done using cuvettes. A methodology was then developed using 3D samples of PRESAGE®️ and an in-house phantom placed in an electromagnet and irradiated with a Cobalt-60 (^{60}Co) source. The developed methodology is of interest to validate the TPS of the MR-linac. Part of the work described in this chapter has been published [40, 42].

4.1   Introduction and aim

The effect of the magnetic field on the dose distribution has been studied in detail with MC simulations to cover different irradiation scenarios [163, 164, 167]. The most relevant changes in the dose distribution in the presence of a magnetic field occur at the interfaces of materials with high-density differences. The experimental measurement of the simulated doses is an essential step to validate the MC calculations.

In this study, I propose the use of PRESAGE® 3D dosimeter to verify the agreement between the delivery and the calculated dose distributions at the Elekta MR-linac. When this thesis started, the MR-linac was still being installed at the RMH/ICR. Hence, a collaboration was initiated with the UK's National Physical Laboratory (NPL, Teddington, UK), where an electromagnet was mounted in a ^{60}Co unit room. This way, PRESAGE® samples could be used under the effect of a constant magnetic field, by mimicking experimental set-ups similar to the ones reported by Raaijmakers et al., 2005 [163] (see Figure 2.8a). These experiments provided a starting point to investigate if PRESAGE® samples could be used to measure doses, in particular at the interfaces were the ERE occurs.

Since the initial introduction of PRESAGE®, its formulation has undergone several changes in order to improve its stability and sensitivity to radiation [145, 146]. This means that PRESAGE® studies, even from the same group, have involved sample fabrication using different components, different ratios of the same components, and different curing conditions. This can lead to a noticeable difference in dose-response characteristics between different PRESAGE® samples [100, 108, 145], which means that every batch of these dosimeters needs to be characterized before their use. It was also necessary to understand how the samples would respond to radiation for a specific range of dose values, for the beam energy in use and if they would be affected by a constant magnetic field. At the time of this study, it had been reported that the absolute response of PRESAGE® samples was reduced by up to 12% in the presence of a 1.5T magnetic field [35,

131].

4.2 Material and Methods

4.2.1 PRESAGE® cuvettes characterization

4.2.1.1 PRESAGE® samples and readout system

Two batches of PRESAGE® from the same *Formulation* (batch 1 and batch 2) were provided by Heuris Pharma (Skkillman, NJ, USA) in the form of both 1 x 1 x 4cm³ cuvettes and cylindrical samples (Figure 4.1). A spectrophotometer (6705 Jenyway, Staffordshire, UK) was used to readout the optical density (OD) of each PRESAGE® cuvette by applying a light source at 633nm (where the PRESAGE® absorption spectrum peak is located) through the sample. The samples were always scanned before irradiation, in order to calculate the difference in OD ($\triangle$OD) only due to the dose deposition. Each sample was scanned three times to obtain the average of three consecutive readings.

4.2.1.2 Reference conditions

A total of 24 cuvettes from each batch were used to characterize the dose-response of two batches in terms of linearity, reproducibility, stability over time and energy/dose rate dependency. The effect of energy and dose rate was studied by performing the same irradiations using both an Elekta Synergy Linac (Elekta, Crawley, UK) with a 6MV beam, and a ^{60}Co unit (Theratron 780C, Theratronics, Ontario, Canada). The samples' linearity was tested by irradiating each cuvette with 2, 4, 6, 8 and 10Gy and leaving a cuvette unexposed. Irradiations were repeated twice for 2, 6 and 10Gy to study reproducibility. The OD of each sample was measured at different time points (1, 2, 4 and 6 days) after irradiation to verify changes in the $\triangle$OD over time.

Samples' irradiations were performed inside a water tank (IBA Blue Phantom, IBA Dosimetry, Bartlett, TN), with a 10 x 10cm² field and a source to surface

distance (SSD) of 95cm. Each cuvette was placed at 5cm depth with the help of a sample holder developed in-house (Figure 4.1 of PRESAGE® cuvettes). Dose output was calculated following the guidelines by Lillicrap et al., 1990 [126] using a NE2611(UK) ionization chamber.
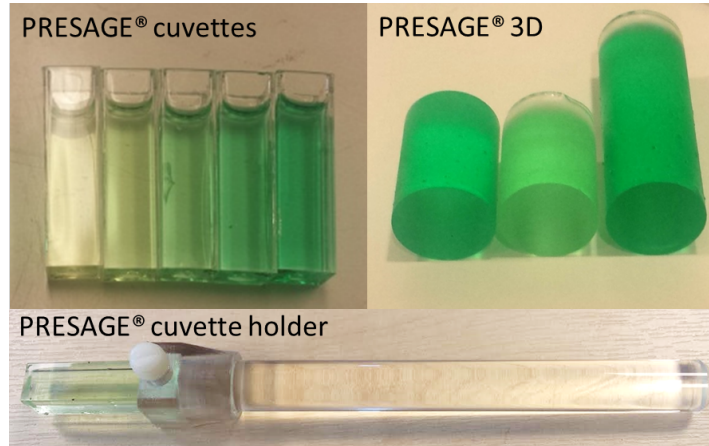
Figure 4.1: Example of PRESAGE® cuvettes and cylinders used for the characterization experiments and 3D dose measurements, respectively. An example of a sample of PRESAGE® cut in half and placed next to a full-length sample is shown. The PRESAGE® cuvettes holder was developed in house to be attached to the same holder used to position the NE2611(UK) ionization chamber within a water tank. The length was chosen so that the middle of the cuvette coincided with the effective point of measurement of that chamber.

4.2.1.3   MR-linac

When the MR-linac came into service, the effect of magnetic field on PRESAGE® sensitivity was examined by irradiating cuvettes in the MR-linac using the same set-up described in the previous section (cuvettes placed in a water tank at 5cm depth and irradiated with a 10 x 10cm^2 field), but adapted to the new isocenter position (SSD of 143.5cm). The MR-linac dose output in this conditions was 0.89Gy/MUs. This value had been previously calculated using a Farmer chamber by physicists from NPL. Two sets of experiments were performed, each using 6 cuvettes from batch 1. In the first case, the magnet was ramped down (0T), and in the second it was at field (1.5T). Samples were irradiated with doses of 2.67, 6.23 and 9.79Gy (300, 700 and 1100MUs respectively) in the centre of the cuvettes. Two samples were irradiated at each combination of dose and magnetic

field. For these experiments, the Cary 50 Bio UV-VIS spectrophotometer (Agilent Technologies, California, USA), was used by recording a spectrum three times consecutively and taking the average of the points at 633nm.

4.2.2 PRESAGE® 3D - NPL experimental set-up

4.2.2.1 PRESAGE® 3D dosimeters

Cylindrical samples of PRESAGE® (density 1.07 g.cm^{-3}) with 2cm diameter and approximate length of 5.8 ±0.2cm, depending on the sample, were created with a plastic mould made in house and shipped to the manufacturer. The resultant samples, which were made from the same formulations as the cuvettes (batch 1 and 2), consisted of a flat side (a region corresponding to the bottom of the mould) and a curved side (meniscus region corresponding to the top of the mould) as shown in Figure 4.1 of PRESAGE® 3D. The samples are firm and easily machined but contained small air bubbles on their external surfaces. The *Formulation* elemental composition was provided by the manufacturers and consisted of 62.8% of Carbon (C), 21.8% Oxygen (O), 9.1% hydrogen (H), 4.9% Nitrogen (N), 0.9% of Sulphur (S) and 0.5% of Bromine (Br).

4.2.2.2 Experimental set-up

At the NPL an electromagnet (250MM Electromagnet, GMW, USA) was installed adjacent to a ^{60}Co unit, as displayed in Figure 4.2a. The distance between the poles of the electromagnet can be modified, but was set to 5cm, which allowed the magnetic field strength to be changed from 0T to 2T by varying the electric current of the magnet. A perspex phantom was developed in house to position 2cm diameter PRESAGE® samples between the poles whilst providing enough material around the samples to guarantee electronic equilibrium within the sample (Figure 4.3a and b). The phantom consists of separate 5 x 5 x 1cm^3 slabs that attach to each other and to a 5 x 7cm^2 surface of a black Acetal base via cylindrical rods as shown in Figure 4.3b.

4.2.2.3 ^{60}Co unit MC model validation

A phase space file (ph-sp) of the ^{60}Co unit head had been previously implemented in BEAMnrc (an EGSnrc based MC code [104]) at the NPL for a given reference condition (SSD=95cm, 10×10cm^2 field). This ph-sp file was modified for a SSD=127.45cm and a 8×8cm^2 field size. These parameters were chosen so that the ^{60}Co unit beam could deliver a uniform dose in the middle of the electromagnet pole pieces. The positions of the ^{60}Co collimating jaws for the new field size were measured with a micrometer in both x (left-right) and y directions (up-down), as shown in Figure 4.2b.

To validate this new ph-sp file the BEAMnrc utility code BEAMDP [128] was used to calculate the photon energy fluence spectra, as a function of the x and y positions (Figure 4.2b) at 127.45 cm away from the ^{60}Co source (Figure 4.2c). The photon fluence profiles were compared with air kerma measurements performed with a semiflex ionization chamber (31010, PTW, Freiburg, Germany) at the same distance, and placed inside an empty water tank that had been rotated by 90° so that there was no perspex in the path of the beam. The chamber effective point of measurement was placed at 127.45cm from the source, and profiles were acquired using the omniPro-Accept 7 software (IBA dosimetry Gmbh, Schwarzenbruck, Germany) between -15cm and 15cm along both axes perpendicular to the beam. Gamma index analysis with 1.5% as dose difference (DD) and 1.5mm as distance to agreement (DTA) was applied to assess the agreement between the simulated photo energy fluence and the measurements with the ionization chamber [127].

4.2.2.4 MC simulations of the experimental set-up

A second EGSnrc user code called Cavity, a C++ based MC system [103], was used to simulate the experimental set-up described in subsubsection 4.2.2.2. The schematic of the experimental set-up used for the MC simulations is shown in Figure 4.2c. The ph-sp file generated with BEAMnrc was used as an input file for the simulations performed in Cavity, where the geometry of electromagnet
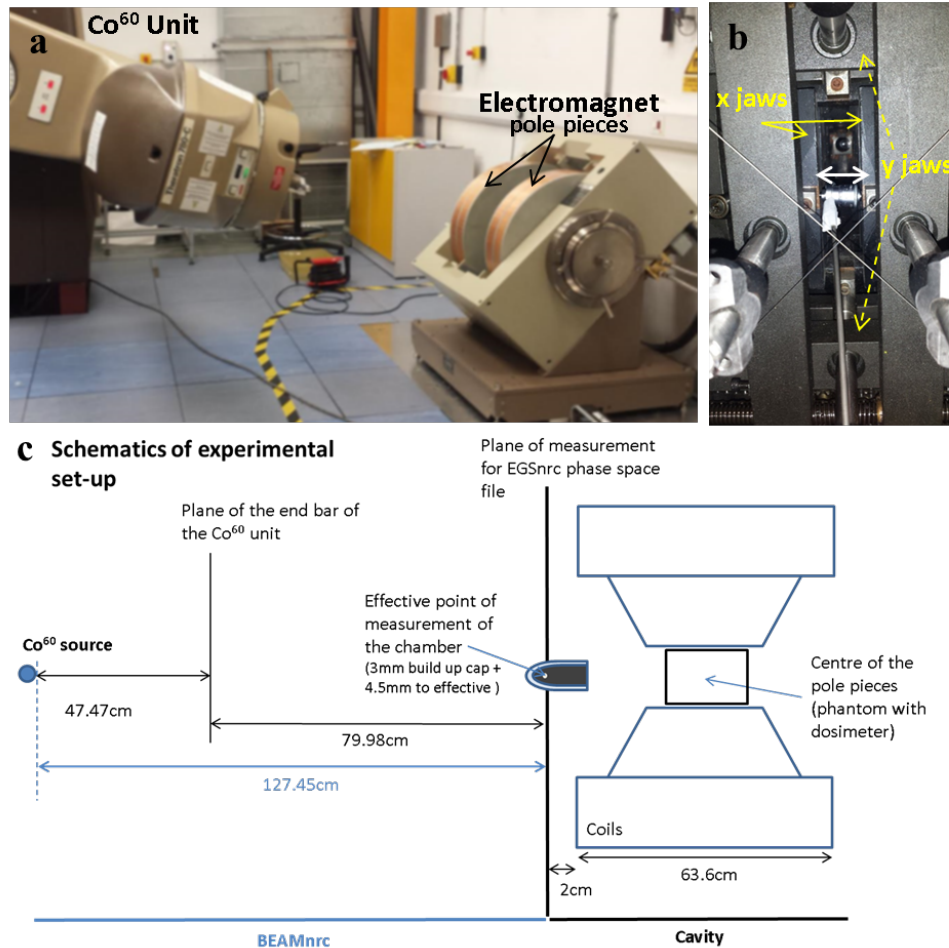
Figure 4.2: (a) NPL experimental set-up of a ^{60}Co unit in non-reference conditions. The electromagnet poles were set-up 5cm apart. A magnetometer was used to measure the magnetic flux. (b) View of a micrometer being used to measure the opening of the most external set of x jaws of the ^{60}Co unit. Arrows in white indicate the direction of the measurements performed with the micrometer in the x direction, showing the jaws in y direction completely open. (c) Schematics of the NPL experimental set-up used for the MC simulations (BEAMnrc + Cavity). The data calculated at the BEAMnrc was saved as a ph-sp file and used as the input source for the Cavity user code, where the electromagnet and the phantom geometry with the PRESAGE® samples inside was simulated.

pole pieces, the phantom and the PRESAGE® samples were simulated. Information about the materials was required to allow the calculation of the cross section data of the media. This information was obtained at the NIST website (https://physics.nist.gov/PhysRefData/Star/Text/ESTAR.html) for each material based on the density data and their elemental composition.

Simulations of two PRESAGE® cylinders oriented with their long axes parallel to the beam in the presence of different magnetic field strengths (0.5T to 2T) and different size air gaps (0.5 to 2cm) were performed to study the influence of these parameters on the dose distribution. These simulations allowed to identify the measurement conditions that would give visible changes in the dose distribution, in the ERE region, by only changing one parameter (air gap size or magnetic field strength). The length of the simulated PRESAGE® samples (i.e. total for two halves of the phantom plus air gap) were chosen based on the phantom length limitation of 7cm. One-dimensional profiles were obtained along the central region with variable sampling density, corresponding to the dose gradient along the beam direction (i.e. finer sampling where the dose changed more rapidly with distance). Voxel sizes of 0.5 x 1 x 1mm^3 and 1 x 1 x 1mm^3 were used in the build-up region (first 4.5mm of the sample) and 2.5 x 1 x 1mm^3 voxel sizes were used in the more slowly varying region distal to the depth of dose maximum. Voxels of 1 x 1 x 1mm^3, followed by 0.5 x 1 x 1mm^3, were calculated in the edge region affected by the ERE (last 3mm). Data was normalized to the centre of each simulated profile.

The transport cut-offs were set to AE=ECUT=0.521 MeV for electrons, which corresponds to the rest mass plus the kinetic energy. The photons cut-offs were set to AP=PCUT=0.01MeV. The macro provided by EGSnrc (emf_macros.mortran with EM ESTEPE = 0.02) was included in the code to simulate a magnetic field [104, 110, 129], which was homogeneous and present throughout the simulation volume.
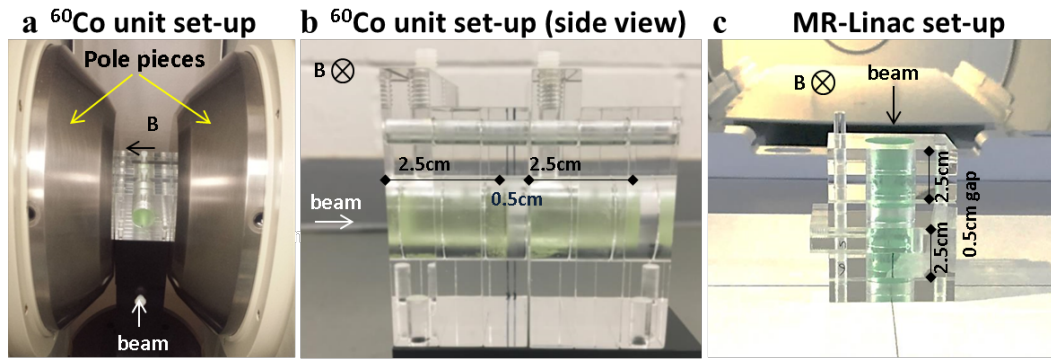
Figure 4.3: (a) perspex phantom attached to the black Acetal base and positioned between the poles of the electromagnet (5cm gap allow varying the magnetic field strength from 0 to 2T).(b) The two PRESAGE® samples (upstream and downstream samples) configuration within the perspex phantom to be placed between the electromagnet poles, at a distance of 162cm from the ^{60}Co source. (c) The same PRESAGE® sample configuration within the phantom before its placement at the isocentre of the MR-linac.

4.2.2.5 Measuring the ERE

On the basis of the simulation results (subsubsection 4.2.2.4), two sets of two PRESAGE® samples from batch 1, separated by a 0.5cm air gap, were irradiated with 3Gy (at the centre of the electromagnet poles, measured with an ionization chamber), in a 0.5T and a 1.5T magnetic fields (Figure 4.3a and b). The beam output value was determined with a NE2611(UK) ionization chamber using a chamber holder developed at the NPL to position the chamber in the middle of the poles and at the ^{60}Co unit isocenter.

Axial and sagittal 2D dose distributions were also simulated for comparison with measurements. The axial 2D distribution obtained with PRESAGE® was averaged over the last 1mm of the sample. Percentage depth dose (PDD) profiles were simulated independently with variable sampling from 0.5 x 1 x 1mm^3 to 2.5 x 1 x 1mm^3. The statistical uncertainty of all simulations was within 2% for 2D data and 1% for 1D profiles. Measured and simulated profiles were normalized to the centre of each simulated profile and compared using 1D gamma criteria analysis of 3% DD and 1.5mm DTA (3%, 1.5mm).

4.2.2.6   Optical-CT system readout

Contrary to the spectrophotometer, that gives only one OD value for each PRESAGE® cuvette, the optical-CT provides voxel-by-voxel 3D OD values of the entire sample. The microscopy optical-CT scan, described in section 3.2 was used to readout the dose distribution of irradiated cylindrical samples of PRESAGE®.

A custom-designed cap with a screw was used to position PRESAGE® cylinders within the sample holder (shown in Figure 3.5). A small mark was made with a scalpel on both the sample edges and the cap, for reproducible positioning in pre and post-irradiation scans. As the cap clamps onto the top 5mm of the sample, it was not possible to image both distal and proximal ends of the sample simultaneously. Thus, a pre-scan was performed for two separate regions of length 2.5cm at opposite ends of the sample (i.e., the sample was inverted and then repositioned), allowing both end surfaces to be imaged (see Figure 4.4 for clarification). For batch 1, the meniscus end of the samples was removed ($\leq$1cm), while for batch 2 (used in subsection 4.2.3), both ends of the samples were removed ($\leq$5mm each end).

The final reconstructed images (voxel size of 0.052mm^3) were exported to Matalb® and assembled together. The high intensity values caused by artefacts within the sample were identified and replaced by the median of the surrounding pixel values. A 5 x 5 median filter was also applied to smooth the images.
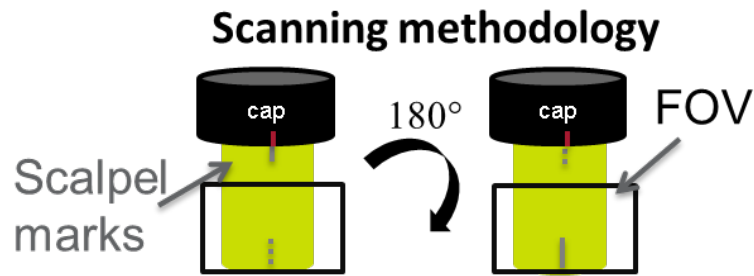
Figure 4.4: The scanning methodology, which involves taking two scans of one sample, is demonstrated. Two marks were made on the sample with a scalpel to distinguish both ends of the sample and to align with a similar mark on the cap, making sure the pre and the post scan are placed in the same position. Reconstructed 3D images are then assembled accordingly in Matlab®.

4.2.3   PRESAGE® - Elekta MR-linac

4.2.3.1   Measuring the ERE

PRESAGE® irradiations were also performed in the MR-linac when the system became available. The perspex phantom was used again to accommodate two PRESAGE® samples of 2.5cm length, separated by a 0.5cm air gap. The phantom was placed so that the MR-linac isocentre was 1cm downstream from the proximal face of the phantom, as shown in Figure 4.3c. Two irradiations were performed, using samples from batch 2, one at 0T and the other at 1.5T, with the 7MV beam of the MR-linac, with the gantry at 0°, a 20 x 20 cm^2 field and 500MUs. The samples were then scanned as described in subsubsection 4.2.2.6.

The experimental set-up was recreated in silico with CARPE DICOM (Elekta AB, Stockholm, Sweden) and simulated with 1mm resolution and 1% uncertainty using the GPU-based MC dose calculation algorithm (GPUMCD) in the research version of Monaco TPS. Measured and simulated profiles were normalized to the centre of each simulated profile and compared using 1D gamma criteria of 3%, 1.5mm.

Gafchromic EBT3 films were irradiated for comparison with PRESAGE® dose distributions as they are considered the gold standard for dose verification of clinical dose distribution. Two films with the same length and width as the

PRESAGE® samples (2.5cm x 2cm) were sandwiched between two half cylinders with the same dimensions as PRESAGE® samples and irradiated in the same conditions. Films were scanned in transmission mode, with 48bit RGB and 150 dots per inch (dpi).

The films from the batch used in this study had been previously calibrated on the MR-linac and also by a conventional linac. To do this rectangular pieces of film were placed in between slabs of a solid water phantom (type RW3 PTW-Freiburg, Germany), at 10cm depth and at the system isocentre. For each calibration curve, 6 films were used and irradiated with doses from 0 to 16Gy. FilmQA Pro software (Ashland, NJ, USA) was used to obtain a calibration curve based on the multichannel film dosimeter approach [144]. Film analysis was carried out using the same software in order to convert the pixel values to dose.

4.3 Results

4.3.1 PRESAGE® cuvettes characterization

Results of PRESAGE® cuvettes characterization regarding linearity, repeatability, dose rate/energy dependence and stability over time, for each batch, are shown in Figure 4.5. Samples from batch 1 and 2 show linearity with dose, but their sensitivity shows differences higher than 7%, highlighting how important it is to characterize each batch. Both energy and dose rate did not influence the response of the samples to dose (difference <1% when irradiated with the linac or the ^{60}Co unit). Stability over time was good in the first 2 days, showing a decrease of 1-2% in sensitivity, which becomes more accentuated 4 and 6 days after irradiation with differences of 3% to 4% respectively (Figure 4.5d).
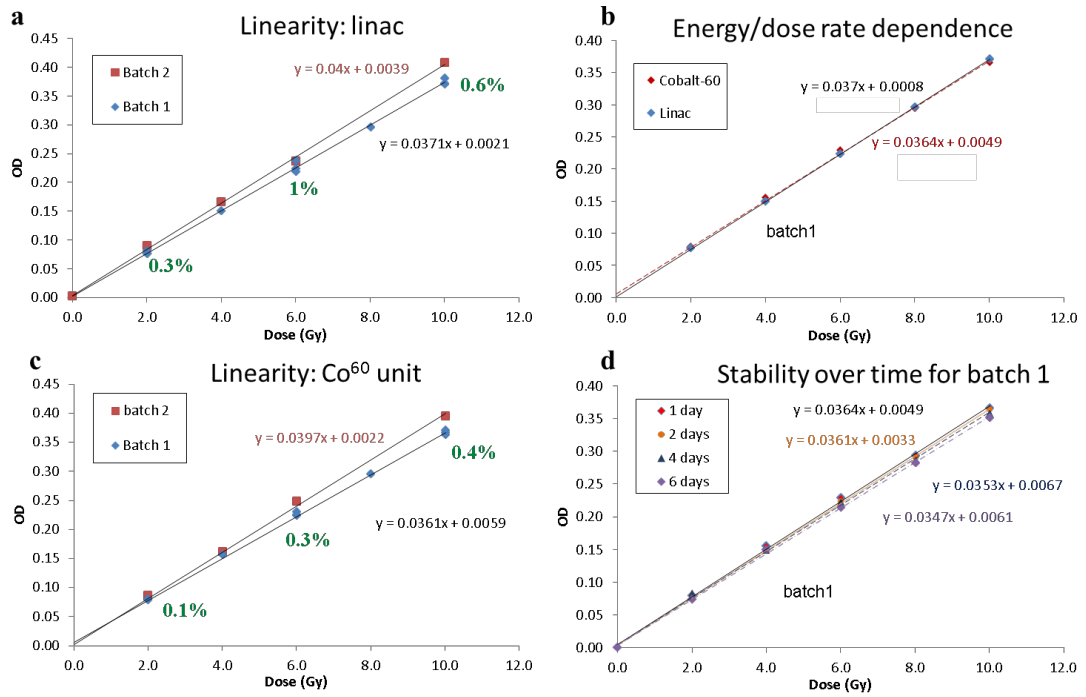
Figure 4.5: Optical density variation (ΔOD) with dose to study PRESAGE linearity (a and c), repeatability (a and c), energy/dose rate dependence (b), inter batch reproducibility (a and c) and stability over time (d). Values in green show the standard deviation of the 3 cuvettes irradiated with the same dose levels (2, 6 and 10Gy), for batch 1, to test the reproducibility of the dose response within a batch. The squared correlation coefficient for the linear fits shown in (a) and (b) for both batches 1 and 2 were $\geq$0.998.

For the experiment which tested the effect of magnetic field on the PRESAGE®, the measured sensitivities without and with the magnetic field were (0.0425 $\pm$ 0.0017)cm^{-1}.Gy^{-1} and (0.0434 $\pm$ 0.0001)cm^{-1}.Gy^{-1}, respectively, a difference of 2.1% which is within the standard deviation of the measurements (Figure 4.6).
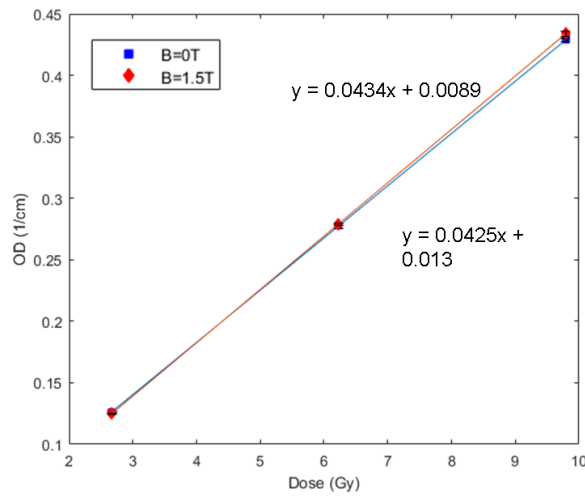
Figure 4.6: Relationship between PRESAGE⑧ cuvettes OD and absolute dose at 0T and 1.5T

4.3.2   PRESAGE⑧ 3D - NPL experimental set-up

4.3.2.1   MC simulations

The ph-sp file validation of the source model is shown in Figure 4.7. Profiles were normalized to the mean value of the central region, and showed good agreement, with 100% points passing the gamma criteria of 1.5%, 1.5mm.

Initial MC simulations of the experimental set-up showed that keeping an air gap of 0.5cm and changing the magnetic field from 0.5T to 1.5T makes a substantial difference on the magnitude of the ERE ($\sim 20\%$ dose increase at the exit region of both samples shown in Figure 4.8d). This occurs as a 0.5cm air gap is large enough for the electrons to curl back to the sample when a perpendicular 1.5T magnetic field is present (electron radius in vacuum=3.7mm), but less so when a 0.5T (electron radius in vacuum =11.2mm) is present instead, reaching the downstream sample. The same does not happen for an air gap larger than 1cm, as almost all electrons will curve back at both magnetic field strengths between 0.5T and 2T. In addition, at a 1.5T, changing the air gap from 0.5cm to 2cm or more, did not produce significant differences in the magnitude of the ERE (2-3% on the first PRESAGE⑧ sample and 5-7% on the second) as shown in Figure 4.8c.
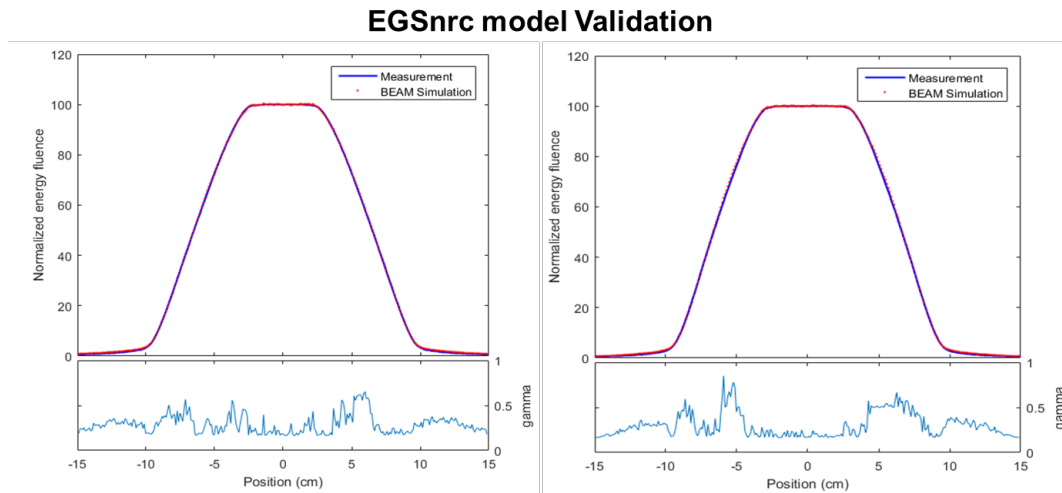
Figure 4.7: Comparison between air kerma measurements (Measurements) and simulated energy fluence profile (BEAMnrc simulations) at 127.45cm from the source, in the x direction (horizontal) and the y direction (vertical). Gamma values for 1.5%, 1.5mm criteria are also shown.

In Figure 4.8a and b an axial view of the simulated experimental set-up is also shown with and without applying a magnetic field, showing the electron path for each situation.

4.3.2.2   Measuring the ERE

Figure 4.9a and c shows a central slice from a sagittal view of the optical-CT data for two PRESAGE® samples separated by an air gap of 0.5cm, irradiated at 0.5T and 1.5T magnetic field strengths. The quality of the PRESAGE® reconstructed images was affected by artefacts caused by particles of dust in the liquid [57]. The misalignment that might have occurred between the pre and post-irradiation scan leads to an increased edge artefact and also additional noise in the data. As the OD is fairly homogeneous throughout the sample prior to irradiation, when the pre scan is subtracted from the post scan, a small misalignment (less than 1° rotation about an axis perpendicular to the plane of the images in Figure 4.9a and b and 4.11c) is not expected to influence the measured dose distribution. These artefacts can be reduced by having better quality samples and by keeping the matching liquid clean during scanning.

Simulations with and without magnetic field
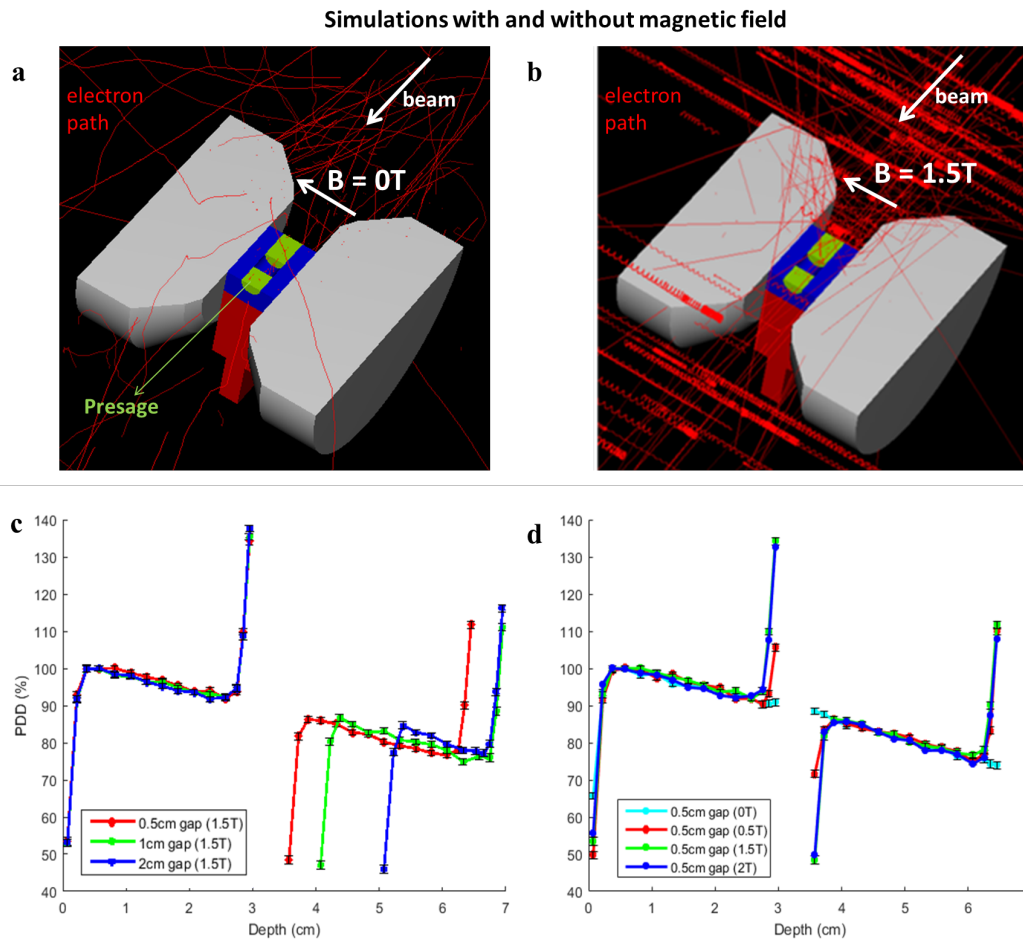
Figure 4.8: Axial cut of the simulated geometry in Cavity, showing the electron path (a) without and (b) with a 1.5T magnetic field. 1D profiles obtained by taking a central profile along the length of the two PRESAGE® samples with (c) different air gap sizes (at 1.5T) and (d) magnetic field strengths (with a 0.5cm air gap). The simulated uncertainty is given by the error bars and was always below 1% for each simulated data.

The normalized measured profiles in Figure 4.9b and d were obtained from the region of interest (ROI) shown in Figure 4.9a and c respectively. Comparison with simulated profiles showed good agreement with a gamma passing rate (3%, 1.5mm) of 99.9% for 0.5T and 99.8% for 1.5T. A sagittal 2D comparison of PRESAGE® and simulations was not possible due to the increase in the response of the PRESAGE® sample to dose at the edges.

In Figure 4.9a and c one can see that the dose increase due to the ERE is not uniform laterally within the last 2mm of the beam exit area of each PRESAGE® sample. The red region is not central but displaced upwards. This asymmetry is
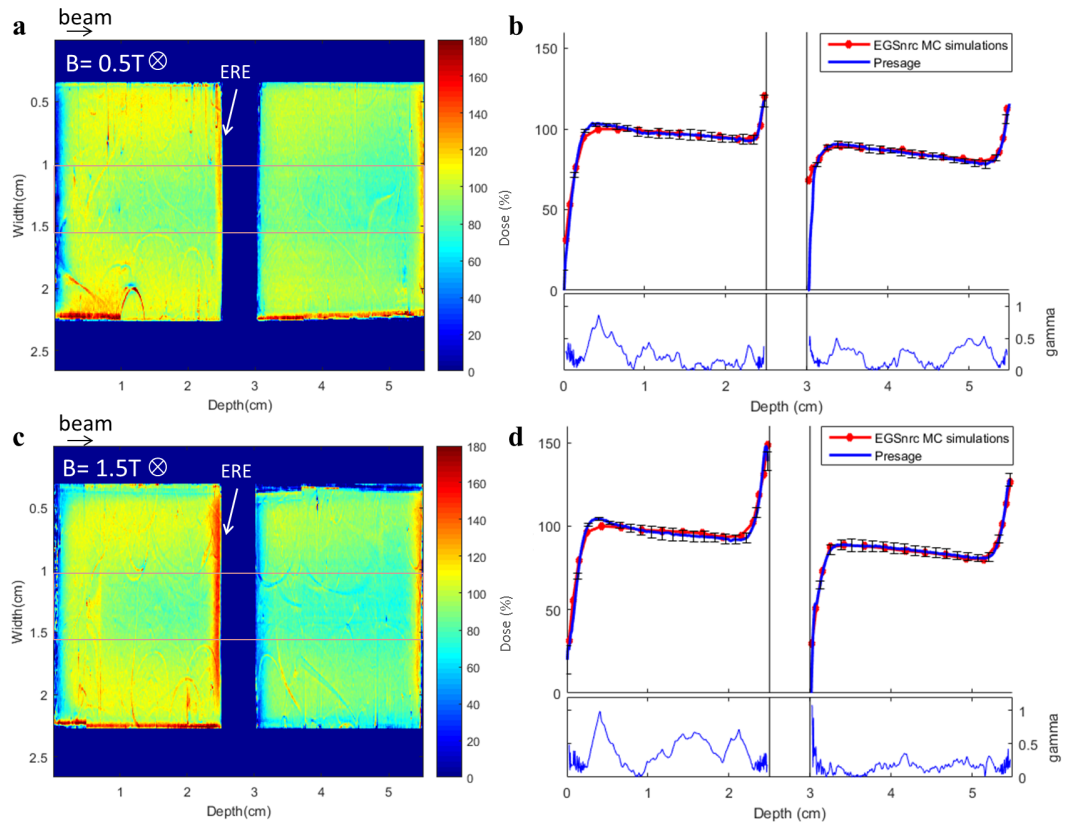
Figure 4.9: Normalized dose maps of the central sagittal slice along the two PRESAGE® samples at (a) 0.5T and (c) 1.5T, and respective (b) and (d) dose profile at the central ROI compared with simulated profiles. Error bars are representative of 1 standard deviation of the measured values within the ROI and account for readout artefacts and sample inhomogeneities. Gamma values for 3%, 1.5mm gamma criteria are also shown, in which the Monaco data was used as a reference.

also evident in Figure 4.10a and b, where the simulated and measured last 1mm axial slice of the first PRESAGE® sample irradiated at 1.5T are shown. This vertical shift is perpendicular to both beam and magnetic field, as the electron paths curve and deposit their energy at the top of the sample. This leads to a corresponding dose deficit at the bottom of the sample, and this is shown in the vertical profile in Figure 4.10c for both simulated and experimental data. By contrast the horizontal profile in Figure 4.10d presents no variation.
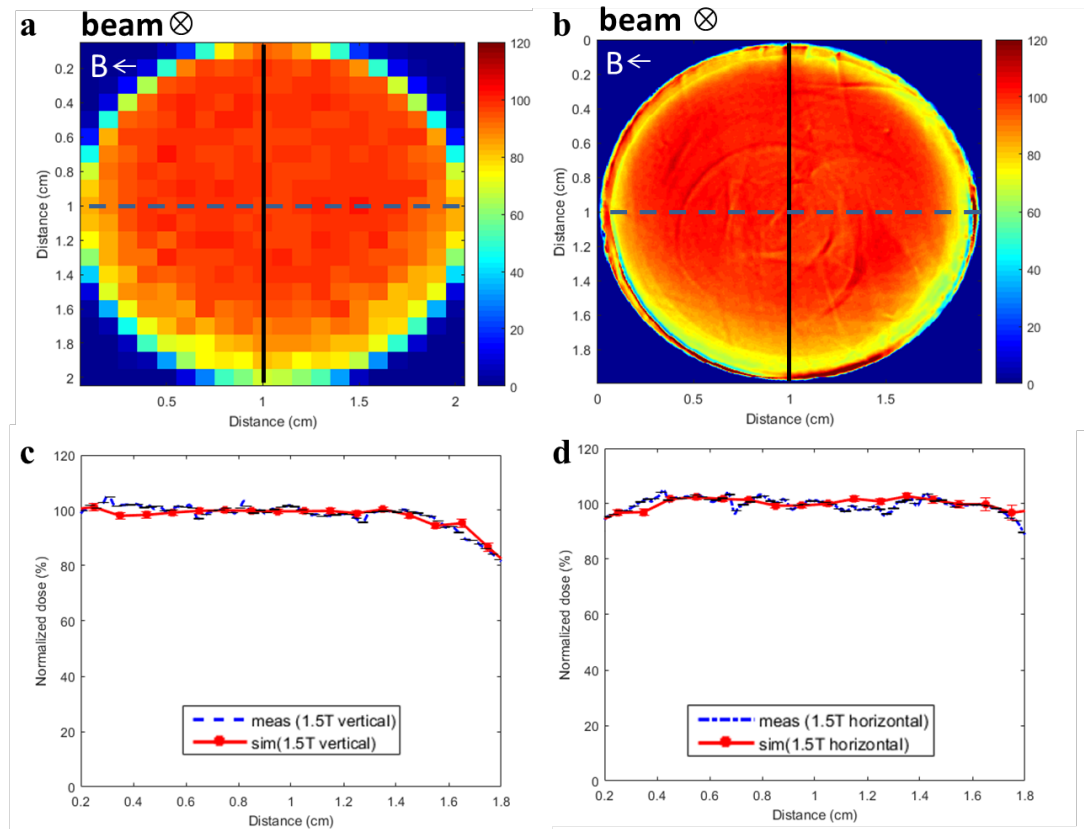
Figure 4.10: Normalized (a) simulated and (b) measured axial slice dose distribution of the last 1mm of the first PRESAGE® cylinder shown in Figure 4.9c. (c) Vertical and (d) horizontal measured and simulated profiles excluding the last 1mm edge. Error bars are representative of 1 standard deviation of the measured values within the ROI.

4.3.3 PRESAGE® - Elekta MR-linac

4.3.3.1 Measuring the ERE

Comparison between PRESAGE® and films measured profiles and Monaco TPS simulation at the MR-linac are shown in Figure 4.11b and d, based on profiles along the length of both samples. A good agreement was obtained between the profiles, given the gamma values displayed in Figure 4.11b and d. A representative normalized dose distribution and central slices from a sagittal view are shown for simulations (Figure 4.11a) and measurements (Figure 4.11c). An increase in the response of the PRESAGE® sample to dose is observed at the edges (Figure 4.11a and c).
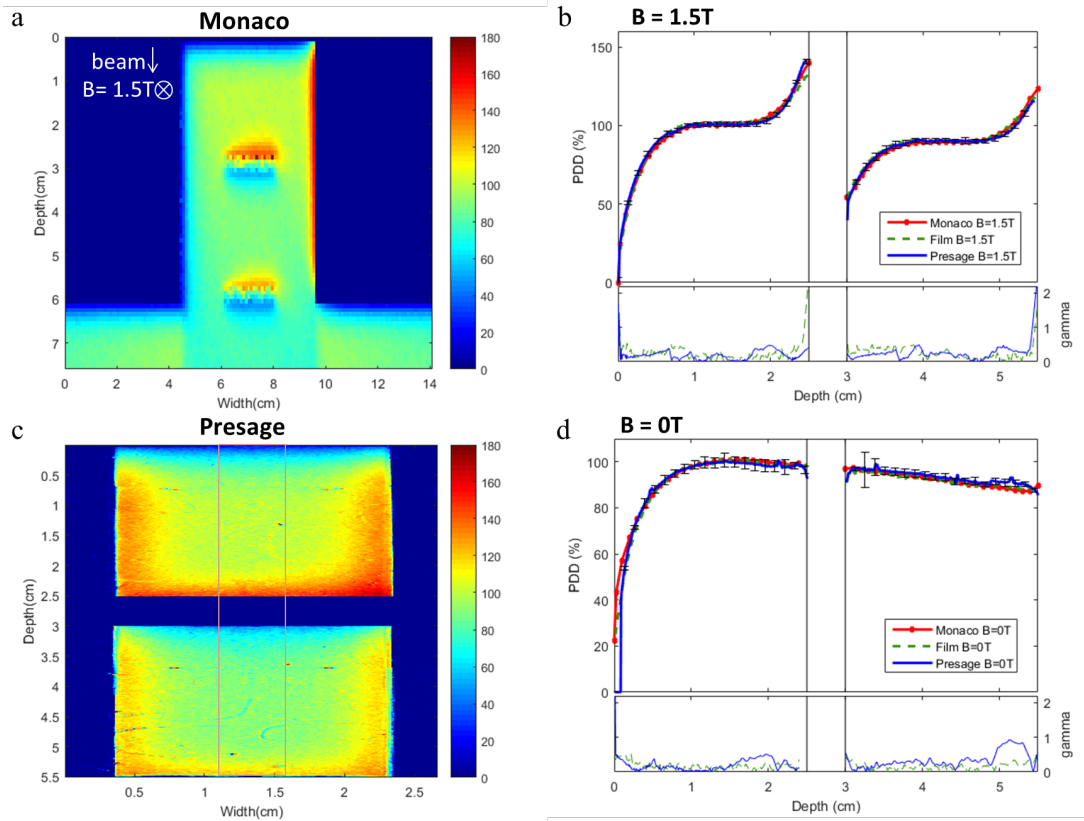
Figure 4.11: (a) Normalized dose distribution in the central sagittal plane simulated with Monaco TPS at 1.5T. The whole set-up including the sample, phantom and couch are shown. (c) Dose distribution obtained with PRESAGE® samples irradiated in the same conditions. A non-uniform response is observed at the edges of the sample. PRESAGE®, EBT3 films and Monaco normalized dose profile obtained at the central ROI at (b) 1.5T and (d) 0T magnetic field strength. Note that film profiles are overlaid by the PRESAGE® results, which highlights the good agreement between both the film and PRESAGE® measurements and the simulations. Error bars are representative of 1 standard deviation of the PRESAGE® measured values within the ROI. 1D gamma values for 3%, 1.5mm gamma criteria are also shown, in which the Monaco data was used as a reference.
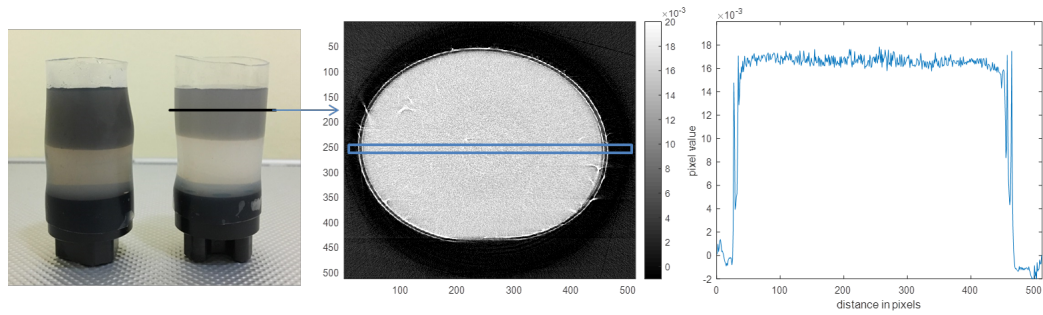
Figure 4.12: Picture of the agarose gels made to understand if the darkening at the edges of the PRESAGE® samples were due to an optical effect. Axial reconstructed image of an agarose gel and respective axial profiles. Unlike PRESAGE® samples that show higher pixel values at the edges, agarose gels displayed flat profiles.

In order to understand this dose increase I made agarose gels with different concentrations of dye in order to mimic different levels of irradiation (Figure 4.12) [134]. The gels were scanned immersed in water using the optical-CT. Reconstructed images show uniform pixel values for the same concentrations of dyes.

4.4   Discussion

4.4.1   PRESAGE® cuvettes characterization

Cuvettes irradiations provide a simple and quick way to study the characteristics of two batches of PRESAGE®. Both batches showed high linearity with dose and reproducibility (within 1% standard deviation) and were not affected by the dose rate or the beam energy (<1% difference in sensitivity). These results are in agreement with previously published data by Guo et al., 2006 [75] who have shown good PRESAGE® reproducibility (<2% variation), high linearity between OD and absorbed dose, and small dose rate/energy dependence (2%).

I showed that PRESAGE® samples are adequate for measuring relative dose distribution at the MR-linac, due to their high linearity and reproducibility with dose. They are not dose rate and energy-dependent, which means the developed methodology at the NPL, using 3D samples of PRESAGE®, could be performed easily at the MR-linac (Figure 4.11). More importantly, was to

understand the sensitivity of PRESAGE® to the presence of a magnetic field. In this thesis, a difference of 2.1% in the sensitivity of the samples at 0T and 1.5T was obtained. This is of the same order as the mean coefficient of variance in the reproducibility study, suggesting that the magnetic field does not influence the sensitivity of PRESAGE® samples. At the time of this study, two publications had tested PRESAGE® cuvettes absolute dose-response [35, 131] with and without a magnetic field. They reported an underdose of 9% and 10%-12% at a 1.5T field with no affect on the samples linearity. Nevertheless, a more recent study reported that samples irradiated with doses up to 5Gy are not affected by a 1.5T magnetic field, which is in agreement with the obtained results in this thesis [121].

The two batches were found to have a distinct response to doses, showing a difference in sensitivity in the order of 7%. This was expected, considering that PRESAGE® samples can be manufactured with different percentages of the same (or different) components. Samples from batch 1 decreased in sensitivity 4 and 6 days after being irradiated. The same was not studied for batch 2 due to the lack of available samples. Therefore individual characterisation of each batch is required before absolute measurements can be made with these dosimeters.

4.4.2   PRESAGE® 3D dosimeters

Cylindrical samples used in this study (Figure 4.9a and b and Figure 4.11c) displayed an increase in the response to dose from the centre to the edges of the sample ("cupping effect"). These results cannot be explained based only on the experiments performed in this chapter, but two potential reasons for this effect are hypothesised: (1) the well-known artefact caused by a RI mismatch between the matching liquid and the sample being imaged [56] and (2) a genuine change in the PRESAGE® sensitivity to dose at the samples' edge.

(1) The RI mismatch artefact creates a region of high intensity around the sample axial edge and, in practice, it is difficult to eliminate it completely. The artefact might have been increased by the presence of nubs/bubbles on the

PRESAGE® axial surface, making it harder to match the RI of the liquid with the sample. According to the manufacturer, the bubbles are generated during manufacturing as a consequence of the low levels of moisture interacting at the interface between the mould surface and the curing polyurethane. Better quality samples are required in the future to eliminate this problem.

(2) The increase in the dose response from the centre to the edges of the samples are likely due to a real non-uniform response of the samples. If it was due to an optical effect instead, an increase in the pixel value from the centre to the edge should have also been visible when scanning agarose gels (Figure 4.12). However, only an RI mismatch artefact was present. Different radiation sensitivities within a PRESAGE® sample have been reported before for large PRESAGE® cylinders of ∼10cm diameter, showing a 5% to 20% difference between the centre and the periphery [49]. The manufacturer suggested that the chemical manufacturing process can lead to sample inhomogeneities near surfaces. For example, due to the effect of temperature during curing of the samples, creating loss of solvent from the dosimeter edges. This results in a higher concentration of various reactants making PRESAGE® samples more reactive at the edges. The effect might be expected to be particularly pronounced in small-diameter samples, where the surface-to-volume ratio is large and might have been responsible for the slight disagreement in the initial build-up region shown in Figure 4.9b and d. The inhomogeneities are also visible in Figure 4.11. However, the build-up shows better agreement. This could be explained by the use of a different batch (batch 2), or the fact that both sample edges were physically removed from the samples in Figure 4.11) whereas for batch 1 (Figure 4.9) only the beam exit side of the samples was removed. These non-uniformities limited the use of the full 3D volume of the samples to measure the ERE. Only the flat regions of the samples were used to measure the dose changes due to the ERE. These regions did not seem to be effected by an increase in the samples sensitivity at the edges. Nevertheless, additional tests are required for a better understanding of what was observed and the implication on measured 3D dose distributions.

4.5   Conclusion

PRESAGE® in the form of cuvettes have been shown to respond linearly with dose, to be reproducible and not affected by dose rate, energy or the presence of a constant 1.5T magnetic field. The results obtained with 3D cylindrical samples of PRESAGE® demonstrated that samples can be used to study the effects of magnetic fields on dose distribution. The non-uniform response of the sample to dose and the presence of artefacts at the axial edges were not a problem for this particular study, as the ERE could still be measured accurately using the flat surface of the samples by taking relative dose profiles along the sample length. However, this study emphasizes that more work is required to improve the quality and robustness of the optical-CT measurements and to understand and characterize the non-uniform response of the samples to dose.

Chapter 5

Dosimetric characterisation and correction of the non-uniform dose response of PRESAGE® samples

In the previous chapter, I have shown that the ERE effect could be measured using the flat side of a cylindrical sample of PRESAGE® by taking a profile along the centre of the sample. However, PRESAGE® samples dose-response showed a radial non-uniformity. In this chapter, I investigated the spatial sensitivity of PRESAGE® samples to dose to determine a correction, accounting for the spatial differences, to measure dose distribution using the full 3D volume of these dosimeters. Some of the results described in this chapter can be found in the conference proceeding by Costa et al., 2019a [39].

5.1   Introduction

As discussed in subsection 2.4.6, radiochromic plastic dosimeters such as PRESAGE® do not need a container as other 3D gels, but, on the other hand, are prone to optical artefacts on their extremities. In the previous chapter (subsection 4.4.2) I explained how these effects could be caused by a refractive index mismatch between the sample and the matching liquid, or by an intrinsic non-uniform sensitivity of the sample to radiation. Until recently, it had been suggested that these effects were caused primarily by the former artefact [56] (see subsection 2.4.6). However, in the last few years, several groups using cylindrical PRESAGE® samples with large diameters ranging from 7 to 11cm have reported edge effects that appeared to be caused by a non-uniform response of the samples themselves. Jackson et al., 2015 [94] reported over-response, by a factor of 2, in the 5mm peripheral region and excluded it from the analysis. Dekker et al., 2016 [49] noted a radial increase of sensitivity to radiation, from the centre outwards, leading to an over-response at the edges of between 5% to 20% depending on the sample. Mein et al., 2017 [139] also observed a radial variation of up to 8% from the centre to the exterior surface, but only when samples were scanned 48 hours after irradiation. A radial correction based on these changes over time was proposed.

The solution of discarding about 5-7mm from the edge of a sample or only irradiating at the samples' central region, which is common practice when using PRESAGE® [24, 155, 169, 170, 177], might not be problematic when using large diameter dosimeters, but can represent a considerable loss of information for smaller samples. In addition, these options do not resolve the radial changes in sensitivity of the samples' edges mentioned by Jackson et al., 2015 [94] and by Dekker et al., 2016 [49], which means that measurements with PRESAGE® samples are restrained by their size and specific irradiation condition. Furthermore, measuring at the dosimeter's edges is still not possible, but it is of great interest not only in the field of MRgRT [163] but also for any experiment requiring measurements at the edges (e.g. lung SBRT treatment plan verification).

5.1.1 Aim

In this study, I aimed to gain a better understanding of the non-uniform sensitivity of PRESAGE® samples to radiation for the purpose of deriving a correction to permit dose measurements using their full volume. To fulfil this goal, samples were uniformly irradiated to consecutively increasing doses, in order to obtain a spatial dose-response for each sample. A calibration image was then obtained from each of these samples in order to be used as a correction for the spatial non-uniform sensitivity to radiation. These correction images were then applied to other samples of PRESAGE®, manufactured at the same time.

Samples were irradiated with 3D-CRT and IMRT plans in which measurements near the edges would be required to test the quality of the correction. The measured doses were then compared with the corresponding simulated dose distributions by applying different correction images. An alternative way to eliminate the edge effect by physically removing the samples' surface material was also investigated.

5.2 Material and Methods

5.2.1 PRESAGE® samples

A large number of samples (36 samples) from a single *Formulation* of PRESAGE® (*Formulation a*, see Table A.2) were ordered from the manufacturer and used to study intra-batch consistency, potential magnetic field effects during irradiation and both spatial and temporal variations in dose-response. Additional samples from the same order were used to test the correction methodology. Table 5.1 summarises the different samples from *Formulation a* which were used in this study. Information regarding the dose delivered in Gy, the time between manufacture and irradiation in months, and the purpose of their use is also shown.

Unlike the PRESAGE® samples used in the previous chapter, these samples were manufactured using silicone moulds to create cylinders of 3.5cm diameter ranging in length from 5.3cm to 5.9cm, depending on the degree to which the

Table 5.1: Summary of the irradiated samples, from *Formulation a*, used in this study, containing information regarding time between manufacture and irradiation, doses and the purposes for which samples were used in this work.

Sample	Interval between manufacture and irradiation / months	Dose / Gy	Purpose
a1, a2	1.7	0, 2, 4, 6, 8, 10	Uniform irradiation in conventional linac (B=0) to obtain calibration (*subsubsection 5.2.3.1*). Samples a1 and a2 were also physically modified (*subsection 5.2.6*).
a3, a4, a5	4.3	0, 2, 6, 10	
a6	8.8	0, 2, 6, 10	
a7plan	2.4	max 9.7	Exemplar studies demonstrating correction process using a standard linac (*subsection 5.2.5*).
a8plan	7.1		
a9	4.3	0, 6, 12	Uniform irradiation with physical modification of sample and measurement at the edges (*subsection 5.2.6*).
a10	4.3		
a11MRL	9.6	0, 5, 10	Uniform irradiation in MR linac (B=1.5T) to obtain calibration (*subsubsection 5.2.3.2*).
a12planMRL	9.6	max 13.2 (ERE)	Exemplar studies as above, but with irradiation in MR linac (*subsection 5.2.5*).
a13planMRL		max 8.0	

moulds were filled. The moulds were created using perspex positives, which gives a non-clear smooth finishing to the samples. Each sample had a flat base and a curved meniscus. The flat side of each sample was glued to a 3D printed plastic cap that was used to position the samples in a reproducible way during imaging and irradiation Figure 5.2a and b.

5.2.2   Optical-CT scanner readout

The telecentric optical-CT scan was used. Scanning procedures were as described in section 3.5 and following the recommendations in subsection 3.6.4. PRESAGE® reconstructed images of voxel size 0.24 x 0.24 x 0.19mm^3, were re-sampled to a more clinically relevant resolution of 0.5 x 0.5 x 0.5mm^3, for comparison with the dose distributions obtained with the TPS.

5.2.3 Investigation of the samples' spatial non-uniform dose-response

5.2.3.1 Reproducibility and time-dependence for a single formulation

As shown in Table 5.1, samples from *Formulation a* were irradiated at three different time points after their manufacture: 1.7 months (a1, a2), 4.3 months (a3, a4 and a5) and 8.8 months (a6). Samples a1 and a2 were irradiated uniformly in steps of 2Gy, receiving accumulated doses of 2, 4, 6, 8 and 10Gy. After verification of the samples' linearity with dose using samples a1 and a2, the remainder of samples a3 to a6 received only three accumulated dose levels: 2, 6 and 10Gy.

The samples were irradiated at the RMH/ICR research linac (Synergy, Elekta AB, Stockholm, Sweden), and placed inside an MP1 water tank (PTW, Germany) at 90cm SSD and 10cm depth. In order to deliver a uniform dose, each sample was irradiated with four equally spaced 6MV beams and field size of 10 x 10cm^2. The gantry was always kept at 0° and each sample was rotated by 90° between beam deliveries. This set-up was first simulated in Raystation (RaySearch Medical Laboratories AB, Stockholm, Sweden) TPS by setting a cylindrical sample of PRESAGE® to a density of 1.07 g.cm^{-3}. Dose uniformity within a sample of PRESAGE® is expected to be within 0.1% as given by the TPS dose calculation. A sample holder allow the sample to be placed completely parallel to the beam axis so no changes in dose transverse to the sample are expected.

Each sample was imaged 1 to 3 hours before the first irradiation (pre-scan) and subsequently 1 hour after each irradiation (post-scan) to control for changes in the dose-response that might be related to post-irradiation time [139].

5.2.3.2 Magnetic field dependence

Another sample from the same *Formulation* (sample a11MRL) was irradiated with the Elekta MR-linac with accumulated uniform doses of 5 and 10Gy. The same MP1 water tank was used and the conditions applied in subsubsection 5.2.3.1

were adapted here. Because the MR-linac has a bore size of 70cm in diameter
and a fixed table height, the samples were positioned at an SSD of 133.5cm, 10cm
away from the lateral side of the tank and with the gantry at 90°.

5.2.4   Correction of the spatial non-uniformity of dose response

By taking advantage of the cylindrical symmetry of the PRESAGE® samples
their linearity with dose, a spatially non-uniform dose response, is expected to be
as follow:

$$\Delta I(D, r) = m(r)D + c(r) \tag{5.1}$$

where $\Delta I(D, r) = I_{\text{post}} - I_{\text{pre}}$, with $r^2 = x^2 + y^2$, corresponds to the change in
the optical-CT value between the pre- and post-scans for a voxel with in-plane
coordinates (x, y) after irradiation to an accumulated dose D. $m(r)$ is the gradient
of the dose-response for points at a distance r from the axis of rotation of the
sample, and $c(r)$ is the intercept of the fit line.

To improve the signal-to-noise ratio of the 3D calibration images, which were
uniformly irradiated, the images were averaged longitudinally (along the sample
length). As it will be shown later, there is an edge effect of about 6 to 7mm that
extends inwards each sample (both axially and top and bottom). As samples have
different lengths, in order to avoid their top and bottom extremities, the source
data was averaged from the axial slices occupying the central 2.9cm of each sample.
This way, a 2D image was obtained for each accumulated dose. The distance r
was then discretized, and the image pixels (x, y) was assigned to radial positions.
The pixels corresponding to the same radial position were averaged in order to
get a pixel value for each radial position r. This was done for each accumulated
dose level. A straight line could then be fitted for each radial position, to obtain
$m(r)$, by plotting the pixel value as a function of the accumulated dose (i.e., a 6
point fit for samples a1, a2; a 4 point fit for samples a3 to a6; and a 3 point fit for
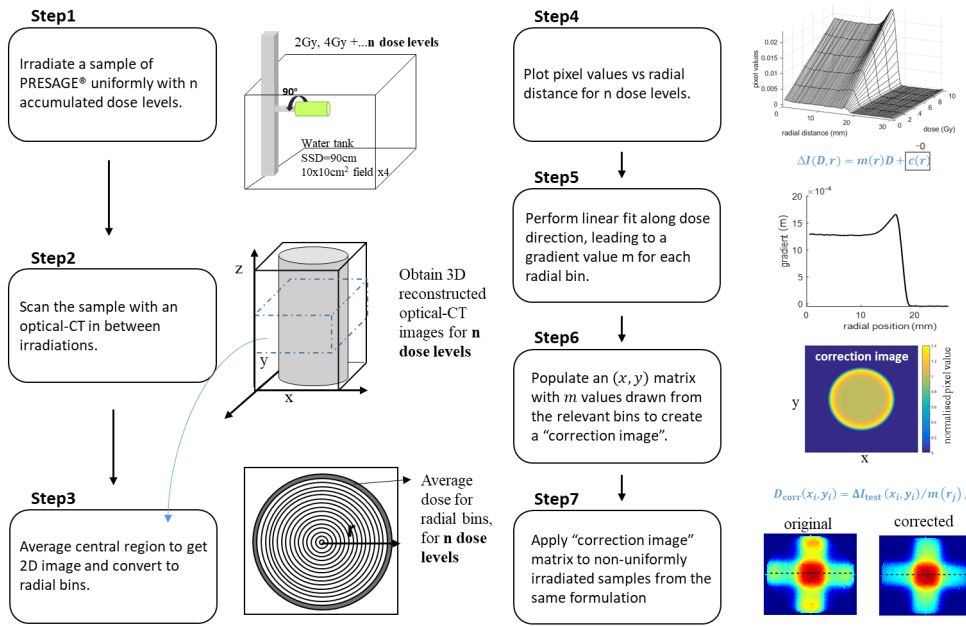
Figure 5.1: Diagram displaying the steps required to obtain a calibration image to correct for the non-uniform dose response of PRESAGE® samples.

sample a11MRL). The intercept value $c(r)$ for the fits was approximately zero, and for this reason, the value was disregarded. In practice, this consists of simply computing a 2D "correction image" by populating a matrix of type (x, y) with the m values taken from the relevant radial positions.

The resulting calibration is then applied to the measurement of a test dose distribution as it will be explained in the next section. A diagram of the steps described here, performed to obtain a calibration image to correct for PRESAGE® samples non-uniform response, is in Figure 5.1.

The resulting calibration is then applied to the measurement of a test dose distribution on a different sample from the same batch using the Equation 5.1, in which ΔI is the intensity measured with the test sample.

5.2.5   Validation of sample correction

To verify if the calibration in Equation 5.1 could be successfully applied to correct the observed samples' spatial non-uniform response to dose, samples a7plan, a8plan, a12planMRL and a13planMRL were used. To do this, each sample was

placed inside the QUASAR^{TM} MRI4D phantom (Modus Medical Devices Inc, London, Ontario) and irradiated with different dose distributions.

The QUASAR phantom, which was filled with deionized water, has two cylindrical holes, one central and one offset. A holder was created in-house to place a sample of 3.5cm diameter and 5cm length in one of the cylinders. The offset cylinder was filled with deionized water while the PRESAGE® was placed in the central insert (Figure 5.2) to facilitate phantom positioning. Motion could be applied in the SI direction with and without rotation by attaching one of the cylindrical inserts to the piezoelectric motor box. For a consistent position of the holder within the phantom, the motor box was connected to the central cylinder.

As shown in Figure 5.2a and b, a sample of PRESAGE® was mounted in the central cylinder of a QUASAR and a CT scan of the set-up acquired (Figure 5.2d and e). The sample in these Figures (Figure 5.2a, b, d and e) was used only as a dummy for the CT-scan. Both the top and the bottom edges of the sample were trimmed to keep a consistent length of 5cm. This way, the same CT scan could be used to calculate different treatment plans.

Sample a7plan was irradiated with four equally spaced 6MV beams of field sizes of 3 x 1.5cm^2 (Figure 5.2d). Two other samples were irradiated with more clinically representative dose distributions, in which 5 beams were used, and the fluence was optimized with an IMRT plan. Sample a8plan was irradiated in the research linac (Figure 5.2e), while sample a13planMRL was irradiated in the MR-linac. Sample a12planMRL was also irradiated in the MR-linac, but using a single beam (gantry at 0°), and a field size of 3 x 5cm^2, in order to observe a dose increase at the dosimeter's edge caused by the ERE. The maximum dose delivered to these samples is in Table 5.1.

All simulations were performed in Monaco TPS, with an isotropic (1mm)^3 voxel size and a 1% uncertainty of dose to medium. Both PRESAGE® reconstructed images and Monaco calculated dose distributions were normalized to the region of the maximum dose and rescaled to an isotropic voxel size of (0.5mm)^3 before being registered to each other. Sample a12planMRI was normalized to a central
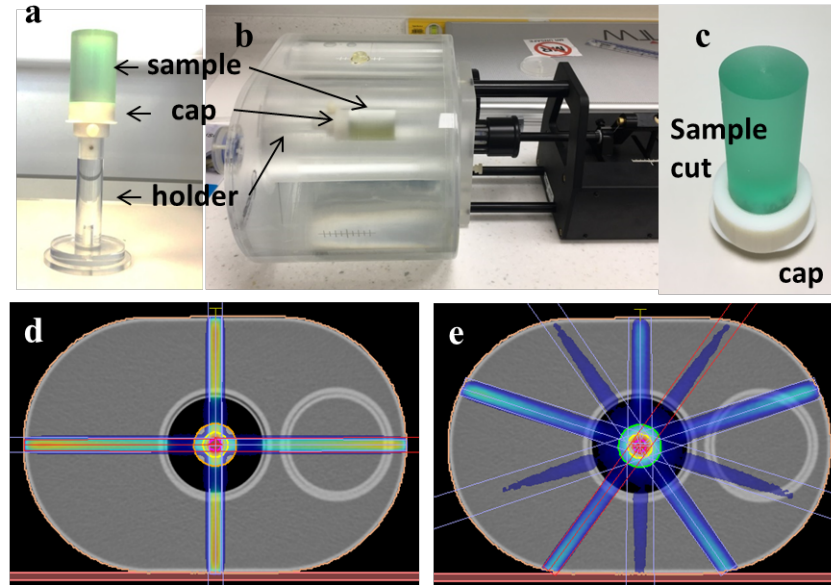
Figure 5.2: (a) Small sample of PRESAGE® attached to the in-house holder created to place it inside the (b) QUASAR phantom in a reproducible position. (c) Sample a9 after being reduced in diameter. CT scan of the phantom with a dummy PRESAGE® sample showing the dose distribution calculated with (d) 3D-CRT and (e) IMRT planning, and delivered to sample a7plan and sample a8plan, respectively.

volume value of the sample.

The correction images obtained from each uniformly irradiated samples (sample a1-a6, a11MRL), which were calculated following the methodology described in subsection 5.2.4 were applied here to correct the non-uniformly irradiated samples. To do this, each axial slice of the reconstructed 3D images of samples a7plan and a8plan, were divided by the correction image $m(r)$ of each sample (a1-a6) as per Equation 5.1, in which ΔI is the intensity variation measured with the non-uniformly irradiated sample. The same was performed for samples a12planMRL and a13planMRL which were corrected with samples a1, a6 and a11MRL.

Note that I did not attempt to model or correct the data at the top and bottom edges of the cylindrical samples, due to the distinctly curved meniscus and inconsistent length of samples supplied by the manufacturer.

After applying the correction images obtained from uniformly irradiated samples, the agreement between the experimental measurements and TPS calculations was investigated by applying a local 3D gamma criteria of either 3%/ 2mm or

2%/ 2mm, with a 10% threshold.

To facilitate the image registration between the optically obtained image and the CT scanned image, three cylindrical fiducials with a diameter and length of 1.5mm were drilled in three different surfaces of the PRESAGE® dummy sample. This way, the position of the sample could be known in both images acquired with an optical-CT and a CT scan. Both images were imported to the open-source software 3Dslicer to perform the registration between the two images to identify any required rotations and translations to be applied on the irradiated samples. This information was then used in Matlab®. Fiducials based registration is commonly used in 3D dosimetry to avoid misregistration due to artefacts inside and at the edges of the sample [8].

Gafchromic EBT3 films with the same length and width as PRESAGE® samples were sandwiched between a perspex cylinder split in half, with the same dimensions as the PRESAGE® samples and irradiated in the same conditions. The films were irradiated on a few planes for comparison with PRESAGE® (samples a7plan, a8plan and a13planMRL) and TPS simulations. Films were scanned in transmission mode, with 48bit RGB and 150dpi. FilmQA PRO was used to obtain absolute dose values, but each dose distribution was normalized to their maximal value to compare with PRESAGE® and Monaco simulations.

5.2.6   Physical removal of sample surface layer

Considering that most non-uniformities in the samples occur close to their surfaces, as I will show below, an alternative to applying a correction could be the physical removal of an outer layer from the samples. One week after the experiment described in subsubsection 5.2.3.1 sample a1 was reduced in diameter from 3.5cm to 2.5cm using a metal lathe and sample a2 was reduced in length by removing 0.6cm from the top and bottom end of the sample. Both samples were scanned 1h after being physically modified, and then uniformly irradiated with additional 6Gy and scanned again after 1h. Sample a1 was then re-scanned after 1 month, a time during which it was kept in the fridge.

To test the reproducibility of removing the outer axial edges of the sample, and to eliminate the time factor of one week between the first irradiation and the sample cutting process, an additional sample a9 was also reduced in diameter by 1cm. Moreover, to understand if measurements could be performed immediately adjacent to internal cavities, a cylindrical hole of 1cm diameter was drilled in the middle of sample a10. Both samples were irradiated uniformly in their original shape with 6Gy and scanned after 1h. They were then physically modified and immediately re-scanned. These modified samples were then once again uniformly irradiated with an additional 6Gy, before a final scan was performed after 1h.

In order to scan sample a10, the sample cavity needed first to be filled with matching liquid and then covered with tape, as otherwise, the liquid would not go inside the sample hole. This is a consequence of the samples being scanned vertically with a cap at the top, as shown in subsection 2.4.5, given the high viscosity of the matching liquid and the narrow diameter of the cylinder.

5.2.7   Alternative PRESAGE® samples' *Formulations*

The same methodology described in subsection 5.2.3 and subsection 5.2.4 was applied to investigate three additional batches of PRESAGE®, each with different percentages of solvent content (*Formulation b, c* and *d*). The content of each *Formulation* can be found in Table A.2. These *Formulations* were provided by the manufacturer after the observation of the results obtained with *Formulation a*. They have higher solvent content than *Formulation a*, as a tentative to eliminate the non-homogeneous response to dose of PRESAGE® samples. The high solvent content improves samples' stability, which, in theory, should result in less solvent loss from the sample surfaces and hence a more homogeneous spatial sensitivity to dose. The number of samples used in this study and the purpose for which they were irradiated are summarized in Table 5.2.

Table 5.2: Summary of samples irradiated in this study (*Formulations b, c* and *d*). These samples' higher solvent content is expected to have an effect not only on the spatial uniformity of their dose-response but, also on their dose sensitivity and stability over time when compared to *Formulation a.*

Formulation (solvent %)	Sample	Interval between manufacture and irradiation (months)	Dose (Gy)	Purpose
b (10%)	b1, c1, d1	0.7	0, 2, 6, 10	Uniform irradiation in conventional linac (B=0) to obtain calibration.
c (15%)	b2plan, c2plan, d2plan	0.7	max 9.7	Exemplar studies demonstrating correction process using a standard linac.
d (20%)	b3MRL, c3MRL, d3MRL	1.4	0, 5, 10	Uniform irradiation in MR linac (B=1.5T) to obtain calibration
	b4MRL, c4MRL, d4MRL	2.9	0, 2, 6, 10	

5.3   Results

5.3.1   Investigation of the samples' spatial non-uniform dose-response

5.3.1.1   Reproducibility and time-dependence for a single formulation

In Figure 5.3, an increased optical-CT pixel value is observed over the outer 6 to 7mm of sample a2, both at the top and bottom edges and radially around the sample. This shows a spatially non-uniform response of the PRESAGE® to radiation. For samples a1 to a5, the difference between the pixel values at the centre, compared to the edges, ranged from around 20% to 28% for an accumulated dose of 10Gy. The absolute differences in pixel value were smaller for lower accumulated doses, suggesting that this was not an optical artefact resulting from the optical-CT scanning process. Nevertheless, the known optical edge artefact, caused by a refractive index mismatch (see discussion in subsection 4.4.2), was still visible (see Figure 5.3c for sample a2), with its extent from the surface into the sample ranging from 0.5mm to 1.4mm depending on the sample (a1 to a5). In Figure 5.3d, the changes in optical-CT pixel values with the radial distance are shown for each accumulated dose, averaged over the central 2.9cm of sample a2.
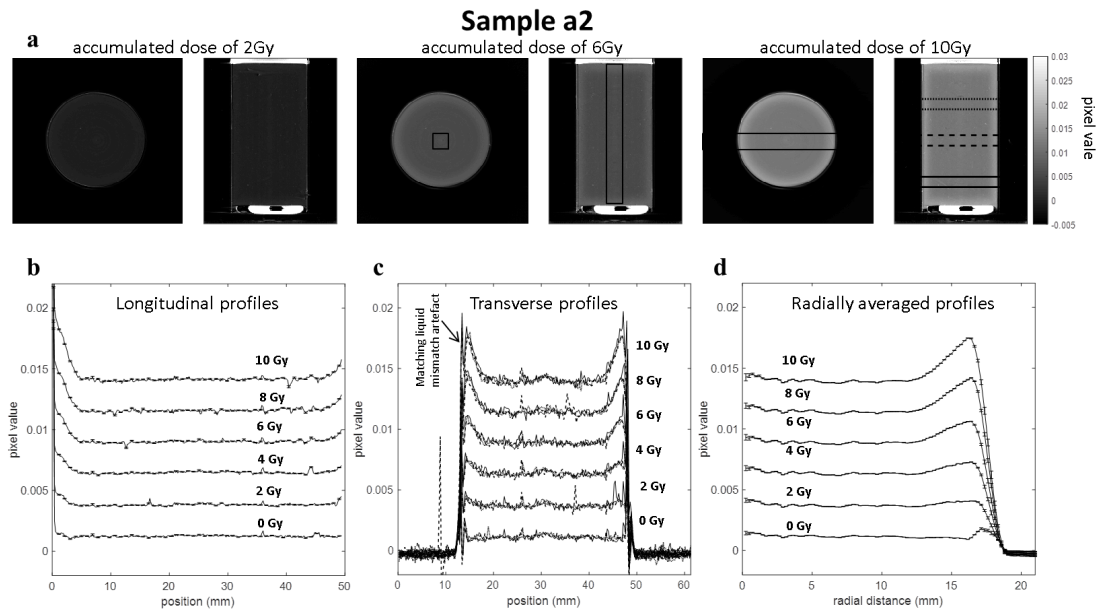
Figure 5.3: (a) 2D transverse and longitudinal slices of the reconstructed optical-CT image for sample a2 with an accumulated dose of 2, 6 and 10Gy, showing a visible edge effect. (b) Transverse profiles were obtained by averaging over the 4 x 4mm^2 cross-sectional area of a cuboidal column along the length of the sample as indicated on the 6Gy images. The error bars represent one standard error of the mean. The profiles show the results for the pre-scan and five accumulated dose levels (c) Transverse profiles were taken at different positions along the sample length, which are drawn on the 10Gy images. For each dose level, the plots are overlaid to show the small variation along the sample length. (d) Sample a2 radial average for each accumulated dose obtained by averaging the axial slices in the central region of the sample (constituting 2.9cm of the sample). Error bars represent one standard deviation of the mean of each radial distance.

Figure 5.4a shows that, at any given radial coordinate, the relation between absorbed dose and radiochromic response was linear. However, near the dosimeter edges, the slope of the fit lines increased, indicating an enhance in the dose sensitivity. Figure 5.4b demonstrates that even among PRESAGE® samples from the same *Formulation* and ordered at the same time, changes in absolute dose sensitivity, in the central region of the sample, of up to 38% are possible. These results were discussed with the manufacturer who explained that the ordered batch from *Formulation a* was manufactured in two different days. This, in theory, would result in two different sets of samples. Based on the central pixel values of the dosimeters (Figure 5.4b) two different groups are suspected to belong to
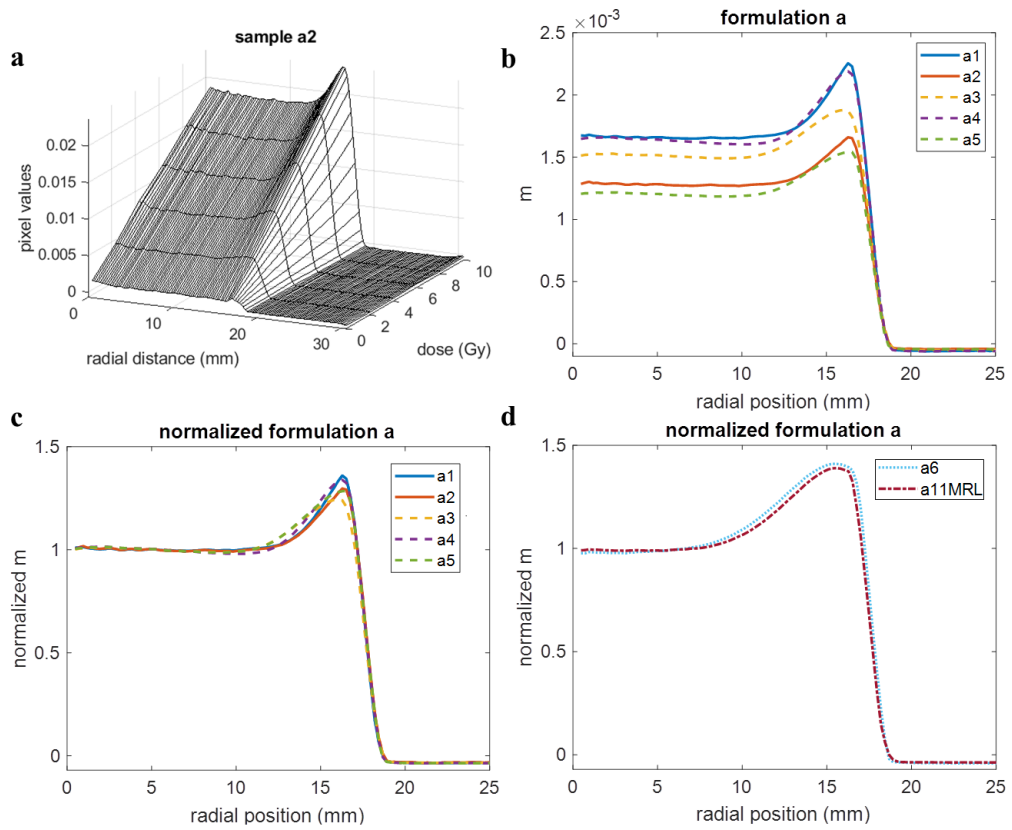
Figure 5.4: (a) Relationship between optical-CT pixel value and dose for the sample a2 as a function of radial distance. (b) Dose-response gradient (m) relationship with radial position for samples a1 to a6 and a11MRL, demonstrating both a variation in sensitivity of each sample in the radial direction and a variation in the absolute value of the sensitivity between samples. (c) Radial plots of m values, normalized to the centre of the samples, show a broadly similar pattern of relative sensitivity as a function of radial position for samples a1 to a5. (d) Radial plots of normalized m values for samples a6 and a11MRL, which were irradiated significantly later show a much more extensive edge effect.

different manufacturing dates: samples a1, a4 and a3 were likely from the same batch; sample a2 and a5 were possibly from another batch. The pixel variation between the dosimeters prevented any attempt of applying a correction that would account for absolute dose differences. For this reason, the samples' response to dose was normalized. Figure 5.4c demonstrates that, regardless of the absolute dose-response, all samples from *Formulation a* had a similar spatial variation in relative sensitivity effect. The peak value of gradient m for samples a1 to a5 could reach a difference of around 24% to 36%, depending on the sample, when compared to the centre.

All samples displayed a uniform dose response in the central volume with an increase in sensitivity at the outer edges, the extent of which depends on their age by the time they were irradiated. A quantitative measure for their similarity was found by taking the root mean square (rms) difference between the profiles of Figure 5.4c over the region of the edge effect (radial position 11 to 17mm). The rms difference between the profiles a1 and a2 is 2.9%, while the mean rms between the profiles a3, a4 and a5 is 3.9%. The mean rms considering all samples a1-a5 is 4%.

Comparison of Figure 5.4c and d shows an apparent increase in the extent of the edge effect over time that could extend from ∼6 to ∼13mm in 7 months, and was associated with a slight increase of the magnitude of the effect (difference in the gradient m peak value of ∼ 40%, when compared to the centre). By comparing samples' a1-a5 profiles with sample a6 profile, the rms differences are larger than 10%. These results highlight that care must be taken when using correction images obtained at very different time points (more than 5 months).

5.3.1.2 Magnetic field dependency

The normalized radial dose-response of two samples irradiated within a month, one at the research linac (sample a6) and the other at the MR-linac (sample a11MRL), show comparable results (Figure 5.4d). The rms difference between the two profiles of Figure 5.4d) over the region of radial position 9 to 17 mm is

3.1%, which is within what was observed for the other samples (a1-a5). These results support previous data which showed that PRESAGE® samples were not affected by a constant magnetic field.

5.3.2 Performance of the correction procedure

If no correction is applied, PRESAGE® measurements of non-uniform irradiations disagree with planning system calculations in the outer 6 to 7 mm of the sample (Figure 5.5 and Figure 5.6). For samples a7plan, a8plan, a12planMRL and a13planMRL, the maximal relative dose differences in the profiles shown are approximately 23%, 13%, 37% and 35%. For the correction image with higher gamma passing rate (see Table 5.3) relative dose differences could be reduced to a maximal error that varied between 2 and 8%. The corresponding 3D gamma passing rates (2%/2mm with a 10% threshold) improved from 90.4%, 69.3%, 63.7% and 43.6% for uncorrected images to 97.3%, 99.9%, 96.7% and 98.9% respectively when the best performing correction 2D image was applied (see Table 5.3). The best performing correction image applied was different for each non-uniformly irradiated sample.

These results show that applying any correction from sample a1 to a6 always improve the results, but performed best when there was a good match between the sensitivity profiles of the calibration and measurement samples. This meant that the time evolution of the samples, as illustrated in Figure 5.4c and d, was relevant. The data of Table 5.3 show that, for all four dosimeters, the worst performance of the correction algorithm occurs when the calibration data are derived from the sample with the largest mismatch in irradiation time from that of the test sample.

5.3.3 Physical removal of sample surface layer

Both sample a1 and a2 in Figure 5.7 and sample a9 in Figure 5.8 show that the edge effect disappeared in the regions that were physically removed, again suggesting that the edge effect is not an artefact caused by the optical scanning. The non-
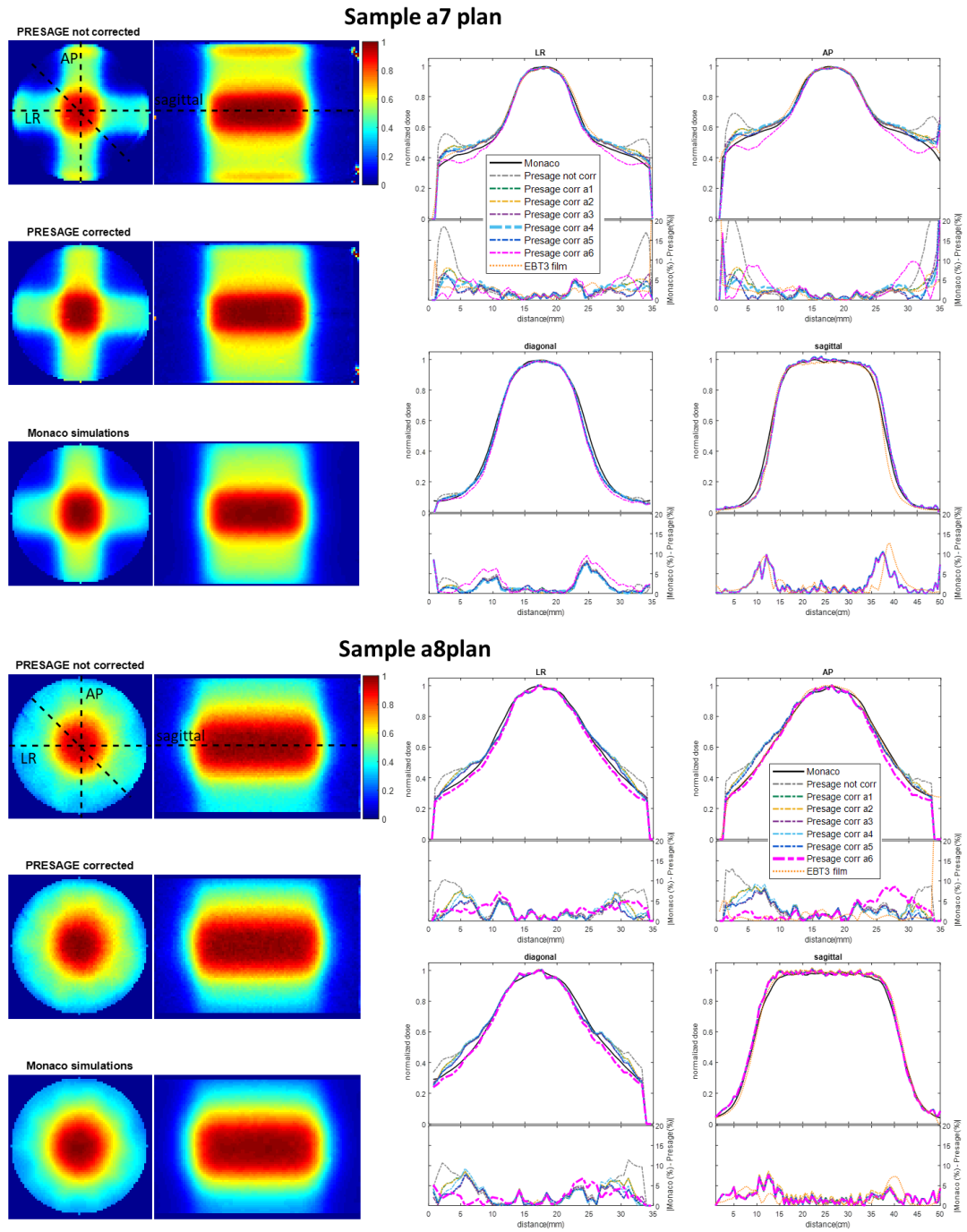
Figure 5.5: Comparison of normalized 2D axial and sagittal dose distributions, without correction and after applying a correction image based on data from six different calibration samples, for the two dosimeters irradiated in the research linac. For each profile, the measured data and the Monaco TPS output are plotted together in the upper panel. The difference between measurement and TPS for each set of calibration data is plotted in the lower panel. EBT3 films normalized profiles and respective differences when compared with Monaco calculated data were also obtained for some of the profiles for comparison. Note that the suitability of the correction image used depends on the time it was obtained. The profiles in which the correction image has a higher gamma passing rate are highlighted with a thicker line (Table 5.3).
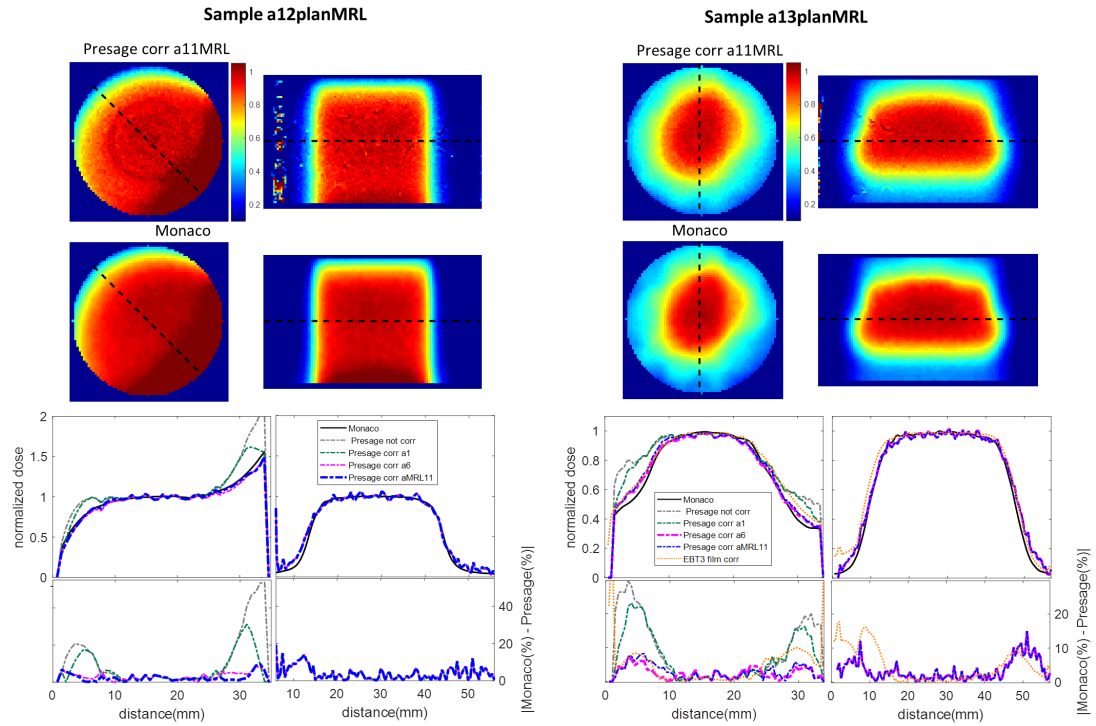
Figure 5.6: Comparison of normalized 2D axial and sagittal dose distributions, without correction and after applying correction images based on data from three different calibration samples, for the two dosimeters irradiated on the MR-linac. The sagittal 2D sample position was rotate by 90° to be representative of its position during irradiation. Plotted profiles show additional applied correction images and the respective difference between Monaco TPS and PRESAGE® (or film) normalized profiles. The artefact visible on the sagittal 2D image of sample 12planMRL corresponds to the end of the sample and was removed in the profile. Note that the quality of the correction image used depends on the time it was obtained. Sample a1 was obtained 7.9 months before sample a12planMRL and a13planMRL were irradiated, under-correcting it (Table 5.3). The profiles which correction image produced the higher gamma passing rate are highlighted by plotting a thicker line.

reappearance of the effect after the sample was irradiated with an additional 6Gy shows that newly exposed surfaces did not immediately acquire an enhanced sensitivity. Nevertheless, additional results obtained with sample a2 in Figure 5.8 suggest that the effect can reappear if a sample is irradiated after a month. Sample a10 shows that it is possible to drill a hole in the sample and still obtain valid data near the internal edges.

As long as irradiation and imaging take place shortly after the sample is modified, there is no need to apply a correction for the edges that were removed or

Table 5.3: 3D Gamma passing rates (%) applied using different criteria for sample a7plan, a8plan, a12planMRL and a13planMRL, without correction and with correction using data from different calibration samples from *Formulation a*.

Irradiation	Correction	Irradiation time mismatch (months)	3%,2mm	2%,2mm
	no corr	-	97.3	90.4
	a1	-0.7	99.6	96.4
	a2		99.4	95.4
a7plan	a3		99.2	96.4
	a4	1.9	99.6	**97.3**
	a5		99.5	97.1
	a6	6.4	98.4	92.2
	no corr	-	85.2	69.3
	a1	-5.4	100.0	97.2
	a2		100.0	97.0
a8plan	a3		99.6	98.8
	a4	-2.8	100.0	98.9
	a5		100.0	99.7
	a6	1.7	100.0	**99.9**
	no corr	-	66.7	63.7
a12planMRL	a11MRL	0	97.8	**96.7**
	a6	-0.8	97.7	96.4
	a1	-7.9	81.3	78.4
	no corr	-	45.3	43.6
a13planMRL	a11MRL	0	99.0	98.6
	a6	-0.8	99.3	**98.9**
	a1	-7.9	70.6	68.2

drilled, as the central region of the sample has a uniform response to dose. Note that, as expected, the regions of the samples that were not physically removed still displayed a visible edge effect.

5.3.4 Alternative PRESAGE® *Formulations*

Formulations b, c and *d* presented different absolute and spatial sensitivities when compared with *Formulation a*, and also between each other (see Figure 5.9a in comparison with Figure 5.4c and d). When compared to the centre of the sample, normalized gradient m values for samples b1, c1 and d1, were 23%, 29% and 34% higher on the edges. Furthermore, contrary to the samples from *Formulation a*, samples did not show a uniform central region with a well-defined edge, but rather a gradual variation in intensity from the centre to the edge as can be seen in Figure 5.9b. This is still true for samples from the same *Formulations* irradiated
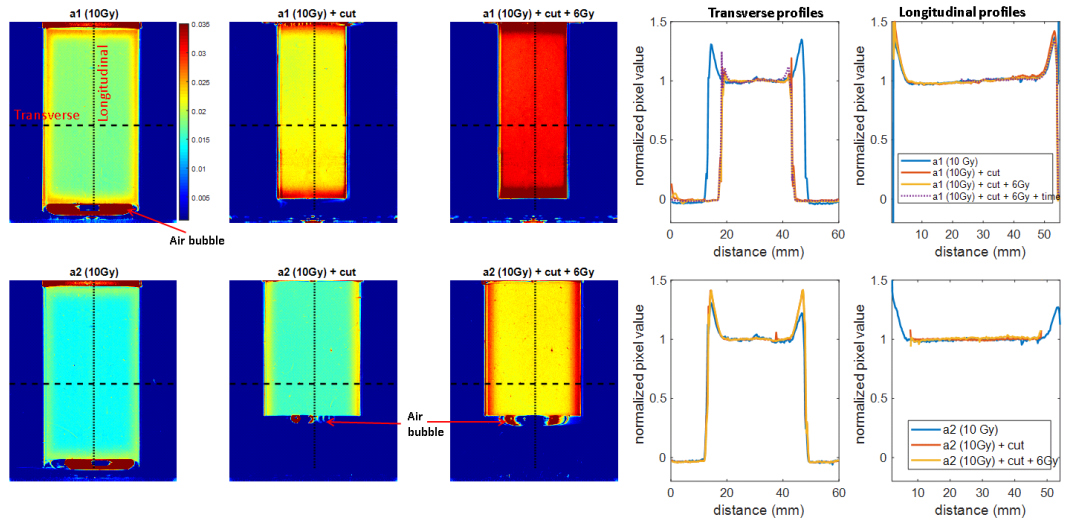
Figure 5.7: Central sagittal view of the reconstructed images of samples a1 and a2 before (a1(10Gy), a2(10Gy)) and after being physically changed (a1(10Gy) + cut, a2(10Gy) +cut) and uniformly irradiated with additional 6Gy (a1(10Gy) + cut + 6Gy, a2(10Gy) +cut +6Gy). Dose distributions are shown in absolute values to distinguish between different accumulated dose levels. Axial and sagittal profiles averaged over the middle of the samples are shown after normalization to the flat region of each reconstructed image. The profiles obtained for sample a1 scanned 1 month after the last irradiation is shown to investigate changes over time (reconstructed image not shown here). Regions corresponding to the cap and air bubble, inside the matching liquid, in the top and bottom regions of the longitudinal profiles, were not plotted for clarity.

at a later time point.

I did not irradiate samples from the same *Formulation* at equivalent time points. However, samples which were irradiated 0.7 and 2.2 months after the first samples showed an increase in their averaged absolute gradient values m (Figure 5.9d). Note that the samples "*Formulation* name + 3MRL" were irradiated at the same time as sample a11MRL (sample from *Formulation a* uniformly irradiated at the MRL (see Figure 5.5d and Table 5.1). The increased pixel value was understood as a darkening of the sample over time, and not as a consequence of the magnetic field.

The dose-response for these three *Formulations* displayed non-linearity, which became more evident for samples irradiated at a later time point (Figure 5.9c shown for samples from *Formulation d*), something which is uncharacteristic for PRESAGE®. This slight non-linearity could explain why the use of only
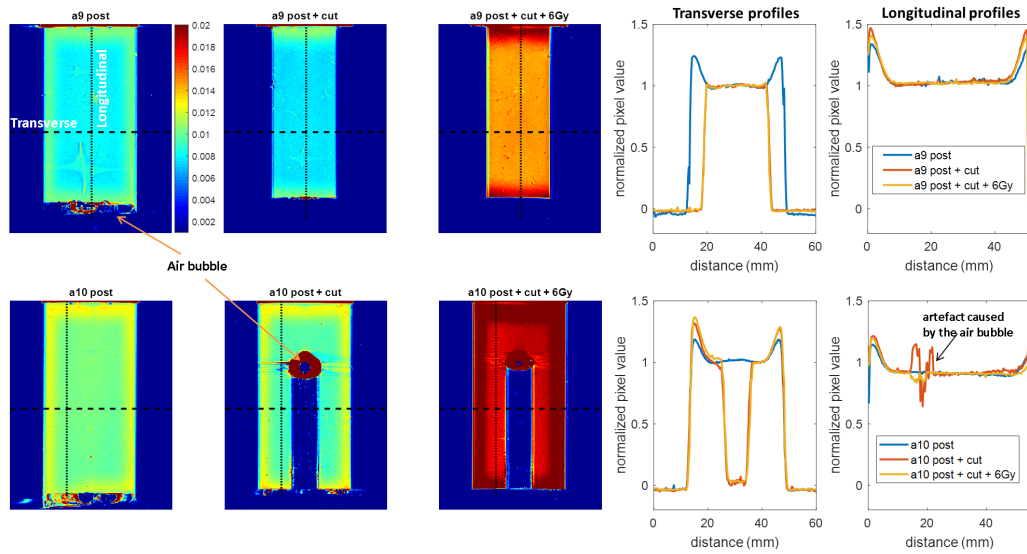
Figure 5.8: Central sagittal view of sample a9 and a10 reconstructed images before (a9 post, a10 post) and after being physically changed (a9 post + cut, a10 post +cut) and uniformly irradiated with additional 6Gy (a9 post + cut + 6Gy, a10 post +cut +6Gy). Dose distributions are shown in absolute values to distinguish between different accumulated dose levels. Axial profiles averaged over the middle of the samples are shown after normalization to the flat region of each reconstructed image

a single dose irradiation and the pre-scan cannot be used to obtain a reliable correction image (Figure 5.10b). Based on the assumption that PRESAGE® has a linear response to radiation, it should be possible to obtain a correction image with only two dose levels. This process would facilitate the methodology developed (subsubsection 5.2.3.1) but would only work when a linear response exists. Figure 5.10a confirms that for *Formulation a*, only one dose point plus the pre-scan is required to calibrate the correction. The radial average $m(r)$ is almost identical when calculated using only the pre-scan and 6 or 10Gy image, compared with the result of a linear fit to data from multiple images. The use of 2Gy results in noisy data and is not recommended. Also, as expected, for the other three *Formulations* (Figure 5.10b), the gradient value is greatly affected by the choice of the dose level used for the calibration. Regardless, improved 3D gamma passing rate are obtained when compared with no correction (Table 5.4).
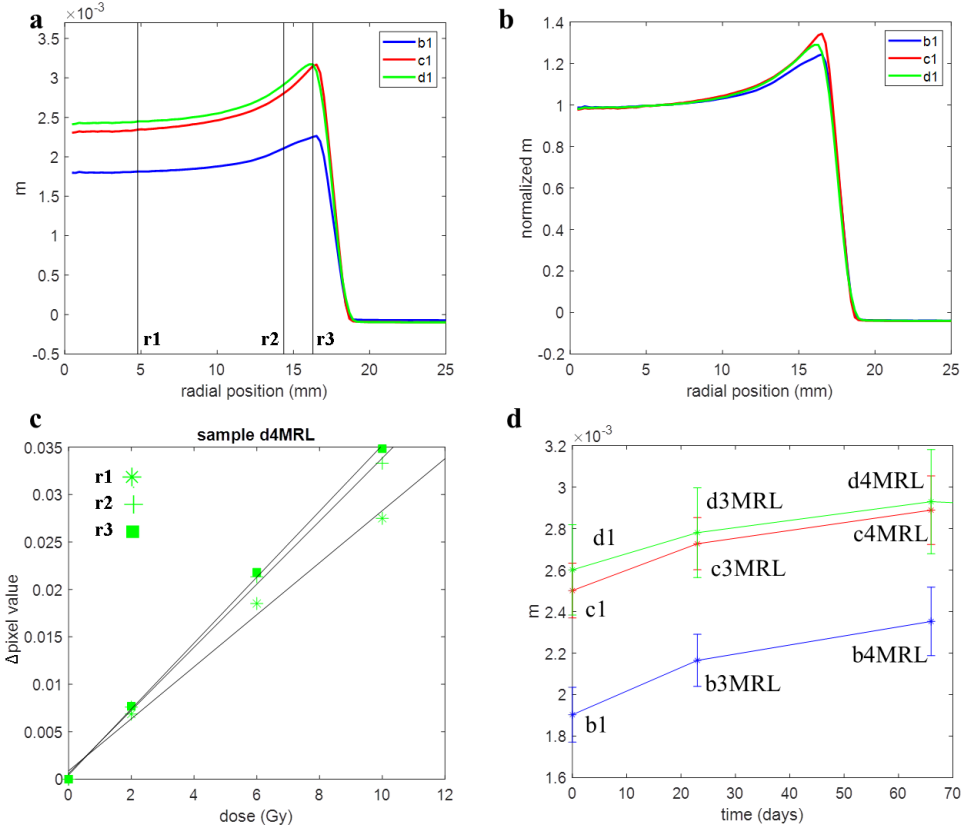
Figure 5.9: (a) Absolute and (b) normalized gradient (m) relationship with radial position obtained with samples from *Formulations b, c* and *d* in a conventional linac (samples b1, c1 and d1). The over-responses at the edges are 34%, 29% and 23% respectively. (c) Dose-response relationship for sample d4MRL, the sample which displayed higher discrepancies of non-linearity with pixel value. Visible changes do not affect the R^2 which is ∼0.99 for all the fits. (d) The relationship between absolute gradient (m) values (averaged over the samples central region) and the time of irradiation post-manufacturing for all the uniformly irradiated calibration samples. Time represents the number of days between the sample's manufacturing and their irradiation. Error bars represent one standard deviation of the gradient values found in a cylindrical subvolume of radius 1.75 cm of each sample.
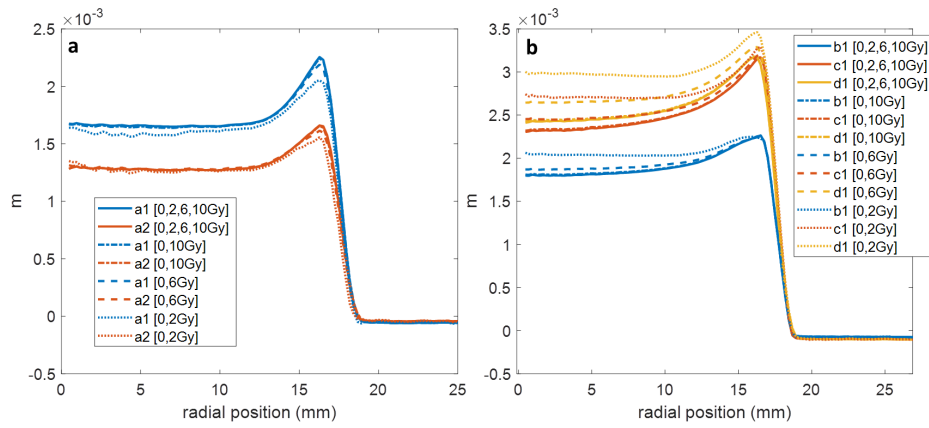
Figure 5.10: Relationship between gradient and radial position for (a) sample a1, a2 and (b) sample b1, c1 and d1 calculated based on data obtained from different accumulated doses (applying all the available dose levels or only two dose levels).

Table 5.4: 3D gamma passing rates (%) comparing simulations with measurements of sample b2plan, c2plan and d2plan irradiated with four beams forward plan and applying different criteria with a 10% threshold. Results are shown for samples without any correction and with corrections obtained from different accumulated dose levels.

Irradiation	Corrrection	3%,2mm	2%,2mm
b2plan	no corr	96.9	95.7
	b1[0, 2, 6, 10Gy]	99.8	99.4
	b1[0 10Gy]	99.8	99.4
	b1[0 6Gy]	99.7	99.3
	b1[0 2Gy]	99.0	98.4
c2plan	no corr	95.0	93.6
	c1[0, 2, 6, 10Gy]	99.7	99.2
	c1[0 10Gy]	99.7	99.2
	c1[0 6Gy]	99.7	99.2
	c1[0 2Gy]	99.2	98.7
d2plan	no corr	97.4	96.3
	d1[0, 2, 6, 10Gy]	99.7	99.4
	d1[0 10Gy]	99.7	99.4
	d1[0 6Gy]	99.8	99.4
	d1[0 2Gy]	99.5	99.2

5.4   Discussion

In this study, I developed a correction methodology based on images obtained by uniformly irradiating calibration samples that can be applied to correct the over-response of samples to dose at the samples' edges. This correction allowed to measure dose distributions at the periphery of the samples of PRESAGE®

that otherwise would not have been possible to measure. I did not attempt to apply a correction image that would account for absolute changes in sensitivity but instead, correct relative sensitivity changes as a function of the radius of cylindrical samples. The methodology was developed based on one *Formulation* of PRESAGE®, and its application was investigated for other PRESAGE® *Formulations*.

5.4.1 Samples' spatial non-uniform dose-response investigation and correction

The results shown in Figure 5.3 and Figure 5.4 illustrate that samples from *Formulation a* have a central region where there is an approximately uniform response to dose and an outer region of about 6 to 7mm, where the sensitivity to dose can increase substantially. After normalization (Figure 5.4c) the difference between the center and the edges of the samples could be up to 24 to 36% depending on the sample. The extent of this region and its magnitude change over time (Figure 5.4c and d). Retrospectively, the cupping effect observed in chapter 4, when using 2cm diameter samples, was in fact, an edge effect of about 6-7mm, as identified in this chapter.

The small difference between sample a6 and a11MRL after normalization provides evidence that irradiation in a conventional linac or at the MR-linac does not influence the spatial distribution of the PRESAGE® dose-response.

Samples of the same *Formulation a* displayed marked differences in absolute sensitivities (see Figure 5.4b). These changes are expected to occur when using 3D chemically-based dosimeters. Performing absolute dose measurements with these dosimeters is always challenging [130, 154]. The manufacture of the samples in two different days likely aggravated these differences. However, it was not the aim of the project to study this effect in more detail.

Nevertheless, applying any of the correction images to non-uniformly irradiated samples from *Formulation a* (Figure 5.5 and Figure 5.6) always improved the

agreement between the measured data and the calculated data from the TPS. As expected, and as a consequence of a presumed chemical change leading to an extension of the edge effect over time, all non-uniformly irradiated samples show better agreement with TPS simulations when corrected by a calibration image from samples uniformly irradiated at a closer time point. This is clear by looking at both profiles and 3D gamma passing rates (Table 5.3). For sample a11MRL, these results show how the correction completely transformed the ability to measure near the edges, and in this case, allowing making 3D measurements of the ERE (Figure 5.6).

Uncertainties introduced by applying this method are in the order of 4% in the edge region of 6 to 7mm as given by the rms difference between the m profiles for different radial distances obtained with samples a1 to a5. For samples older than 9 months, the edge effect extends overtime to 13mm and to differences of more than 10% when compared to the other samples' profiles. These results highlight the need to correct a sample with a correction image which is obtained at a close time point. The PRESAGE® samples' changes in spatial response to dose over time is one source of uncertainty of this method. Care must be taken when samples (to correct and be corrected) are irradiated more than 5 months apart, as differences can become superior to 4% and extend to more than 7mm of the outer region of the samples.

Other sources of uncertainty can come from the fact that although samples were manufactured with the same formulation they are from different batches. Samples from different batches have been shown to have distinct absolute dose responses. Other factors as sample position (rotation or tilt) during scanning can contribute to uncertainties in the correct determination of the edge effect. For example, a 0.1° could originate changes of 0.5% in the peak of the edge effect. The temperature of the samples during irradiation and scanning could also have created changes in the response of the samples. In the future, a systematic study, using samples from the same batch should be performed to assess how temperature affects the edge effect correction.

5.4.2 Physical removal of sample surface layer

The calibration and correction methodology demonstrated, reduced the dose measurement error at the sample edges to a clinically acceptable level. Nevertheless, it was also essential to understand if it would be possible to eliminate the errors at source. The results in Figure 5.7 and Figure 5.8 demonstrate that the physical removal of the outer edges of the samples before irradiation mitigated the edge effect on the samples from *Formulation a*. This option is a good alternative to applying a correction, provided that a sample is ordered with dimensions larger than those needed for the eventual measurement and assuming that workshop facilities are available for cutting the sample with high accuracy.

5.4.3 Sources of edge effects

In subsection 4.4.2, I have discussed two possible sources of an edge effect that would explain the dose distributions measured with PRESAGE® samples. I mentioned that it could be due to (1) the well-known artefact caused by a mismatch between the matching liquid and the samples, due to the optical scanning, and (2) a genuine change in the sensitivity of PRESAGE® to radiation. The samples from *Formulation a* are subjected to the effect mentioned in (2). The artefact mentioned in (1) is also visible in our samples but, typically, affects a millimetre or less around the edges. This artefact is challenging to eliminate, because, in practice, it is not possible to obtain a perfect refractive index agreement between the sample and the matching liquid, especially if there are temperature variations in scanning conditions.

It is important to understand that edge effects in optical-CT can also arise from (3) effects attributed to scattering, as reported by Bosi et al., 2009 [22] and (4) an artefact previously observed for highly light-absorbing samples [7] which leads to reconstructed images with lower intensity in the centre than at the edges. The artefact mentioned in (3) is not expected to affect PRESAGE® samples as the origin of its optical contrast is absorption, not scattering. Based on the results

of the non-linearity obtained with *Formulations b, c* and *d*, it seems likely that the mentioned artefact in (4) was influencing the data. Reasons supporting this statement are discussed in the following section.

5.4.4 Effect of different PRESAGE® samples' *Formulations*

It was beyond the scope of my PhD project to study the dose-response of different *Formulations* of PRESAGE®. However, it was of interest to know if the manufacturer could provide samples that would not have such spatial non-uniformity observed with *Formulation a*. At the same time, it was relevant to know if the methodology developed could be applied to these new PRESAGE® *Formulations*.

Although changing the percentage of solvent in the PRESAGE® *Formulation* led to observable changes in the spatial variation of sensitivity these samples still displayed an increase in the dose-response (Figure 5.9a and b). Furthermore, they presented non-linearity with dose in particular at the centre of the sample (Figure 5.9c) that became more evident with samples' ageing (data not shown).

This non-linearity means that correcting data on the basis of a single calibration image is not possible (Figure 5.10b). The gradual increase in the sensitivity of the samples to dose, from the centre to the edges, implies that they are being affected by the optical-CT effect mentioned in (4). This is a consequence of the high sensitivity of the samples (solvent content) which led to a quicker darkening of the samples with dose. These results do not state that the methodology cannot be applied to these *Formulations*. They reveal, however, that the dynamic range of the telecentric optical-CT was not adequate to measure the optical changes of these highly reactive samples. The process might not be straightforward, and although the investigation was not required for this study, further research should be performed in the future.

5.5   Practical guidelines

Based on the studies with *Formulation a*, I created a list of recommendations to be followed when performing measurements using PRESAGE®, mainly when measuring dose at the sample edges is of interest:

(1) Order or manufacture a batch with enough samples to use one (or more) as uniformly-irradiated calibration samples to obtain a correction image, with the remaining test samples used for the experiments of interest. All specimens should have the same diameter and should be similar in length.

(2) When possible, irradiate any calibration sample at the same time as the test samples and. If this is not possible, irradiate the samples preferably within a time-window of a month.

(3) If this is the first time irradiating a batch or specific *Formulation*, make sure artefacts caused by extremely high absorption are not present for higher doses, by testing linearity with dose using more than two dose levels.

(4) Assuming linearity, obtain the calibration data by pre-scanning the selected sample and then irradiating it uniformly, scanning the sample one hour after irradiation. I suggest using a higher dose than the maximum dose to be delivered to the test samples, to cover the full range of measurements with high signal-to-noise ratio.

(5) For each scanned and reconstructed image, exclude the top and bottom edge of the sample, and average the central slices along the sample length where there is a small variation between slices.

(6) Apply the correction image slice by slice to the irradiated test sample using Equation 5.1. The 6 to 7mm top and bottom edges of the test sample should be removed or not considered, as the correction would be accurate for those regions.

(7) If one expects to irradiate samples for a period longer than 3 months, I recommend saving a sample to uniformly irradiate at a later time point, to identify possible changes over time and possibly interpolate the correction images.

(8) For cylindrical samples with a meniscus, and inconsistent length between

samples from the same batch/*Formulation*, it is likely to be easier to trim the two ends of the sample to mitigate the edge effect, rather than attempt to model it.

5.6   Conclusion

In this study, I showed that it was possible to use the full volume of small samples of PRESAGE® to measure dose by applying a correction image obtained from uniformly irradiated samples from the same *Formulation*. This correction is essential for measurements in which changes are expected to occur at the PRESAGE® dosimeters interfaces. This is the case of measurements which are influenced by the ERE in MRgRT systems. The correction can also be employed to validate treatments such as SBRT in the lungs, where measuring near the dosimeter-lung density might be required.

Chapter 6

MR-linac adaption workflow validation using PRESAGE®

Different plan adaptation methods are available with the Elekta MR-linac for treatment delivery, which can be separated into two main workflows, the adapt-to-position (ATP) and the adapt-to-shape (ATS). This chapter proposes the use of PRESAGE® dosimeters to perform E2E tests to verify the accuracy of the MR-linac plan adaptation workflows. The phantom/PRESAGE® set-up, which was described in chapter 5, was used here to test the ATP workflow, mimicking patient displacement scenarios. The ATP and ATS workflows were then tested by simulating a prostate treatment, using larger samples of PRESAGE® with and without the presence of an air cavity.

6.1 Introduction

In subsection 5.2.5, the good agreement between PRESAGE® measurements and Monaco simulations, in both homogeneous regions and at the dosimeter-air interfaces, proved the capability of the PRESAGE® samples to measure dose distributions accurately near the edges as long as an appropriate correction was applied. The success of that study provided the confidence needed to trust the validation presented her, of the treatment plan adaptation workflows available at the Elekta MR-linac (see subsection 6.2.1). Treatment adaptation techniques increase the complexity of an RT treatment, and both spatial and dosimetric accuracy of the planned dose should be verified before starting to treat patients at the MR-linac.

Two conference abstracts studies have tested the accuracy of available adaptation workflows using MRgRT systems, by performing E2E dosimetric verifications. Ahunbay et al.,2018 [6] tested and validated with success the MR-linac ATS workflow, using an MR-MV phantom consisting of a 3D diode array. This phantom provides discrete 3D dose information and does not account for patient inhomogeneities. Hoffmans et al., 2018 [84] used films together with an anthropomorphic pelvic phantom as an E2E test to verify the MRIdian system workflow. This verification takes into account both body shape and tissue densities but does not provide complete 3D dose information. More recently, two other studies used 3D gels for dose verification of adapted RT treatments in MRgRT system [65, 158].

6.1.1 Aim

In this chapter, I performed E2E tests to verify the MR-linac workflow by mimicking treatment sites where air-tissue interfaces exist. Three studies were performed. Firstly, as a proof of concept, the ATP workflow was tested by delivering a simple IMRT plan to small 3.5cm diameter PRESAGE® samples inside the QUASAR phantom. The phantom was placed in three different positions on the table, and an adapted plan was created to account for the phantom displacement, and a

new plan delivered. The measured dose distribution was compared to Monaco simulations. Secondly, the same phantom and larger samples of PRESAGE® were used to mimic a prostate RT treatment with and without the presence of an air cavity in the rectum, to understand how accurately Monaco TPS was simulating the dose at tissue-air interfaces. Finally, the same phantom PRESAGE® set up was used without the presence of an air cavity to verify the ATS workflow.

6.2 Background

6.2.1 Elekta MR-linac adaptation workflows

At the Elekta MR-linac, the treatment can be adapted using different workflows. The main adaption workflows can be divided in the adapt-to-position (ATP) and the adapt-to-shape (ATS) methods [208], and a schematic of their differences is shown in Figure 6.1. For both workflows, a pre-treatment image (CT scan or MRI) is required together with the PTV and OAR contours and the calculated plan (original dataset). Then, before the treatment starts, an MR image of the patient on the couch is taken and registered with the pre-treatment image.

In the ATP workflow, a rigid registration is performed between the pre-treatment image and the MRI. The isocentre position is updated in the original dataset to reflect the actual position of the patient on the couch. The MLC leaves will move automatically to match the new target location. After that, the plan is re-calculated or re-optimized on the pre-treatment-CT with the original contours based on the new isocentre position.

In the ATS workflow, the plan is adapted based on the anatomy of the patient on the day of the treatment, by deformably propagating the ROIs of the delineated contours from the pre-treatment CT to the MRI of the day. The dose is then re-optimized on the acquired MRI. This workflow accounts for changes in both the target position and the anatomy of the day. Bulk electron densities (ED) are manually assigned to the contoured structures in order to create a treatment plan
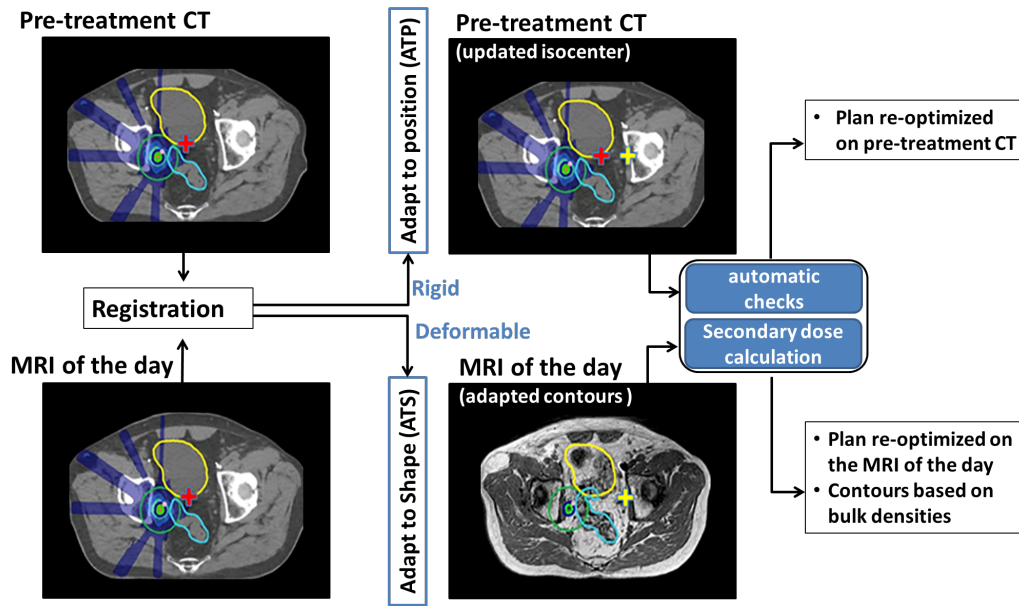
Figure 6.1: Schematic of the MR-linac adapt to position (ATP) and adapt to shape (ATS) workflows, modified from Winkel et al., 2019 [208].

using an MR image. When air cavities are present on the pre-treatment CT scan, they are overridden with tissue density.

Before a plan is delivered, automatic checks are performed and the new plan re-calculated in Raystation (secondary dose calculation). During the treatment, sagittal 2D cine images are acquired, giving information about the patient motion during the treatment.

6.2.2   MR-linac dose verification

Before the MR-linac could be used clinically, a thorough set of measurements and tests were performed during the system's commissioning. Additional patient-specific QA measurements were done before irradiating the first patient, and subsequently, every time a new treatment site was implemented. This step is essential because, as the treatment plan is different at each fraction of RT, its correct delivery cannot be verified before irradiating a patient (pre-treatment verification). At the RMH/ICR the OCTAVIUS® 4D, together with the PTW 1500 detector array (PTW, Freiburg, Germany), is the phantom used to perform these QA measurements. The process consists of verifying the dose distribution

before implementing a new treatment site at the MR-linac. Therefore, volunteers' CT scans are used to create a treatment plan for each dataset and, the dose re-calculated and delivered to the OCTAVIUS® phantom. These systems give a good indication of how accurately the plan was delivered, but they only verify the final dose and do not evaluate the entire online treatment adaptation workflow. Furthermore, they cannot deal with patient heterogeneities, like air and bone, or account for realistic body shapes.

To verify each step within the treatment workflow (ATP and ATS), E2E tests are done using a phantom (triple modality 3D abdominal phantom, CIRS, Inc., Norfolk, USA), which is visible in both CT and MRI. The test allows mimicking a patient on the couch but does not provide dose information.

6.3 Material and Methods

6.3.1 ATP workflow validation

To mimic a simplistic human torso with a tumour in the lung, the QUASAR phantom was used again together with a sample of PRESAGE® (sample a_dummy). The same phantom/PRESAGE® arrangement and treatment plan described in subsection 5.2.5 were also used here. A multimodality CT-MR fiducial (PinPoint, Beekley Medical, Bristol, CT) was placed on the flat end of a cylindrical sample of PRESAGE®. A schematic of this study is shown in Figure 6.2. A central axial slice view of the CT scan (pre-treatment CT) is shown with the five beams used to irradiate the target with a maximum dose of 9.4Gy. For the purpose of this experiment, three PRESAGE® samples were used. Initially, sample a_dummy (which was used for the CT scan) geometric centre was placed in the same position in relation to the MR-linac isocentre as simulated by the TPS. Because at the MR-linac the couch is at a fixed height and there are no lasers to position the phantom/patient in the SI direction, the phantom was placed with the help of electronic portal imaging device (EPID) images taken at gantry 0° and 90°. The

central pixel value of these images corresponds to the MR-linac isocentre. Sample a_dummy was then removed and sample a_ATP1 was positioned in its place. Therefore, the couch had to be retracted from the scanner and moved back to the same position. The sample was then irradiated with the reference plan. This mimics an irradiation at a conventional linac as the target is at the isocentre and the original reference plan is delivered (Figure 6.2).

Both samples a_ATP2 and a_ATP3 were irradiated with the phantom placed away from the isocentre using the ATP workflow of the MR-linac. Sample a_ATP2 was irradiated with the phantom placed 3cm away from the isocentre in the SI direction, while for sample a_ATP3 the phantom was moved an additional 3cm in the LR direction (Figure 6.2). A T2 weighted MR image of the phantom on the couch was taken and rigidly registered with the pre-treatment CT using the Monaco TPS. The agreement between the two was based on the phantom structures since PRESAGE® samples are not visible in MR images. The positions of the samples were inferred by identifying the fiducial shape and location in both images. This workflow updates the isocentre in the original dataset to reflect the current phantom position. The Adapt Segments option was selected. It consists of shifting the apertures of the MLC based on the CT-MR registration to account for the new position of the target. A new plan was then re-calculated on the pre-treatment CT image.

6.3.2   Prostate treatment - ATP dose delivery with and without an air cavity and ATS workflow validation

6.3.2.1   Phantom and PRESAGE® sample set-up

In this study I used larger PRESAGE® (*Formulation e*) samples, supplied by the manufacturer as cylinders of 6.05 ± 0.05cm diameter and 7.6 ± 0.2cm (Table A.2). The QUASAR phantom was again used for this study, but as opposed to the experiments described in subsection 6.3.1, where the central cylinder contained air, both cylinders were filled with deionized water.
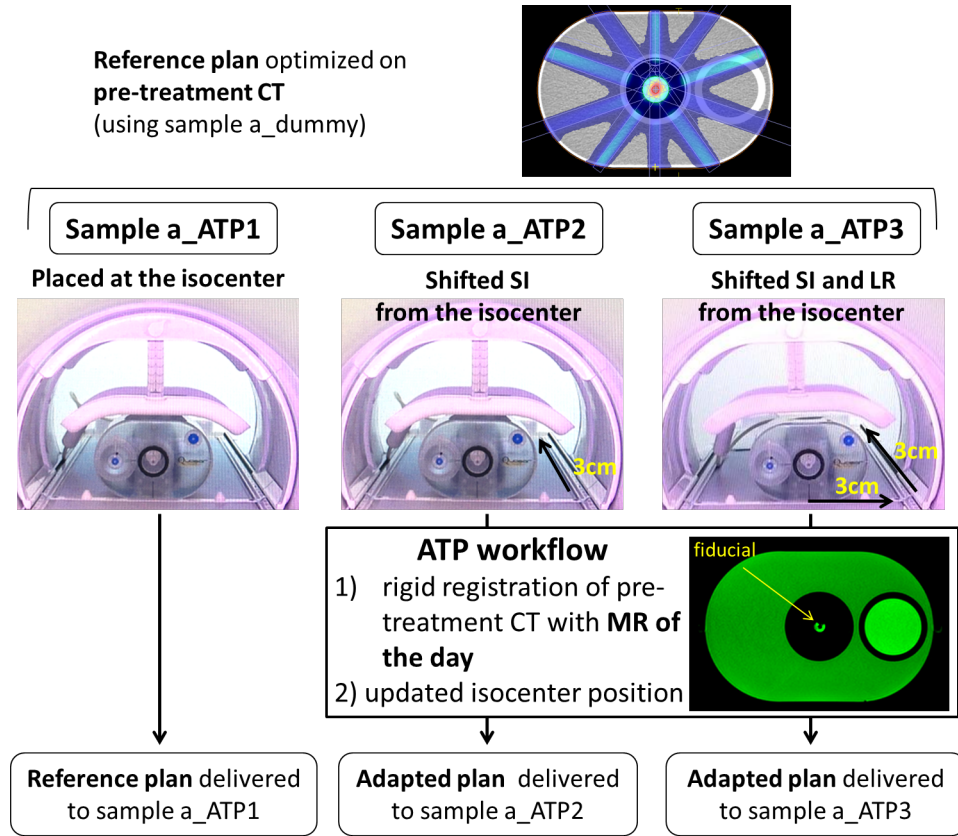
Figure 6.2: Schematics of the study performed to validate the ATP workflow. The arrows over the pictures showing the phantom on the MR-linac couch, display the direction of the motion applied.

6.3.2.2 PRESAGE® samples preparation

Before using a sample from *Formulation e*, the spatial sensitivity of these dosimeters to radiation was characterized in the MR-linac, following the methodology described in chapter 5 in order to obtain a correction image. The calibration, which was obtained by irradiating the sample with accumulated dose levels of 2, 6 and 10Gy, confirmed a linear response with dose and revealed an increase in sensitivity up to 33% edge over the outermost 6 to 7mm radially. The results are shown in Figure 6.3.

Two PRESAGE® cylinders were cut and machined to form four independent samples with the same dimensions (length 3cm and diameter reduced in a lathe to 5.45cm in order to fit inside the phantom).
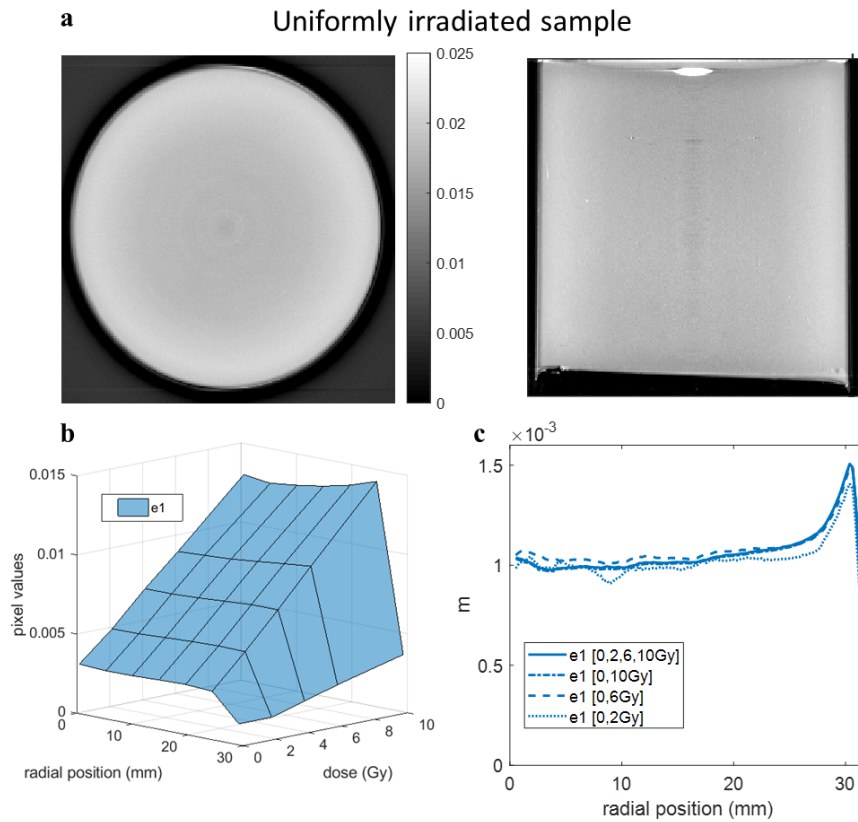
Figure 6.3: (a) 2D transverse and longitudinal slices of the reconstructed optical-CT image for sample e1 uniformly irradiated with accumulated doses of 10Gy. (b) Relationship between optical-CT pixel value and dose along the sample radial distance. (c) Gradient (m) versus radial position for sample e1, obtained with different dose levels. Correction image used to correct the non-uniformly irradiated samples is the one obtained with all dose levels.

6.3.2.3   OAR generation and treatment plan

One sample was used as a dummy (sample e_dummy) to obtain a pre-treatment CT scan. Again, the dummy sample was used so only one CT scan was required to calculate a dose distribution to be delivered to different samples of PRESAGE®. The set-up, which is shown in the top panel of Figure 6.4, aims to mimic the pelvis of a patient, with the PRESAGE® sample acting as both partially the rectum and the prostate OAR. The CT scan was exported to Raystation, where the OAR were created based on a model based segmentation (MBS) [51]. The "Pelvis Male" model which includes the prostate, the rectum, the bladder and

the right and left femur bones, was used. The OARs were positioned so that the
PRESAGE® cylindrical hole would coincide with the centre of the rectum OAR
volume. The prostate shape was drawn to be around the rectum (see Figure 6.4),
to create a more challenging plan optimization. Clinically this also mimics cases
where the seminal vesicles (which are included within the PTV margins used
for prostate RT at the RMH) are around the rectum. In addition, when air is
present in the rectum, this shape is also expected to produce more substantial
dosimetric changes. The rectum, prostate, bladder and the two femur bones
volumes were defined as CTV volumes. The final pre-treatment CT with the
associated structures were exported to Monaco TPS, where the dose distribution
was optimized and calculated (upper panel of Figure 6.4).

The PRISM study (prostate radiotherapy integrated with simultaneous MRI)
protocol, implemented clinically to treat patients at the MR-linac, was followed for
the phantom/PRESAGE® experiments (same number of beams, constraints and
cost functions used for dose optimization). The treatments consist in delivering
60Gy in 20 fractions using IMRT with seven beams to target the PTV (CTV:
0.3cm posterior expansion and 0.5cm elsewhere). More information about this
study can be found at https://clinicaltrials.gov/ct2/show/NCT03658525. The
dose delivered was scaled for the phantom/PRESAGE® experiments (see the
following subsections).

6.3.2.4   TPS exercise - the effect of an air cavity

If air cavities are not accounted for, hot and cold dose regions are expected at the
interfaces of these cavities. This effect can change in magnitude and extension
depending on the treatment plan, size and location of the cavity. As differences
are only expected at the edges of a dosimeter, before selecting the size of the hole
to drill on a sample of PRESAGE®, three different cavity sizes were simulated
to make sure the changes in the dose distribution, caused as a consequence of the
ERE, were large enough to be measured. To study this, an initial plan (reference
plan_uniform) was optimized and calculated in Monaco, using the pre-treatment

CT scan of the dummy sample of PRESAGE®, simulating a situation with no cavity present, as shown in Figure 6.4. This reference plan was then used to re-calculate the dose distribution on a modified version of the CT scan, where the PRESAGE® sample density was overridden to ED=0.01, to simulate different cylindrical air cavities of 1.2cm, 2.4cm (the original size of the PRESAGE® hole on the CT scan), and for 3.5cm. The larger cavity created a more extensive, and higher, difference in dose, and for this reason, was selected for the experiments with PRESAGE®. The plans were scaled to deliver 8Gy to cover at least 50% of the PTV as this produces an adequate dose gradient for PRESAGE® measurements.

6.3.2.5   Dose delivery - ATP workflow with and without an air cavity

Two samples of PRESAGE® were then physically modified to have the same length and diameter of sample e_dummy. For one sample (sample e_cavity) a hole of 3.5cm diameter was drilled while the other sample was not further modified (sample e_uniform). A schematic of this study is displayed in Figure 6.5, and it is separated in 3 steps.

In the first step, the treatment plan was optimized based on a homogeneous PRESAGE® (reference plan_uniform). The second step consisted of irradiating sample e_uniform and sample e_cavity. The phantom was placed at the MR-linac couch in as close position as possible as defined in the reference plan. Each sample was irradiated as per the ATP workflow by following the same methodology as described in subsection 6.3.1. The ATP workflow was used here to account to compensate for mispositioning the phantom as it is challenging to place the sample as per the reference plan. Since the PRESAGE® sample was surrounded by water in this experiment, it become visible by the lack of MR signal. Because the ATP workflow was used, two new plans were calculated, one for each sample. These re-calculated plans should be identical, as the phantom was not moved between irradiations, and should also be very similar to the original plan (reference plan_uniform). The third step consisted of re-calculating the dose on the CT scan without cavity and with a 3.5cm diameter cavity in order to compare the results
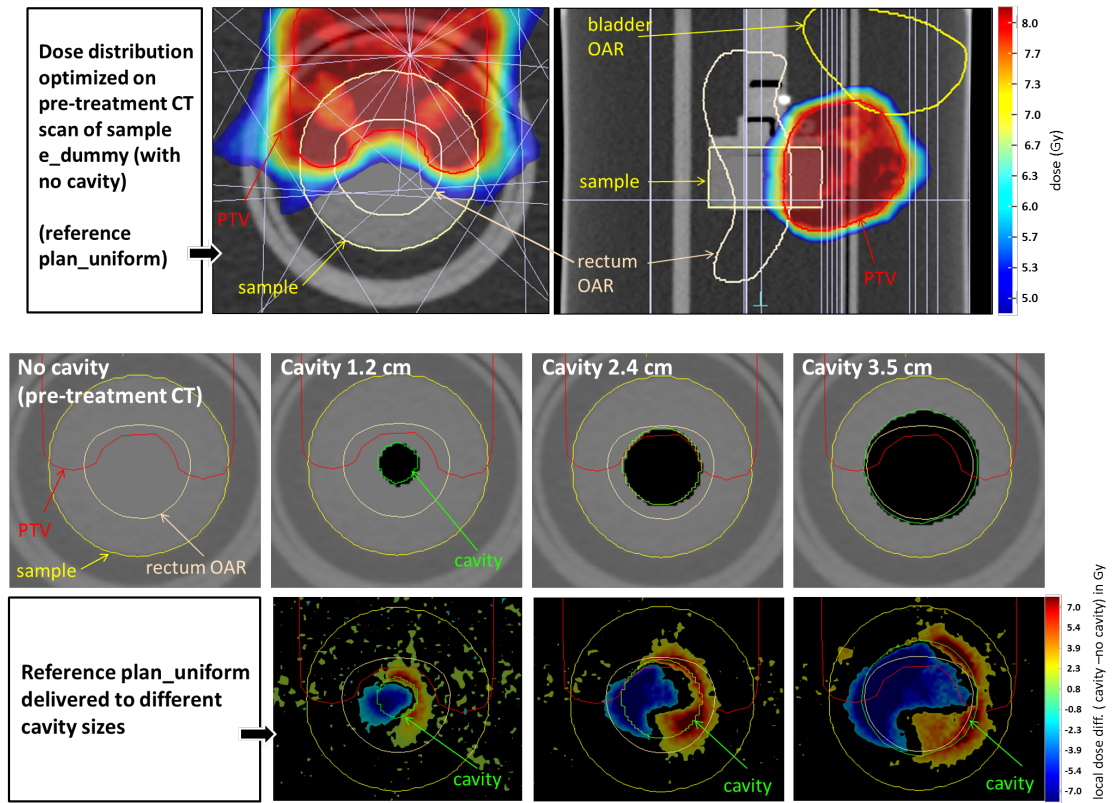
Figure 6.4: Optimized dose distribution calculated on the pre-treatment CT scan (no cavity) is shown on the top panel. On the bottom panel, the pre-treatment CT scan is again shown displaying a situation of a homogeneous PRESAGE® sample (no cavity) and with three different cavity sizes. The PTV and the rectum contours are shown for reference. The density on the CT scan was overridden based on the defined contours shown in green. The contour of the PRESAGE® sample is also shown (yellow). Local dose differences between the dose distribution obtained by delivering the reference plan_uniform to a homogeneous PRESAGE®, and to three different cavity sizes are displayed. A more extensive and higher difference in dose is visible for a 3.5cm diameter cavity.

with the measured data obtained with sample e_uniform and sample e_cavity, respectively. Again, all plans were scaled to deliver 8Gy to cover at least 50% of the PTV.

6.3.2.6 Dose delivery - ATS workflow validation

Sample e_uniformATS was irradiated at the MR-linac following the ATS workflow. This means that after registering the pre-treatment CT and the MRI of the phantom and, deformable propagating the ROIs from the CT to the MRI, the
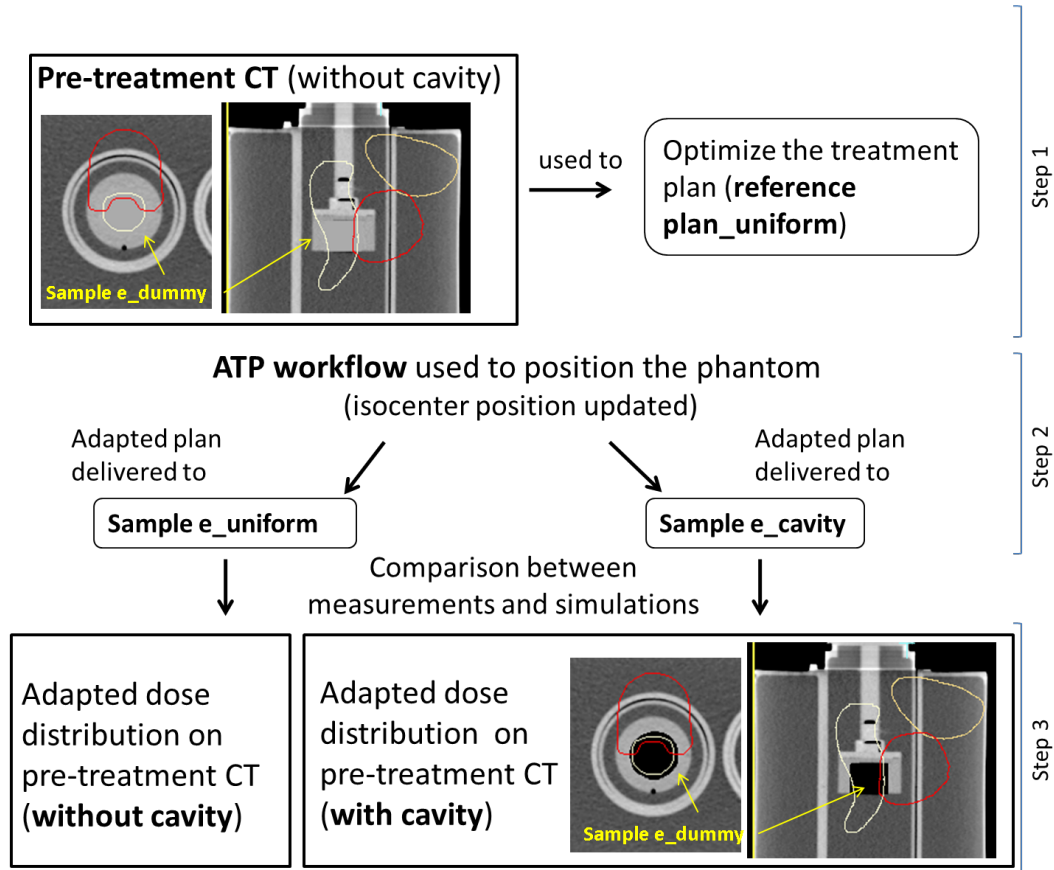
Figure 6.5: Schematics of the study performed to measure the effect of air cavities on dose distribution, not taken into consideration during plan optimization, using PRESAGE® samples and the QUASAR phantom to mimic a prostate treatment. ATP workflow was applied here to correct for errors in positioning the phantom at the MR-linac isocentre. Comparison between measurements and simulations was performed on Matlab® after normalizing the samples to a pre-defined region within the sample.

plan was re-optimized on the MR image. A schematic of this study can be found in Figure 6.6. Bulk densities were previously assigned in Monaco for the external contours ROIs to correspond to water density. I modified the shape and position of the PTV in order to simulate prostate volumetric changes since the pre-treatment CT scan. This alteration did not attempt to represent an exact clinical situation but rather to create a substantial difference on the dose distribution. The plan was also scaled to deliver 8Gy to cover at least 50% of the PTV.
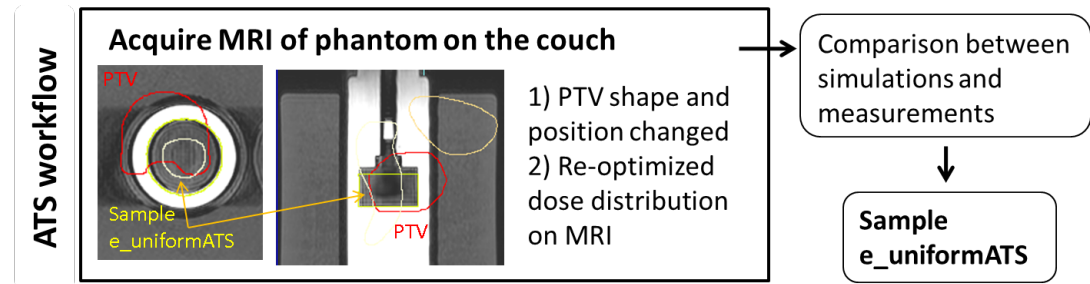
Figure 6.6: ATS workflow performed to irradiate the sample e_uniformATS. The MRI was acquired before irradiating the sample e_uniformATS, and then used to re-calculate the dose distribution based on the phantom position on the couch. The PTV shape and position was changed before re-optimizing the treatment to mimic daily patient organ motion. The PTV contour was enlarged and shifted in relation to the original dataset.

6.3.2.7 Comparison between PRESAGE® and Monaco TPS

Sample readout was performed for all samples as described in section 3.5 and in subsection 3.6.4. They were imaged before and 1h after irradiation using the telecentric optical-CT scanner to obtain reconstructed images with a voxel size $0.24mm$ x $0.24mm$ x $0.19mm^3$ for samples of 3.5cm and 0.30 x 0.30 x $0.20mm^3$ for the larger samples.

Simulations were performed in Monaco with $1mm^3$ resolution and 1% statistical uncertainty. Both Monaco calculated dose distribution and PRESAGE® reconstructed images were again rescaled to a 0.5 x 0.5 x $05cm^3$ voxel size and registered based on the CT scan image information. Relative dose agreement between the two was investigated based on dose profiles and by applying the 3D gamma criteria.

For the experiments performed with samples a_ATP1, a_ATP2 and a_ATP3, Monaco data was normalized to the maximum dose value and PRESAGE® samples rescaled to match the Monaco sagittal central values of the central slice (10mm flat region of the profile). For sample e_uniform, e_cavity and e_uniformATS, the Monaco calculated dose was normalized to the high dose region along the samples' length, and again PRESAGE® was rescaled to the same value. All samples were previously corrected with their correspondent *Formulation* correction image (sample a11MRL with samples from *Formulation a*, and sample e1 with

Table 6.1: 3D Gamma passing rates (%) applied for a 2%,2mm criteria and 10% dose threshold. All samples were corrected using a sample from *Formulation a*

Irradiation	2%,2mm
a_ATP1	98.5
a_ATP2	99.7
a_ATP3	98.4

samples from *Formulation e*).

Because the sample hangs vertically in the optical CT scanner, before scanning the sample e_cavity, the cylindrical hole had to be filled with matching liquid and sealed with tape (Gorilla Crystal Clear Duct Tape, US). However, it was not possible to fill the cavity completely. This means that an air-bubble was always present in the FOV of the projection images. In order to compare measurements and simulations, the volume correspondent to the cavity in PRESAGE® was overridden in Matlab®, to zero in both datasets.

6.4   Results

6.4.1   ATP workflow validation

In Figure 6.7 normalized PRESAGE® reconstructed and Monaco simulated central axial and sagittal 2D images are shown for sample a_ATP1, a_ATP2 and a_ATP3. Profiles taken in the axial and sagittal directions are also shown for comparison. The 3D gamma passing rates for the comparison are shown in Table 6.1.

6.4.2   Prostate treatment - ATP dose delivery with and without an air cavity and ATS workflow validation

6.4.2.1   Dose delivery - ATP workflow with and without an air cavity

PRESAGE® measurements and Monaco calculated averaged central 2D sagittal and axial dose distributions are shown in Figure 6.8. Axial 3D gamma maps
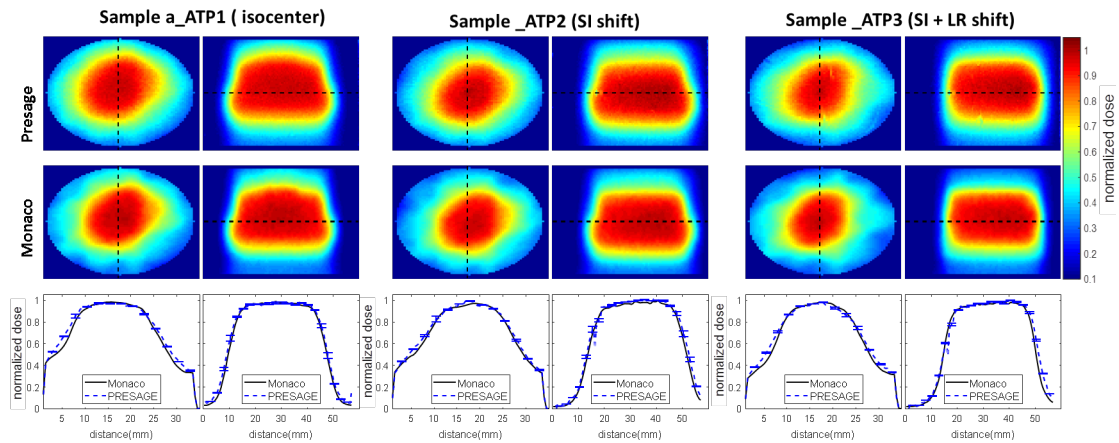
Figure 6.7: Axial and sagittal slices showing normalized 2D colour-coded measured (PRESAGE®) and calculated (Monaco) dose distributions and profiles taken from the regions represented by the black dashed lines. PRESAGE® samples higher sensitivity to radiation at the axial edges was corrected here using a sample from *Formulation a*. Profiles were averaged over ±0.75mm and error bars represent one standard deviation of the variation within that area. Monaco dose calculations are within 1% uncertainty.

averaged in the same sagittal regions are shown for comparison. Given the obtained dose distributions and the passing rate of the gamma evaluation (Table 6.2), there is a good agreement between simulations and measurements. In Figure 6.8, profiles taken in regions where the dose changes due to the air cavity are evident (diagonal 1 and 2) are shown for both Monaco and PRESAGE® normalized dose distributions. Small disagreements are visible on the diagonal 1 profile, but very good agreement is displayed on the diagonal 2 profile. Differences occur mainly at the samples' edges. For sample e_cavity an air bubble is present inside the cavity, which creates artefacts axially to the sample. In Figure 6.9, 2D dose difference between the accumulated dose with and without the presence of a cavity is shown for both PRESAGE® (sample e_cavity and e_uniform) and Monaco. The increase in dose due to the ERE effect is clearly visible in the figure.

6.4.2.2   Dose delivery - ATS workflow validation

For the ATS verification, 2D axial dose distributions obtained over 1cm along the sample's length, and diagonal profiles are shown comparing both simulations and measurements (Figure 6.10). Excellent agreement was found between the
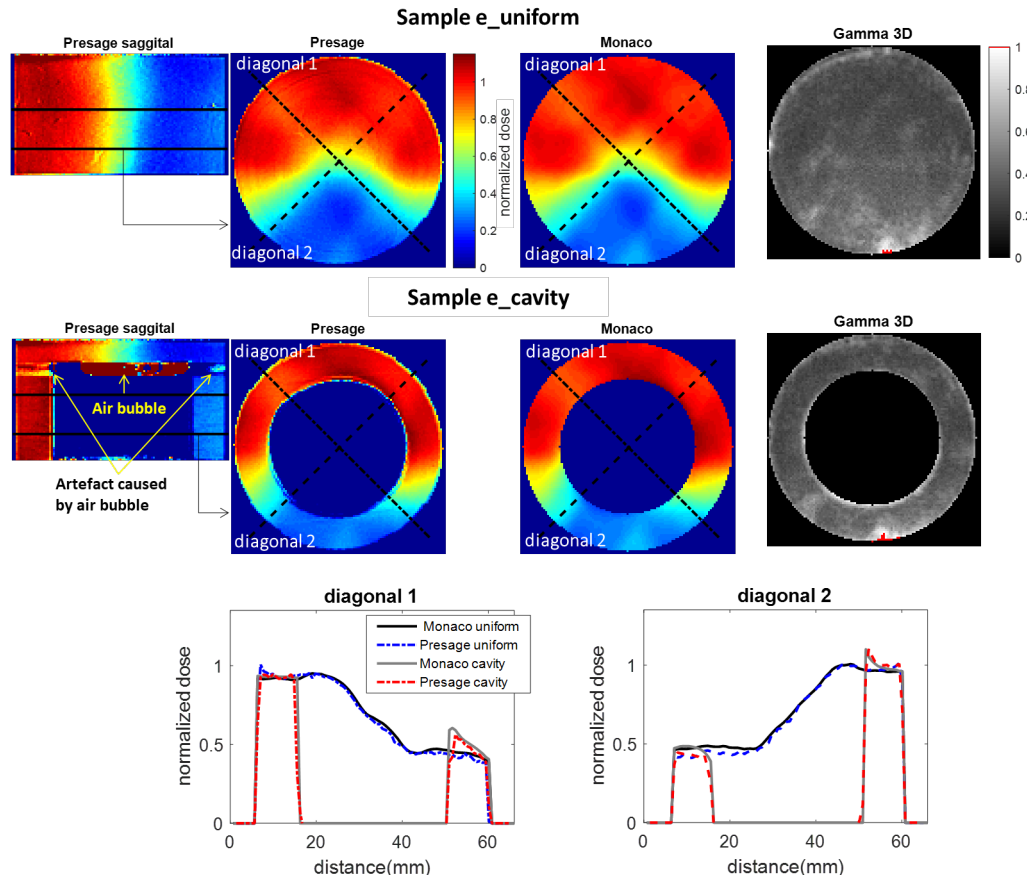
Figure 6.8: Samples e_uniform and e_cavity normalized axial 2D dose distributions averaged over 1cm, as shown on the sagittal view. Respective calculated dose distributions in Monaco are shown. Averaged 3D profiles obtained over the same 1cm are also shown. Diagonal profiles taken along both measurements and simulations for irradiation with and without an air cavity are superimposed for comparison.
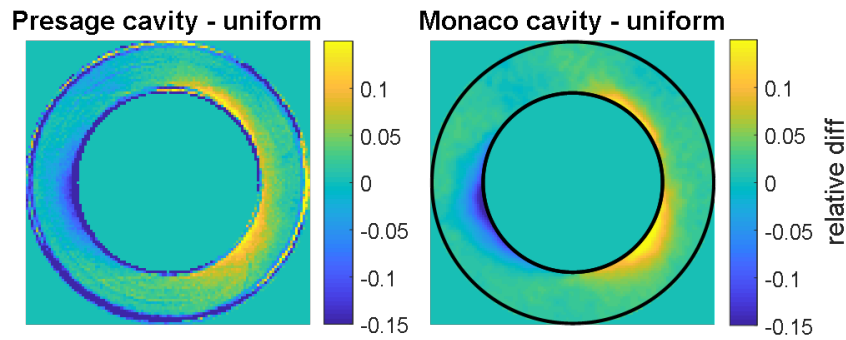
Figure 6.9: 2D normalized relative dose difference between PRESAGE® sample e_cavity and e_uniform. The equivalent Monaco simulated data is shown for comparison. Dose distributions were averaged over the same 1cm region within the sample displayed in Figure 6.8.
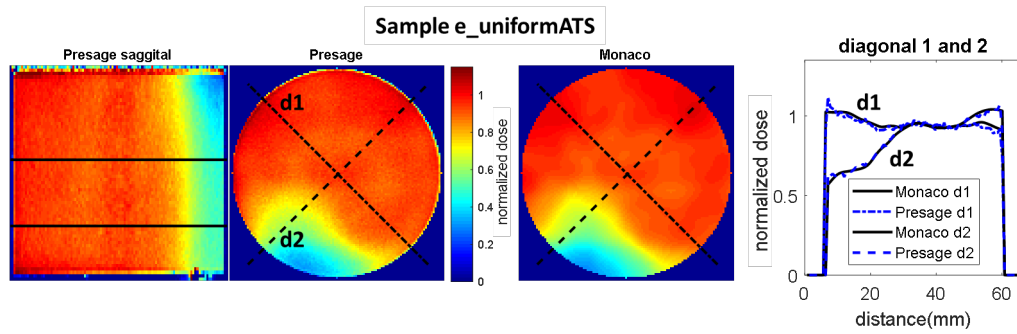
Figure 6.10: Sample e_uniformATS normalized axial 2D dose distributions averaged over 1cm along the sample's length. The region is as represented on the sagittal view of the PRESAGE® dose distribution. The equivalent axial 2D calculated dose distributions are shown. Diagonal profiles taken along both measurements and simulations are shown on the right panel.

Table 6.2: 3D Gamma passing rates (%) applied using different criteria and a 10% dose threshold. All samples were corrected using sample e1 as edges effect extended to more than 6mm. For sample e_cavity the gamma criteria was calculated by excluding the slices where an air bubble in the matching liquid was present within the sample cavity.

Irradiation	3%,2mm	2%,2mm
e_uniform	99.6	99.4
e_cavity	99.2	98.6
e_uniformATS	100	100

normalized dose distributions. The 3D gamma map is not shown considering the excellent agreement between simulated and measured data (Table 6.2).

6.5   Discussion

In this chapter, the MR-linac online adaption workflows were tested using PRESAGE® dosimeters together with a phantom. The set-up was used as a simplified version of a lung phantom and a pelvic phantom. The PRESAGE® samples' invisibility in the MR images was not an issue for the workflow validation at the MR-linac. For instance, the samples were visible when surrounded by water. When in air, their position within the phantom could still be identified with the use of fiducials. A good agreement between PRESAGE® measurements and Monaco simulations was obtained for all E2E adaptive treatment workflows tested

at the MR-linac, always with a gamma passing rate higher than 98% for a 2%, 2mm 3D gamma criteria.

In the first study, I showed that phantom displacements are accurately compensated by the MLCs when using the ATP workflow. The 3D-gamma passing rates for all three experiments were very high and, differences between the three experiments were likely due to the samples' uncertainty.

In the second study, the effect of different size cavities was investigated to determine the cavity size that would result in a significant and measurable ERE. The simulated cavity sizes of 1.2cm and 2.4cm were outside the PTV volume while the larger 3.5cm was within that volume. These results are in agreement with previous studies that have shown that both the size and the position of a cavity affect the magnitude of the ERE [19, 200]. The authors showed an increase/reduction in dose (compared to a homogeneous region) when an air cavity was within the target area. Furthermore, changes in dose due to the ERE has been shown to be more significant in larger cavity sizes [200].

The sample with a cavity (sample e_cavity) has a lower agreement with simulation, when compared to the uniform sample (sample e_uniform) (Figure 6.8 and Table 6.2). Regions where the gamma fails are at the samples' borders. Samples with cavities have edges not only externally but also internally, and they also have overall less material. This will affects the ratio between the edges and the uniform region of a sample, and consequently, the percentage of points within the gamma criteria.

The artefacts created by an air bubble inside the cavity of the sample e_cavity were not problematic since the information provided by the sample was sufficient to validate the adaptive tools of the MR-linac. However, for future measurements, this can be compensated by drilling an additional hole (maximum 5mm) from the middle of the sample through the cap so that the air bubble could be within the cap region and consequently out of the FOV. I tested this alternative, and it worked. However, the additional hole must be filled with water during irradiation, to not affect dose distribution. Another option can be to include the extra hole

in the simulations by acquiring a CT scan of the modified sample inside the QUASAR phantom.

Subtracting the dose distribution measured with PRESAGE® without cavity from the sample with a cavity reveals the expected hot and cold region at the cavity internal edges (Figure 6.9). These subtracted dose distributions compare well visually with simulations. However, when subtracting the images of sample e_uniform from the sample e_cavity, additional edge artefacts were generated. Samples surface imperfections or the existence of dust in the liquid can contribute to different values at the edges that, when subtracted, became more evident. Also, if both samples were not scanned in the exact same position, as a result of for example, sample tilt during scanning, the edges of the samples would not be completely overlaid creating an additional loss of information at the borders of the samples. Nevertheless, this does not compromise the validly of the results measured with PRESAGE® samples, as the ERE was clearly measured at the cavity interfaces.

6.6 Conclusion

PRESAGE® measured data confirmed the dosimetric accuracy of Monaco TPS and the precise treatment delivery of MR-linac. Both ATP and ATS MR-linac online workflows were validated using PRESAGE® samples and a phantom simulating a lung and a prostate IMRT treatment. The expected increase in the dose distribution due to an air cavity, not accounted for during plan optimization was accurately measured using a PRESAGE® sample with an air cavity. The results shown in this chapter give the confidence to create plans in the presence of air cavities.

Chapter 7

Verification of dynamic MLC-tracked RT

Dynamic MLC-tracked RT aims to compensate for intra-fractional tumour motion by preserving the target dose and consequently reducing the dose received by the nearby healthy tissues. In this chapter, I used samples of PRESAGE® and a motion phantom to verify the dose delivered by MLC-tracked RT using both a conventional (research) linac and the MR-linac at the ICR/RMH. Two possible treatment sites were studies by creating plans representative of dose distributions for RT in the lung and prostate. Some of the results described in this chapter can be found in the conference proceeding by Costa et al., 2019a [41].

7.1   Introduction

MRgRT systems are powerful tools for treatment adaptation based on daily patient anatomy. A method of compensating intra-fraction tumour motion consists of moving the MLC leaves dynamically so that the beam aperture follows the target position. This method reduces unnecessary irradiation received by healthy tissues as it allows for a reduction of the PTV margins [27]. Tumour tracking has been employed clinically for the treatment of prostate [106], lungs [21, 54] and liver [54] cancer using SBRT. Tracking can also be applied using a robotic linac control [109] and/or couch motion [63, 140].

Dynamic MLC leaves have been employed for tracking purposes using kV and MV imaging [17, 29], using a combination of kV and optical systems [34], or through the identification of electromagnetic transponders [105, 113, 190]. These methods require surrogates to detect the actual position of the target (body surface imaging, spirometers, breathing belts), or by implanting fiducials within the tumour.

With MRgRT systems, the MLC leaves will likely be able to not only follow the motion of the target but also change their shapes based on non-rigid anatomical changes of both the target and OAR using MR images. Sagittal 2D cine-MRI images have been previously used to identify and follow a defined target in the lungs of healthy volunteers [150]. The physical possibility of tracking using feedback from an online MRI was first demonstrated by Crijns et al., 2012 [43]. A recent paper has shown that MLC-tracking at the Elekta MR-linac is technically possible [70], but the authors did not provide a dosimetric verification.

7.1.1   Aim

In this chapter, I first want to demonstrate that PRESAGE® samples can correctly reproduce the dose distribution simulated by in-house MLC-tracking software (DynaTrack). The software moves the MLC leaves dynamically based on a given target position [15, 68, 101], and it was previously validated with a

research Elekta linac at ICR/RMH, using an array of detectors (Delta4) mounted onto a 4D motion platform [38].

The initial study was performed in a conventional linac before the tracking software was available at the MR-linac. This allow identifying and eliminating any issue without requiring the use of an MR-linac. After verifying this methodology using PRESAGE® I adopted it to validate real-time tracked MLC RT treatments at the Elekta MR-linac by the time it become available. The software had to be updated to be run at the MR-linac and requires validation.

7.2 Material and Methods

7.2.1 In-house dynamic MLC-tracking software

The in-house dynamic MLC-tracking software DynaTrack was initially developed for a Siemens 160MLC on an Artiste linac [113, 140, 194] and later implemented on an Elekta Synergy research linac at the ICR/RMH [68]. The system requires as input a treatment plan (MUs, gantry angles, MLC shapes) generated for a static case and a continuous stream of target positions. Target information can be provided using imaging from different modalities, such as kV and MV planar imaging [68], the Varian Calypso system [113, 140] and more recently, from MR images. An alternative source for the target position identification is through data streaming of target positions reported directly from the movement device.

7.2.2 System latency

Before using DynaTrack to take control of a linac, it is essential to measure the system latency. The system latency in this situation is defined as the difference between the time of the new target position and the time the MLC leaves take to reach that position [68]. There are three different contributing terms for that latency: (i) the motion device latency (the QUASAR phantom in this study), which is the time that it takes for the device to reach an induced position; (ii) the

age of the target position when used by the MLC controller to request an MLC shape. On average, this consists of half of the update rate of a phantom device, or image, used to report the target position; (iii) the average MLC displacement latency, which is the time the MLC leaves take to meet a requested MLC shape.

After the determination of the system latency, a motion predictor can be used to compensate for that delay [194]. The MLC latency was determined based on a set of experiments which followed the methodology described by Fast et al., 2014 [68]. We used a 2cm diameter copper sphere attached to the same holder used for PRESAGE® (Figure 7.3c). A treatment plan with one beam at gantry angle of 0°, and an 8cm diameter circular field was used to irradiate the sphere. EPID images were obtained while a sinusoidal motion was applied to the phantom in the SI direction. Sinusoidal curves with different amplitudes of 5, 10 and 20mmm and breathing periods of 4s and 5s were used. The motion of both the sphere and the MLC leaves was determined based on EPID images of 0.8mm x 0.8mm pixel resolution and with 30Hz update rate, acquired during 5 to 7 periods. The position of both the sphere and the MLC shapes, for all the acquired images ,were identified by a threshold segmentation algorithm. A sinusoidal curve was then fitted for each set of data-points obtained. The time shift between the two sinusoidal curves (obtained from the sphere and MLC shapes) was calculated for the experimentally obtained combination of sinusoidal amplitudes and periods. The average of the determined time shifts gives the system latency. The (iii) average MLC leaves displacement latency, which was found to be 35ms, was then determined by subtracting (ii) the age of the target position when used by the MLC (33ms/2), and the (i) motion device latency (1ms in our experiments with the QUASAR phantom) from the calculated system latency.

7.2.3 Offline dose reconstruction (ODR) tool

To calculate the delivered dose distribution of an MLC-tracked RT, I used an offline dose reconstruction (ODR) tool [143] in the Monaco TPS. The tool allows the dose distribution to be calculated under the same conditions as an actual RT
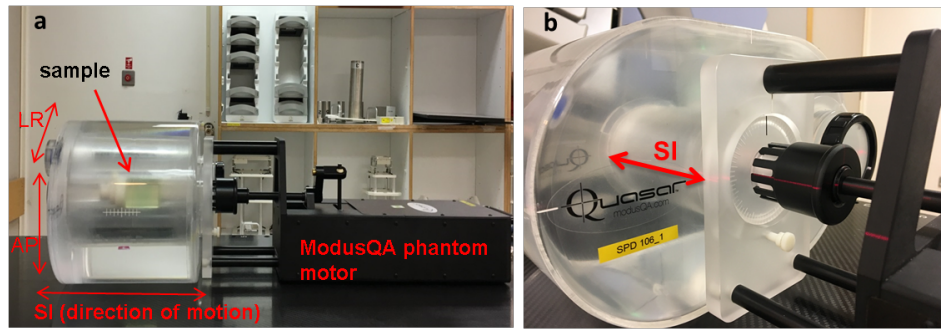
Figure 7.1: (a) Experimental arrangement showing an irradiated sample of PRESAGE® placed, with the in-house holder, inside the central cylindrical insert of the QUASAR motion phantom. A motion was applied in the central cylinder of the phantom in the SI direction. The experimental set-up here is at the Elekta research linac. The same set-up was used for the experiments at the MR-linac. (b) For clarity, the same phantom is shown with the central cylinder attached to the motor.

delivery. It requires as input the logfiles generated by DynaTrack during the dose delivery, which contains the target positions recorded every 40ms, the shapes of the MLC leaves and jaws, as well as the delivered MUs and gantry angles. In order to calculate the dose distribution, the tool associates an MLC shape to each recorded target position. Target positions within 1mm are grouped (only one target position is used). The same is performed for an MLC leaf that shifts within 0.5mm. In addition to the obtained logfiles, the ODR requires the original CT scan, the original treatment plan and the original dose map to reconstruct the dose distribution under similar conditions to those during the RT delivery.

7.2.4 MLC-tracked RT at the Elekta research linac

Before MLC-tracking was available at the Elekta MR-linac, a proof of concept experiment was performed at the RMH/ICR research linac, using small PRESAGE® samples (samples of 3.5cm diameter x 5cm length from *Formulation a*) and the QUASAR motion phantom (Figure 7.1). A diagram describing the experiments workflow is shown in Figure 7.2.

The phantom was positioned on the couch of the linac with the help of lasers. This way, the centre of the sample, which was placed inside the central cylinder of the QUASAR phantom, was placed at the linac isocentre. As can be seen in

a

Phantom positioning	Target position input	Plan delivery

Elekta Synergy
• lasers
Elekta MR-linac
• EPID + dummy sample

→

Elekta Synergy
• phantom motor
Elekta MR-linac
• 2D-cine MRI

→

DynaTrack

updated MLC shapes
↓
linac

b

PRESAGE® irradiation conditions

(1) Static
(2) Motion (w/o tracking)
(3) Tracking

- - optical-CT - → **Measured dose distribution**

comparison
(3D gamma criteria)
↕

DynaTrack
↓

log-files created during irradiation

• MLC shapes
• MUs
• target position

→

Simulated dose distribution

Research Monaco - offline dose
reconstruction (ODR)
(1) Static
(2) Motion (w/o tracking)
(3) Tracking

Figure 7.2: Diagram describing the study workflow. (a) The different steps from the PRESAGE® /QUASAR phantom positioning on the couch to the delivery of the RT using DynaTrack software. At the research linac, the phantom position recorded from the phantom control system were used as input for DynaTrack, while at the MR-linac target positions were identified using 2D-cine images. (b) Logfiles with the MLC shapes and the target positions were used to re-calculate the dose using the ODR in the Monaco TPS for the three delivery conditions. PRESAGE® samples measured dose distributions were compared with the TPS dose distributions after normalization.

Figure 7.1, the phantom central cylinder is attached to the motor which was used to move the sample in the SI direction. Rotation can also be employed, but it was not used in this study. A plan with four equally spaced 6MV beams of field sizes of 3 x 1.5cm^2 was used to irradiate the samples to a maximum dose of 9.7Gy. This is the same plan that I had previously used in chapter 5 (see Figure 5.2d). During dose delivery, the linac was controlled by DynaTrack to move the MLC leaves based on the positions of the moving target, which were reported by the motion phantom (Figure 7.2a). The subsequent steps of the experiments are as shown in Figure 7.2b.

Different samples of PRESAGE® were irradiated to test three different irradiation scenarios: (1) static: static sample, without tracking (2) motion: moving
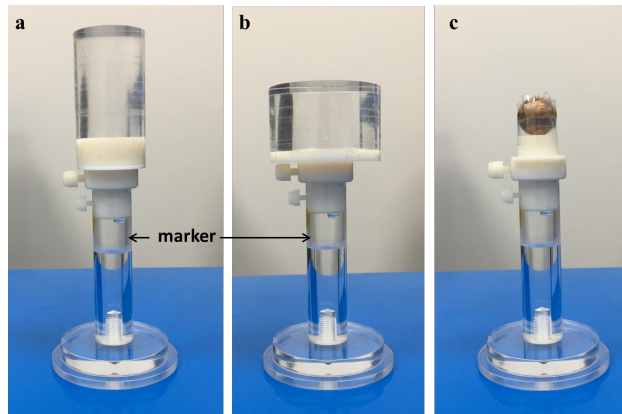
Figure 7.3: The versatility of the PRESAGE® sample holder to be placed in the QUASAR cylindrical insert. The sample holder was modified to have a cylindrical container of 2cm diameter and 2cm length. For these experiments, the container was filled with a liquid that provides good contrast for MR images (marker). The holder can be used to attach perspex cylinders or PRESAGE® samples with different shapes and sizes. (a) 3.5cm diameter; (b) 5.45cm diameter; (c) 2cm diameter copper sphere. This sphere was used for the determination of the MRI-linac latency.

sample, without tracking and (3) tracking: moving sample, with tracking. A sinusoidal curve of 4s period and 7.5mm amplitude was used to move the sample in the SI direction for the scenarios (2) motion and (3) tracking. For each irradiation scenario, logfiles containing the recorded MUs, gantry positions and MLC shapes were stored every 40ms. The phantom positions were obtained at a rate of 25Hz. The logfiles, together with the original CT scan, plan, and dose distribution allowed dose calculation using the ODR tool, for a direct comparison with the PRESAGE® measured dose distributions, after both had been normalized. Normalization was performed as in the previous chapter (subsubsection 6.3.2.7).

7.2.5 MLC-tracked RT at the Elekta MR-linac

The software Dynatrack was modified in-house to support the Elekta MR-linac special research control software and firmware.

7.2.5.1 Phantom/PRESAGE® positioning at the MR-linac

In order to position the phantom at the MR-linac, I used a perspex cylinder with the same dimensions as the PRESAGE® samples to be irradiated in this study

(Figure 7.3a and b). As explained in the previous chapter, to place the samples of perspex in the same position in relation to the MR-linac isocentre as planed in the TPS, EPID images are acquired with the gantry at 0° and at 90°. The central pixel value of these images corresponds to the MR-linac isocentre.

7.2.5.2 Target position identification using MR image

The PRESAGE® /QUASAR phantom set-up described previously in subsection 7.2.4 was applied here. Considering that the purpose of using an MR-linac is to be able to identify the target position directly from a real-time MRI, an MRI-visible object/marker was essential.

The sample holder, which was made of perspex, was modified at the ICR workshop to contain a cavity that could be filled with liquid (see Figure 7.3). The container was filled with a liquid which provides good contrast for typical MR images sequence (1000ml. demi + 770mg. $CuSO_4.5H_20$ + 1ml. arquad (1% solution) + 0.15ml. H_20SO_4-0.1N solution). This cylindrical container with MRI-liquid was used as a marker/surrogate for the identification of the PRESAGE® samples' position. This step is fundamental since PRESAGE® samples and the perspex material of the holder, are not visible on an MR image.

The position of the marker, in relation to the isocentre, was identified with EPID images and by knowing its distance to the perspex sample. After positioning the phantom, a previously developed in-house MRI tool was used to visualize the marker. The in-house MRI tool allows the user to define the location of a 2D-cine plane and select the desired scan protocol [69] (Figure 7.4a). Coronal 2D-cine images were acquired with a coherent fast field echo (FFE) sequence (latency of 200ms and a 3Hz update rate) to identify the position of the marker using a template matching algorithm [183]. This information was utilized by DynaTrack to move the MLC leaves based on the marker reported locations. The template matching algorithm was validated by comparing the reported positions by the MR-tool and the QUASAR phantom.

For the experiments at the MR-linac, I simulated two different plans in Monaco

using the previously acquired CT scans that were used in the studies described in chapter 6.

7.2.5.3 Lung treatment plan delivery

The IMRT plan dose delivered to PRESAGE® samples for the validation of the ATP workflow described in subsection 6.3.1 was used for these experiments (plan_lung consisted of 5 beams to target the centre of a 3.5cm diameter x 5cm length sample). The plan_lung dose was delivered to three samples of PRESAGE®. A new batch of PRESAGE® samples manufacturer with *Formulation a* was ordered for these experiments. As performed in the previous section, each sample was irradiated in three different conditions ((1) static, (2) motion and (3) tracking) as per the workflow described in Figure 7.2. For the scenarios where motion was applied, a sinusoidal curve with a period of 5s and 10mm amplitude was used to move the sample in the SI direction. The target positions during beam delivery were obtained from the 2D-cine images at an update rate of 3Hz and a 200ms latency. Considering the low MR images update rate and their long latency, the total system latency was 401.5ms ((i) 200ms + (ii) 0.5x333ms + (iii) 35ms). In order to improve the accuracy of the tracking, a linear regression predictor with a variable prediction time length was applied during beam delivery.

7.2.5.4 Prostate treatment plan delivery

In order to mimic a prostate plan, the CT scan and treatment plan used for the validation of the ATP workflow in the presence of air cavities was adapted here (plan_prostate) (see section subsubsection 6.3.2.4 for more information). A sagittal view of the calculated plan is shown in Figure 7.4b. The PTV was shifted so that its gradient region would coincide with the edge of the sample, aiming to increase the possibility of obtaining measurable changes when applying motion. The same workflow described in Figure 7.2 was applied here. The coronal 2D-cine images used for the identification of the target position are shown in Figure 7.4a. The tracer used for the (2) motion and (3) tracking scenarios is in Figure 7.4c. This
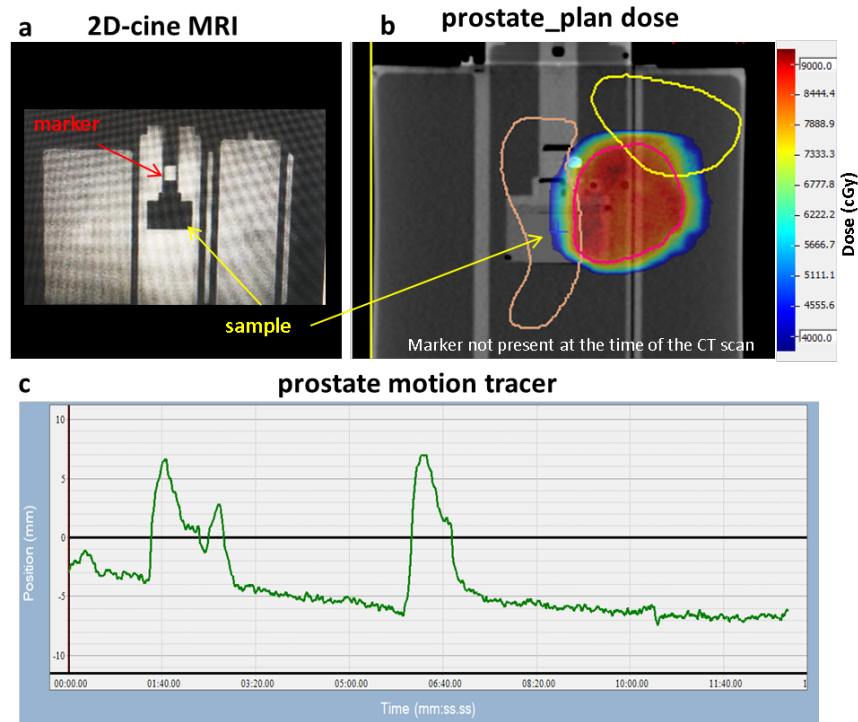
Figure 7.4: (a) Coronal 2D-cine MR image acquired to determine the target position to be used by DynaTrack. The software applies a template matching algorithm to determine the position of the marker. (b) Central sagittal slice view of the CT scan and dose distribution calculated with the prostate_plan. (c) Motion tracer used to move the sample inside the QUASAR phantom during the 8 minutes delivery of the plan_prostate dose distribution.

motion pattern was taken from real patient data [38]. For these experiments, no prediction was required or possible as the applied motion consisted of essentially small gradual, erratic shifts.

7.2.6   Comparison between PRESAGE® and Monaco

The 3D dose distributions obtained from both PRESAGE® samples and Monaco calculations were normalized (subsubsection 6.3.2.7) and compared using a local 3D gamma criteria of 3%, 2mm and a 10% threshold.

All samples' results were corrected using a sample image correction obtained at the closest time point to their irradiation. Samples irradiated at the research linac were optically scanned 1h after irradiation (see section 3.5 and subsection 3.6.4). The same was not possible for the dosimeters irradiated at the MR-linac, which
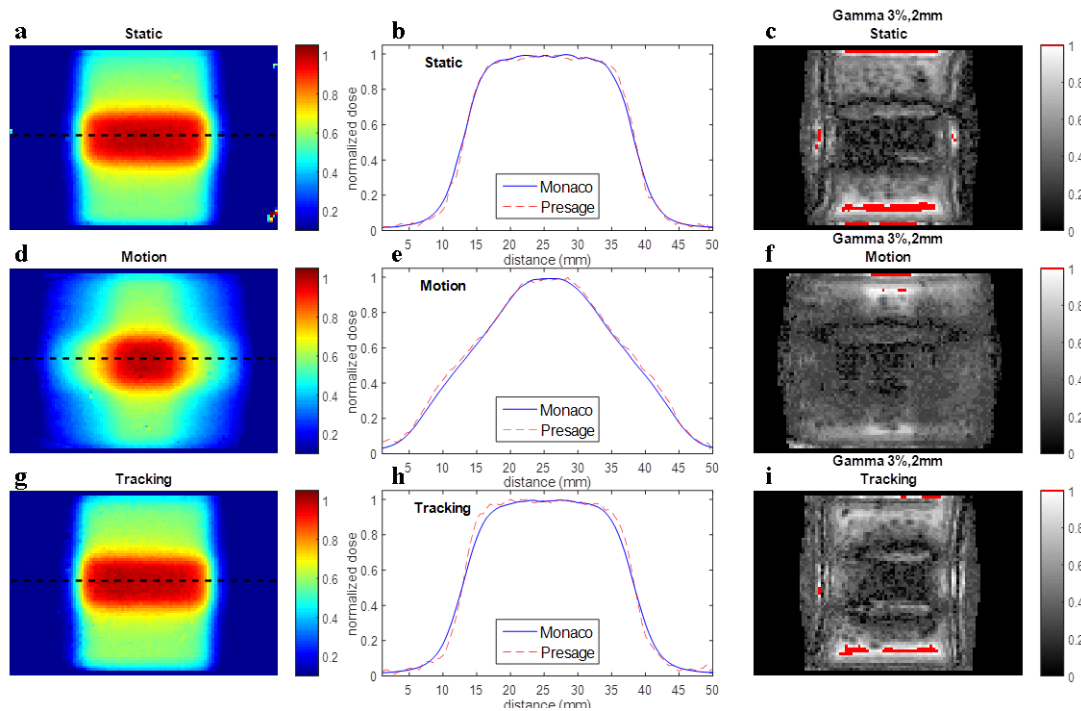
Figure 7.5: Normalized central sagittal slice showing PRESAGE® colour-coded dose distributions and the respective profiles along the SI direction for all three studied scenarios. Central sagittal slice of the 3D gamma map is shown, comparing measurements with simulations. Regions where the gamma criteria fail (gamma ≥ 1) are shown in red. These experiments were performed at the Elekta research linac.

were scanned 3h (plan_lung) and 2h (plan_prostate) after dose delivery. These were the only possible scanning times given that the experiments at the MR-linac were performed on the same day.

7.3 Results

7.3.1 MLC-tracked RT at the Elekta research linac

The agreement between measured and simulated reconstructed dose distributions is visible by taking a profile at the central sagittal slice (Figure 7.5b, e and h) and by applying the 3D gamma criteria (Figure 7.5c, f and i). The regions where the gamma criteria fail, in the central slice of the sample, are shown in red and occur mainly at the axial edges of the sample. Gamma passing rates for the comparison between measuremensts and simulations are shown in Table 7.1.
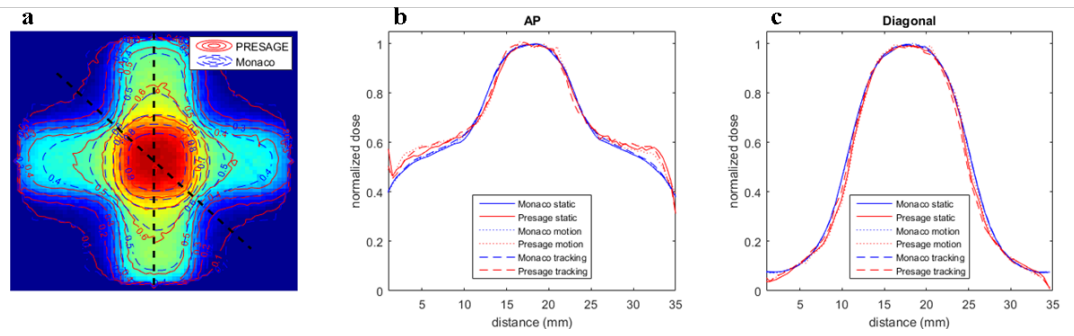
Figure 7.6: (a) Normalized central axial slice colour-coded dose distributions and isodose lines showing PRESAGE® under (1) static conditions. Simulated and measured profiles taken at the central axial slice at (b) AP and (c) diagonal directions are shown for (1) static, (2) motion and (3) tracking scenarios. Irradiations were performed at the Elekta research linac.

An axial normalized 2D dose distribution taken at the centre of the target and respective profiles obtained in two different directions are shown in Figure 7.6. The profiles are equivalent for the three samples as no motion was applied in the transverse direction of the samples.

PRESAGE® samples irradiated in static conditions were compared with samples irradiated in (2) motion and (3) tracking deliveries using the 3D gamma criteria. A central 2D sagittal slice of the gamma sample is shown in Figure 7.7 and the respective 3D gamma passing rates are in Table 7.2. This comparison allow assessing both the methodology and samples reproducibility and to be able to evaluate the advantages of tracking without requiring comparing the measured data with the calculated results with the TPS.

7.3.2   MLC-tracked RT at the Elekta MR-linac

The normalized dose distributions obtained with PRESAGE® samples by delivering the dose calculated for the lung and prostate plans are shown in Figure 7.8 and Figure 7.10 respectively. Profiles were taken along the samples' length to compare measurements and MC calculations. A sagittal section of the gamma 3D maps obtained from this comparison is also displayed, and the passing rates are in Table 7.1.

Figure 7.7: Central sagittal slice of the 3D gamma analysis is shown comparing the PRESAGE® sample in (1) static scenario with (3) tracking and (2) motion. Areas where the gamma criteria fail are in red. Irradiations were performed at the Elekta research linac.

Table 7.1: 3D Gamma passing rates in % (3%, 2mm and a 10% threshold) comparing simulation and measurements for all the experiments performed in this study. The last 5mm of the samples (prostate MR-linac) were disregarded for the calculations as they were affected by substantial edge artefacts, which is unrelated to the performance of the MLC-tracked dose delivery (see Figure 7.10c). If these regions were included, the passing rates would not allow a fair comparison with simulations for the sample irradiated in static conditions (static: 93.9%; motion: 97.1%; tracking: 97.4%).

Irradiation	lung research linac	lung MR-linac	prostate MR-linac
static	99.2	99.4	98.1
motion	99.7	98.9	97.1
tracking	99.3	98.1	98.1

A comparison between PRESAGE® samples irradiated in static conditions with the samples irradiated in motion and tracking are shown in Figure 7.9 and Figure 7.11 for the delivery of plan_lung and plan_prostate respectively. The 3D gamma passing rates for the comparisons can be found in Table 7.2.

7.4   Discussion

Previous studies which used 3D gel dosimeters to verify the dose distribution of MLC-tracked RT have demonstrated the benefits of acquiring 3D dose information [28, 187]. In this study, samples of PRESAGE® were irradiated for the first time for 3D dose verification of MLC-tracked RT at an Elekta linac and the MR-linac. In this study, I have shown that PRESAGE® 3D dosimeters can be used to
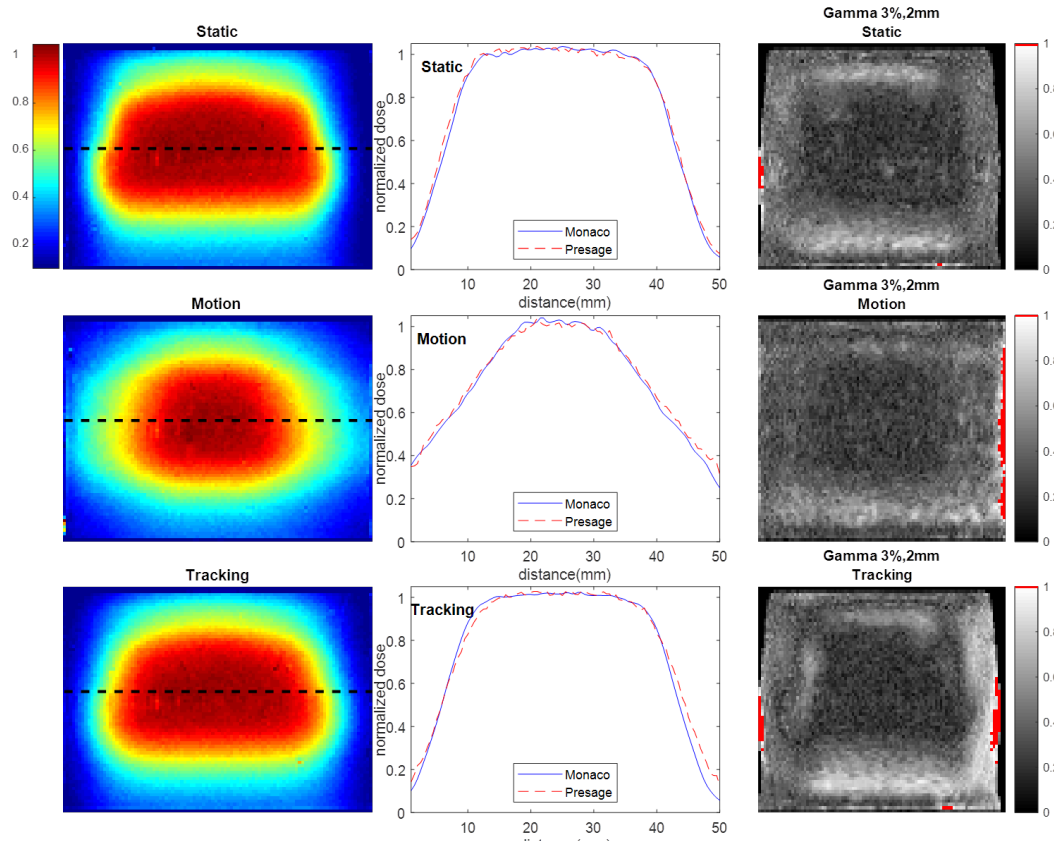
Figure 7.8: Normalized central sagittal slice (averaged over 1mm) showing PRESAGE® colour-coded dose distributions and the respective profile for the three irradiation scenarios of the plan_lung at the MR-linac. Central sagittal slice of 3D gamma analysis is shown comparing measurements with simulations. Areas where the gamma criteria fails (gamma $\geq$ 1) are shown in red. A correction image from *Formulation a*, but from a different batch, was used to correct the dose distributions obtained with PRESAGE® .
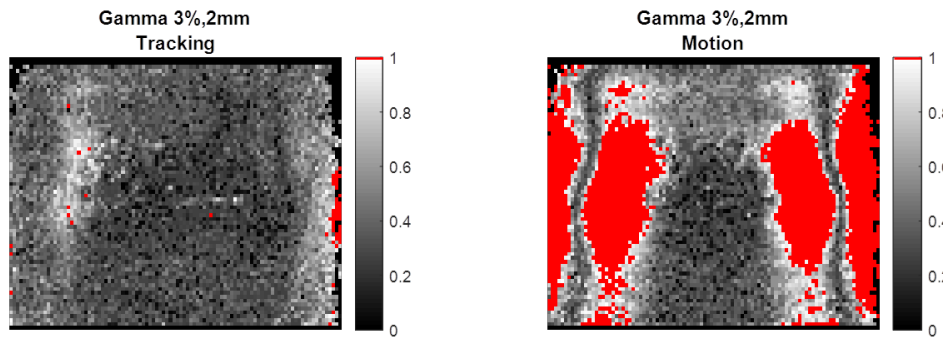
Figure 7.9: Central sagittal slice of the 3D gamma analysis is shown comparing the PRESAGE® sample in (1) static scenario with (3) tracking and (2) motion. Areas where the gamma criteria fails are in red. Irradiations were performed at the Elekta MR-linac linac with the plan_lung.
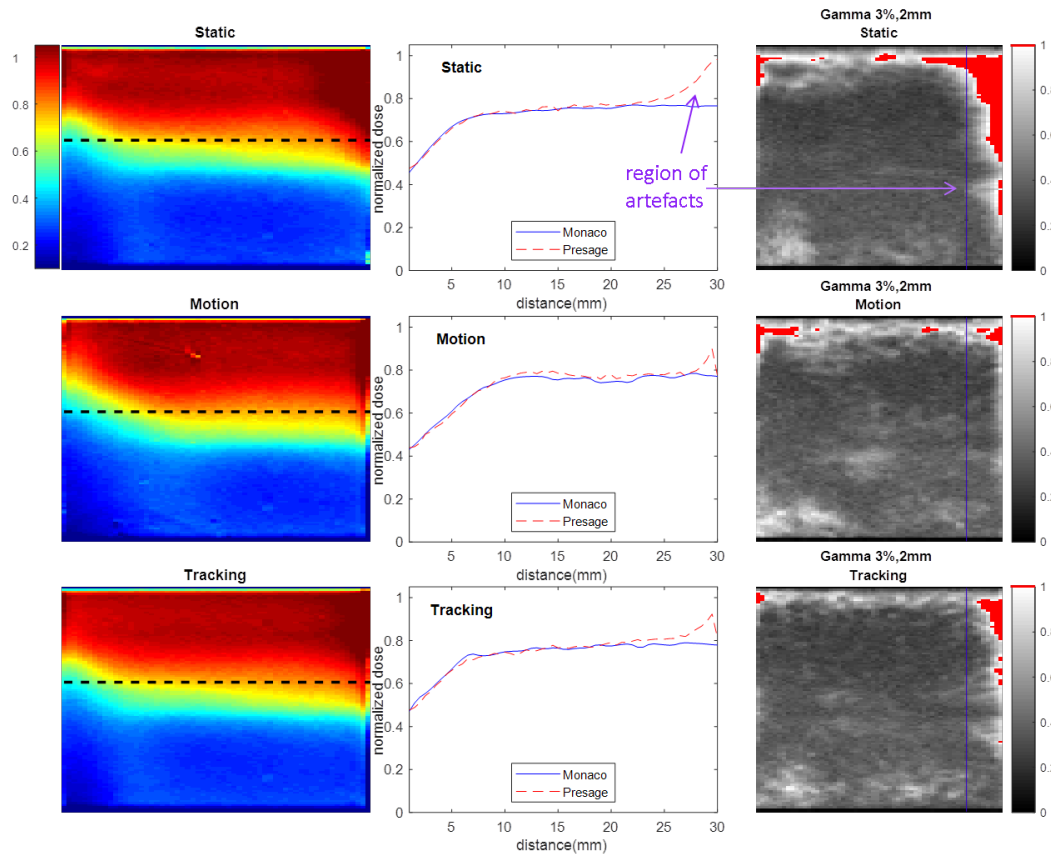
Figure 7.10: Normalized central (averaged over 1cm) sagittal slice showing PRESAGE® colour-coded dose distributions and a respective profile for the three irradiation scenarios of the plan_prostate at the MR-linac. Central sagittal slice of 3D gamma analysis is shown comparing measurements with simulations. Regions where the gamma criteria fail (gamma $\geq$ 1) are shown in red. Artefacts caused by an edge effect of approximately 5mm are visible for the sample irradiated in static conditions. These last 5mm of the sample were excluded for the calculation of the gamma criteria in Table 7.1 for a direct comparison with simulations. Samples used for this experiment were 11 months old, which explains the samples' extremities edge effect.
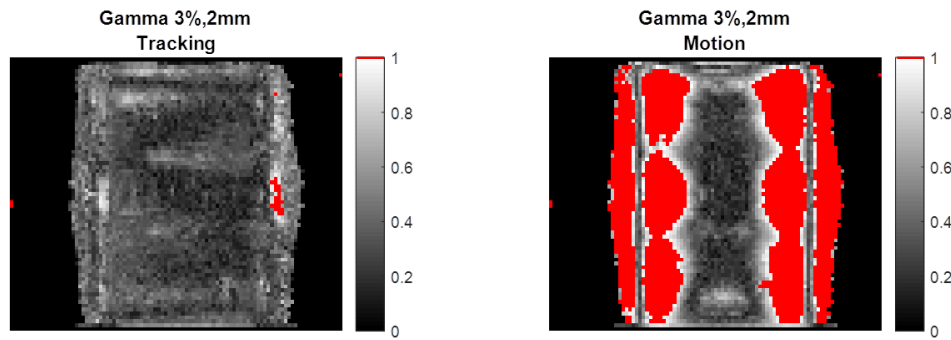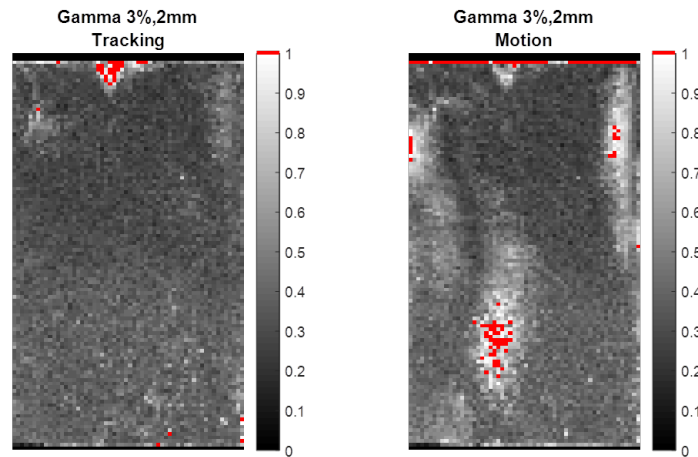
Figure 7.11: Central sagittal slice of the 3D gamma analysis is shown comparing the PRESAGE® sample in (1) static scenario with (3) tracking and (2) motion. Regions where the gamma criteria fail are in red. Irradiations were performed at the Elekta MR-linac linac with the plan_prostate. Regions of artefacts are likely due to an edge effect at the samples' boundaries. These samples were 11 months old by the time they were irradiated and, although their top and bottom edges were physically eliminated before these experiences, the results suggest the amount removed was not sufficient.

Table 7.2: 3D Gamma passing rate in % (3%, 2mm and a 10% threshold) comparing measured sample irradiated under (1) static conditions comparing with (2) motion and (3) tracking scenarios. *Considering the mild motion applied to the sample (prostate MR-linac), differences in the passing criteria between motion and tracking, when compared to a static scenario, can only be clearly distinguished if a tighter gamma criteria is used. For example for a 3%, 1mm criteria, there is a 74.0% and 91.9% passing rate for motion and tracking respectively, when compared to static.

Irradiation	lung research linac	lung MR-linac	prostate MR-linac
motion (static)	77.6	77.8	93.6*
tracking (static)	99.5	99.0	98.6*

verify the dose delivered in different irradiation scenarios of static irradiation and motion with and without applying tracking.

For the samples employed to mimic a lung RT treatment, a slightly narrower penumbra was visible for the simulated (3) tracking scenario profile (and (2) motion) in comparison with the respective measured profiles (Figure 7.5 and Figure 7.8). To reconstruct the dose delivered, the recorded MLC leaves positions were rounded to their nearest integer millimetre value. This explains the difference between the measurement and the simulated profiles, as particularly small fields were used in these experiments. This could explain the slightly lower passing

rate for the tracking experiments for both experiments mimicking a lung RT treatment. When the target undergoes a sinusoidal motion, the advantages of applying tracking are evident (Figure 7.5 and Figure 7.8). As expected, in the presence of movement without tracking, the 3D dose distributions are blurred compared to when MLC-tracking is applied. The same conclusions can be drawn from Figure 7.7 and Figure 7.9, where the gamma criteria was used to compare the sample irradiated in the (1) static scenario with the two other situations where PRESAGE® samples were irradiated while moving.

For the experiments which mimicked a prostate RT treatment, simulations and measurements agreed for most of the samples' volume except for an increase in the measured dose at the sagittal edge ($\sim$5mm) of the sample (Figure 7.10). The gamma passing rates for the comparison in Table 7.1 are between 97% and 98%. These are good result considering phantom positioning uncertainties (within 1mm SI and AP) as the ATP workflow could not be used.

The benefit of MLC-tracked RT during a prostate RT is not as clearly identified as for a tumour in the lungs. Nevertheless, small differences between measured samples in (2) motion and (3) tracking scenarios can be seen in the gamma maps (Figure 7.11). A less steep dose gradient is visible for the sample irradiated under (2) motion when compared with the other two (Figure 7.10) scenarios. This study portrayed a relatively simplistic situation where motion occurred only in SI direction. While prostate shifts might be more pronounced in the AP directions, the results presented here are relevant for TPS dose verification and as part of a linac commissioning test.

7.5   Conclusion

Dose delivered using dynamic MLC leaves to track the position of a moving target was validated for the first time on the Elekta MR-linac, using PRESAGE® 3D dosimeters. This statement is supported by the agreement between simulations and measurements, and by the data obtained with samples irradiated in static

and tracking scenarios.

Chapter 8

Discussion, future work and final conclusion

This chapter summarizes the main findings of this thesis. The contributions to the field of 3D dosimetry and MRgRT are discussed and compared with the available literature in the field.

8.1 Discussion and outlook

In this PhD project, I have assessed the value of using PRESAGE® 3D dosimeters to provide confidence in the safe delivery of MRgRT using the treatment adaptation workflows of the Elekta MR-linac.

In a first step, I showed that PRESAGE® samples are suitable for dose measurements, as they have a linear dose-response that is not affected by the presence of a magnetic field (chapter 4). Initial dose profiles measured with cylindrically shaped PRESAGE® samples were compared with MC simulations. The results showed how accurately dose changes resulting from the ERE could be identified with these dosimeters, given the excellent agreement with MC calculation. However, the strength of using PRESAGE® dosimeters is their ability to measure volumetric dose distributions. Initially, this could not be accurately obtained since these dosimeters displayed an increased dose-response from their central region to their edges. By the time these experiments were performed, a study mentioning similar results using large samples of PRESAGE® was published [49]. The authors explained the results as being caused by a real spatial non-uniform response of the samples to dose. The experiments performed in this PhD confirmed these findings.

At the time of these experiments, there were no studies aiming to compensate for this non-uniform spatial response of PRESAGE® samples to dose. Studies which successfully used PRESAGE® dosimeters always avoided using the samples' extremities [155, 169, 170]. Nevertheless, measuring at the PRESAGE® 3D dosimeters' interfaces was necessary to meet the goals of identifying dose changes due to the ERE. To explore whether this could be achieved, I performed a comprehensive investigation of multiple PRESAGE® samples to study their spatial response to dose. In chapter 5, the issue of measuring dose at the interfaces was solved to a clinically acceptable degree by correcting each irradiated sample of PRESAGE® with information obtained from uniformly irradiated calibration samples manufactured with the same *Formulation*. This study proved to be

of crucial importance for the experiments performed at the MR-linac, enabling measuring 3D dose data using the full volume of the dosimeters. The good agreement between the measured and the simulated dose distributions at the interfaces affected by the ERE, suggested that the TPS of the MR-linac was correctly modelling the magnetic field effect on the dose distribution. An alternative method was also investigated whereby the edges of the samples were physically removed. This is acceptable, assuming that larger samples are acquired and that they are used shortly after their modification.

A combination of both methods (correction image and physical edge removal) was applied to the samples used as part of the E2E tests performed to validate the online treatment adaptation workflows of the Elekta MR-linac (chapter 6). The measured dose distributions had an excellent agreement with calculations, which gives confidence that each step of the workflow is within specifications.

The accuracy of the process was confirmed from information acquired in all three dimensions, data that could not be retrieved using 1D or even 2D detectors. In particular, the experiments in which an air cavity was present within a sample of PRESAGE®, could not have been done with films. Arrays of detectors, which reconstruct dose in 3D, would also not be able to reproduce such geometry. Other groups have measured the dose changes due to the ERE, but they were not able to accurately determine it in 3D or at a clinically used RT dose level [35, 83, 123, 133]. The same E2E phantom/PRESAGE® set-up, CT scan and the readout methodology applied in chapter 6, was used to validate MLC-tracked RT (chapter 7). The benefits of tracking a moving target were demonstrated experimentally for the first time at the Elekta MR-linac.

For all the experiments performed in this thesis, 3D gamma passing rates (3%/3mm) were always within 98% and 100% for the measurements with small samples surrounded by air. For the experiments representative of prostate RT gamma passing rates were within 97% and 100% for the same criteria. Although PRESAGE® samples only investigated a portion of the treatment volume, the calculated gamma passing rates were higher than the clinically accepted limits

(>95% passing for 3%/3mm) [93, 96]. Our results are comparable, and even slightly better, to what has been achieved by other groups using PRESAGE® 3D dosimeters [24, 139] and other 3D gels [65, 158] , which showed passing rates of 96% to 99% by avoiding the dosimeters' edges.

The need for accurate 3D dose verification of MRgRT systems has prompted the investigation of new 3D dosimeters and techniques suitable for the purpose. Two recent studies used MR-readable 3D dosimeters as E2E tests to validate the adaptation workflows of the Elekta MR-linac [158] and the ViewRay system [65]. In the first study, the authors used a commercially available 3D gel from RTSafe, which was able to report measurable dose distributions in less than 30 min after irradiation, without being removed from the MR-linac. Though, they compromised the resolution of the MR-obtained 3D image of the gel to values lower than what is currently achievable with TPS calculations (1.5 x1.5 x 2mm^3 voxel size). In this thesis, I showed that dose readout could be as fast as reported for the RTsafe 3D gel and that the obtained dose distributions can be acquired with higher resolution ($<(1mm)^3$). Not using an MRI scanner can have additional advantages as a workflow can be performed whereby several 3D dosimeters can be irradiated sequentially and readout at a later stage using more readily available equipment.

In the second study, the authors created a phantom with different insert materials of air and bone and the dose was readout 24h after irradiation [65]. As in this thesis, they used 3D gels successfully to evaluate the accuracy of the online adaptive workflows of an MRgRT system, but changed the position of one of the inserts before re-optimizing the plan. Their gamma passing rates where within 93% and 96% for a 3%/3mm criteria which is slightly lower than what is usually achievable with PRESAGE® dosimeters.

Both studies, which required the gels to be within containers, also did not attempt to perform the challenging measurements at the interfaces of different density materials where the ERE occurs. This effect was investigated by another study in which MR-readable 3D gels with equivalent lung densities were developed

[133]. The author identified changes in dose due to the ERE by comparing measured data at a conventional linac and at an MR-linac. However, they did not benchmark their finding against simulations. These results are promising, but so far, PRESAGE® samples were the only 3D dosimeters to measure the ERE successfully by comparing it with calculations.

8.2   Future work

This study laid the foundation of performing E2E tests with PRESAGE® samples, which can subsequently be applied for commissioning tests of new linacs to be installed or updated at the RMH in Sutton. The methodology developed in this thesis proved to be quite versatile, as it permitted the validation of different types of treatments (e.g. adapted RT workflows, MLC-tracked RT), with essentially the same set-up and sample readout. Additional work can still be done to make the image analysis readily accessible to other users in the future by, for example, having a graphical user interface. Another option is performing the analysis in the open-source software 3Dslicer. A toolbox for 3D dosimetry is currently available to download, but it would need to be tailored to the methodology presented here before it could be used [8].

The project was focused mainly on measuring dose distributions using the full volume of the samples. For the prostate plan study, the OAR and the PTV were only partially represented by the sample. Consequently, dose-volume histograms (DVHs) could not be obtained for a direct comparison with the OAR and the PTV. The use of DVHs metrics for the validation of the correct plan delivery can provide useful complementary information to the clinically used gamma criteria [212]. This metric has been obtained before using 3D dosimeters [130, 154, 158, 159]. Although obtaining DVHs from PRESAGE® measured data was not aimed as part of this project, this could be explored in the future using larger samples, in which the full PTV and OAR volumes are within the dosimeter. The optical-CT scanner can image samples of up to approximately 11cm diameter and the current

tank can be extended to fit samples larger than 6.5cm diameter.

The benefit of using 3D dosimeter as E2E test is undoubted as they are the only detectors able to measure real-3D dose by mimicking any shape and by comprising materials with clinically relevant densities as air, lung and bone. Nevertheless, the use of 3D dosimeters clinically is still hindered by the work required for their implementation. For example, some 3D dosimeters are not commercially available and require a demanding manufacturing process. With PRESAGE® dosimeters we do not have this issue as we can buy the samples. Nevertheless, one inconvenience of using PRESAGE® when measurements at the interfaces are required, is the need to obtain a correction image to account for the edge effect. This might be time-consuming considering the samples' spatial response changes with their age. To solve this issue (both the non-uniformity and stability over time), the manufacturers are currently working on new *Formations* which are less affected by light and have higher stability over time. In addition, the dosimeters have to be readout with an optical-CT, and a matching liquid needs to be prepared in-house to match a particular *Formulation*. The most challenging step is having to work with this viscous liquid. Alternative options to scan samples optically using only air, water or a solid tank have been investigated to solve this issue [11, 59, 168], which would facilitate the implementation of PRESAGE® dosimeters as a clinical tool. However, additional studies are still needed in this field in order to find a viable alternative.

In the future, it will be beneficial to explore 3D dosimeters that can be deformed [45, 87, 211], to validate the clinically available deformable image registration algorithms implemented in the MRgRT systems.

8.3 Conclusion

I covered several aspects of 3D dosimetry from sample readout and characterization to its use to verify clinical adaptive RT and MLC-tracked dose delivery at the Elekta MR-linac. I showed that PRESAGE® dosimeters provide reliable and

reproducible dose measurements which give confidence in their application for any linac and TPS QA, and to verify online adaptation workflows available in MRgRT systems. The implementation of this dosimeter as a clinical tool, requires finding alternatives to facilitate the optical-CT scanning process, by eliminating the need for a matching liquid, and develop samples with higher stability over time and with a spatial uniform dose-response.

The methodologies developed can be used in the future to validate other MRgRT systems' workflows. The correction applied to measure dose distributions at the PRESAGE® samples' interfaces will also be of relevance in other RT fields as lung SBRT.

References

[1] A T Abdul Rahman, E Bräuer-Krisch, T Brochard, J Adamovics, S K Clowes, D Bradley, and S J Doran. "Sophisticated test objects for the quality assurance of optical computed tomography scanners." *Physics in medicine and biology* 56.14 (2011), pp. 4177–99.

[2] J Adamovics and P Guo. "A new approach to radiochromic three- dimensional dosimetry-polyurethane". *Journal of physics. Conference series* 3 (2004), p. 172.

[3] J Adamovics and M J Maryanski. "Characterisation of PRESAGE: A new 3-D radiochromic solid polymer dosemeter for ionising radiation". *Radiation Protection Dosimetry* 120.1 (2006), pp. 107–112.

[4] J A Adamovics. *Patent Application Publication Pub . No .: US 2007 / 0020793 A*. 2007.

[5] J Adamson, Y Yang, T Juang, K Chisholm, L Rankine, J Adamovics, F F Yin, and M Oldham. "On the feasibility of polyurethane based 3D dosimeters with optical CT for dosimetric verification of low energy photon brachytherapy seeds". *Medical Physics* 41.7 (2014), pp. 1–9.

[6] E E Ahunbay, X Chen, E S Paulson, G P Chen, and A Li. "An End-to-End Verification of Online Adaptation Process on a High-Field MR-Linac". *International Journal of Radiation Oncology, Biology,Physics,* 102.3 (2018), S131.

[7]   S Al-Nowais and S J Doran. "CCD-based optical CT scanning of highly attenuating phantoms". *Journal of Physics: Conference Series* 164 (2009), p. 012023.

[8]   K M Alexander, C Pinter, J Andrea, G Fichtinger, and L J Schreiner. "Implementation of an efficient workflow process for gel dosimetry using 3D Slicer". *Journal of Physics: Conference Series* 573 (2015), p. 012042.

[9]   P Andreo, D T Burns, K Hohlfeld, M S Huq, T Kanai, F Laitano, V Smyth, and S Vynckier. *International Atomic Energy Agency, Absorbed Dose Determination in External Beam Radiotherapy, Technical Reports Series No. 398.* Tech. rep. Vienna, 2006.

[10]   A Appleby, E A Christman, and A Leghrouz. "Imaging of spatial radiation dose distribution in agarose gels using magnetic resonance". *Medical physics* 14.3 (1987).

[11]   S Bache, J Malcolm, J Adamovics, and M Oldham. "Optical-CT 3D dosimetry using Fresnel lenses with minimal refractive-index matching fluid". *PLoS ONE* 11.3 (2016), pp. 1–14.

[12]   S T Bache, T Juang, M D Belley, B F Koontz, J Adamovics, T T Yoshizumi, D G Kirsch, and M Oldham. "Investigating the accuracy of microstereotactic-body-radiotherapy utilizing anatomically accurate 3D printed rodent-morphic dosimeters". *Medical Physics* 42.2 (2015), pp. 846–855.

[13]   H Bainbridge, A Salem, R H.N. Tijssen, M Dubec, A Wetscherek, C V. Van Es, J Belderbos, C Faivre-Finn, and F McDonald. "Magnetic resonance imaging in precision radiation therapy for lung cancer". *Translational Lung Cancer Research* 6.6 (2017), pp. 689–707.

[14]   D L J Barten, D Hoffmans, M A Palacios, S Heukelom, and L J V Battum. "Suitability of EBT3 GafChromic film for quality assurance in MR-guided radiotherapy at 0.35 T with and without real-time MR imaging". *Phys Med Bio* 63.16 (2018), p. 165014.

[15] J L Bedford, M F Fast, S Nill, F M A McDonald, M Ahmed, V N Hansen, and U Oelfke. "Effect of MLC tracking latency on conformal volumetric modulated arc therapy (VMAT) plans in 4D stereotactic lung treatment". *Radiotherapy and Oncology* 117.3 (2015), pp. 491–495.

[16] S H Benedict, K M Yenice, D Followill, J M Galvin, W Hinson, B Kavanagh, P Keall, M Lovelock, S Meeks, L Papiez, T Purdie, R Sadagopan, M C Schell, B Salter, D J Schlesinger, A S Shiu, T Solberg, D Y Song, V Stieber, R Timmerman, W A Tomé, D Verellen, L Wang, and F F Yin. "Stereotactic body radiation therapy: The report of AAPM Task Group 101". *Medical Physics* 37.8 (2010), pp. 4078–4101.

[17] R I Berbeco, H Mostafavi, G C Sharp, and S B Jiang. "Towards fluoroscopic respiratory gating for lung tumours without radiopaque markers". *Physics in Medicine and Biology* 50.19 (2005), pp. 4481–4490.

[18] I Billas, H Bouchard, U Oelfke, and S Duane. "The effect of magnetic field strength on the response of Gafchromic EBT-3 film". *Physics in Medicine and Biology* 64.6 (2019), p. 9.

[19] G H Bol, J J W Lagendijk, and B W Raaymakers. "Compensating for the impact of non- stationary spherical air cavities on IMRT dose delivery in transverse magnetic fields". *Phys Med Bio* 60.2 (2015), pp. 755–768.

[20] G H Bol, S Hissoiny, J J W Lagendijk, and B W Raaymakers. "Fast online Monte Carlo-based IMRT planning for the MRI linear accelerator." *Physics in medicine and biology* 57.5 (2012), pp. 1375–1385.

[21] J T Booth, V Caillet, N Hardcastle, R O'Brien, K Szymura, C Crasta, B Harris, C Haddad, T Eade, and P J Keall. "The first patient treatment of electromagnetic-guided real time adaptive radiotherapy using MLC tracking for lung SABR". *Radiotherapy and Oncology* 121.1 (2016), pp. 19–25.

[22] S G Bosi, P Naseri, and C Baldock. "Light-scattering-induced artifacts in a complex polymer gel dosimetry phantom". *Applied Optics* 48.13 (2009), pp. 2427–2434.

[23] L W Brady, H P Heilmann, and M Molls. *New Tecnologies in Radiation Oncology*. 2006, p. 321. ISBN: 3-540-00321-5. arXiv: `arXiv:1011.1669v3`.

[24] S L Brady, W E Brown, C G Clift, S Yoo, and M Oldham. "Investigation into the feasibility of using PRESAGE/optical-CT dosimetry for the verification of gating treatments." *Physics in medicine and biology* 55.8 (2010), pp. 2187–201.

[25] A Bruschi, M Esposito, S Pini, A Ghirelli, G Zatelli, and S Russo. "How the detector resolution affects the clinical significance of SBRT pre-treatment quality assurance results". *Physica Medica* 49.September 2017 (2018), pp. 129–134.

[26] V Caillet, J T Booth, and P Keall. "IGRT and motion management during lung SBRT delivery". *Physica Medica* 44 (2017), pp. 113–122.

[27] V Caillet, P J Keall, E Colvill, N Hardcastle, R O'Brien, K Szymura, and J T Booth. "MLC tracking for lung SABR reduces planning target volumes and dose to organs at risk". *Radiotherapy and Oncology* 124.1 (2017), pp. 18–24.

[28] S Ceberg, M Falk, P M A Rosenschöld, H Cattell, H Gustafsson, P Keall, S S Korreman, J Medin, F Nordström, G Persson, A Sawant, M Svatos, J Zimmerman, and S Å J Bäck. "Tumor-tracking radiotherapy of moving targets; verification using 3D polymer gel, 2D ion-chamber array and biplanar diode array". *Journal of Physics: Conference Series* 250 (2010), pp. 235–239.

[29] L I Cervo, A KY Chao, A Sandhu, and S B Jiang. "The diaphragm as an anatomic surrogate for lung tumor motion". *Physics in Medicine and Biology* 54.11 (2009), pp. 3529–3541.

[30] H Chandarana, H Wang, R H N Tijssen, and I J Das. "Emerging role of MRI in radiation therapy". *Journal of Magnetic Resonance Imaging* 48.6 (2018), pp. 1468–1478.

[31] X Chen, P Prior, G P Chen, C J Schultz, X A Li, X Chen, P Prior, G Chen, C J Schultz, and X A Li. "Technical Note : Dose effects of 1 . 5 T transverse magnetic field on tissue interfaces in MRI-guided radiotherapy". 4797 (2016).

[32] K Y Cheng, L L Hsieh, and C T Shih. "A Comprehensive evaluation of NIPAM polymer gel dosimeters on three orthogonal planes and temporal stability analysis". *PLoS ONE* 11.5 (2016), pp. 1–11.

[33] P Cherry and A Duxbury. *Pratical Radiotherapy: Physics and Equipment*. 1. 2009, pp. 1–5. ISBN: 9780874216561. arXiv: `arXiv:1011.1669v3`.

[34] B Cho, P Poulsen, D Ruan, A Sawant, and P J Keall. "Experimental investigation of a general real-time 3D target localisation method using sequential kV imaging combined with respiratory monitoring". *Phys Med Bio* 57.22 (2012), pp. 1–7395–407. arXiv: `NIHMS150003`.

[35] G W Choi. "Measurement of the Electron Return Effect Using PRESAGE Dosimeter. UT GSBS Diss. Theses (Open Access)". PhD thesis. 2016.

[36] C Clark, E Gershkevitsh, W Lechner, J V Dyk, D Venencia, T Bokulic, P Kazantsev, and P Wesolowska. *IAEA Supported National End -to- End Audit Programme for Dose Delivery Using Intensity- Modulated Radiation Therapy through On-Site Visits to Radiation Therapy Institutions*. Tech. rep. February. 2019, pp. 1–30.

[37] C Clift, A Thomas, J Adamovics, Z Chang, I Das, and M Oldham. "Toward acquiring comprehensive radiosurgery field commissioning data using the PRESAGE/optical-CT 3D dosimetry system." *Physics in medicine and biology* 55.5 (2010), pp. 1279–93.

[38] E Colvill, J Booth, S Nill, M Fast, J Bedford, U Oelfke, M Nakamura, P Poulsen, E Worm, R Hansen, T Ravkilde, J S Rydhög, T Pommer, P M A Rosenschold, S Lang, M Guckenberger, C Groh, C Herrmann, D Verellen, K Poels, L Wang, M Hadsell, T Sothmann, O Blanck, and P Keall. "A dosimetric comparison of real-time adaptive and non-adaptive

radiotherapy: A multi-institutional study encompassing robotic, gimbaled, multileaf collimator and couch tracking". *Radiotherapy and Oncology* 119.1 (2016), pp. 159–165.

[39] F Costa, S Doran, J Adamovics, S Nill, I M Hanson, and U Oelfke. "Characterization of small PRESAGE℞ samples for measurements near the dosimeter edges". *IOP Conf. Series: Journal of Physics: Conf. Series 847* 1305 (2019), p. 012009.

[40] F Costa, S Doran, S Nill, S Duane, D Shipley, I Billas, J Adamovics, and U Oelfke. "Development of a methodology to study the effect of magnetic field on dose distributions in an MR-linac, using PRESAGE℞ and Monte Carlo calculations". *Journal of Physics: Conference Series* 847 (2017), p. 012058.

[41] F Costa, M J Menten, S Doran, J Adamovics, I M Hanson, S Nill, and U Oelfke. "Dose verification of dynamic MLC-tracked radiotherapy using small PRESAGE℞ 3D dosimeters and a motion phantom". *IOP Conf. Series: Journal of Physics: Conf. Series 847* 1305 (2019), p. 012068.

[42] F Costa, S J Doran, I M Hanson, S Nill, I Billas, D Shipley, S Duane, J Adamovics, and U Oelfke. "Investigating the effect of a magnetic field on dose distributions at phantom-air interfaces using PRESAGE 3D dosimeter and Monte Carlo simulations". *Physics in Medicine and Biology* 63.5 (2018), NT01.

[43] S P M Crijns, B W Raaymakers, and J J W Lagendijk. "Proof of concept of MRI-guided tracked radiation delivery: tracking one-dimensional motion." *Physics in medicine and biology* 57.23 (2012), pp. 7863–72.

[44] I J Das, C W Cheng, R J Watts, A Ahnesjö, J Gibbons, X A Li, J Lowenstein, R K Mitra, W E Simon, and T C Zhu. "Accelerator beam data commissioning equipment and procedures: Report of the TG-106 of the Therapy Physics Committee of the AAPM". *Medical Physics* 35.9 (2008), pp. 4186–4215.

[45] Y De Deene, P S Skyt, R Hil, and J T Booth. "FlexyDos3D: a deformable anthropomorphic 3D radiation dosimeter: radiation properties." *Physics in medicine and biology* 60.4 (2015), pp. 1543–63.

[46] Y De Deene, C Claeys, and C De Wagter. "Three dimensional radiation dosimetry in lung-equivalent regions by use of a radiation sensitive gel foam: Principles". *Journal of Physics: Conference Series* 56.1 (2006), pp. 256–258.

[47] J De Los Santos, R Popple, N Agazaryan, J E Bayouth, J P Bissonnette, M K Bucci, S Dieterich, L Dong, K M Forster, D Indelicato, K Langen, J Lehmann, N Mayr, I Parsai, W Salter, M Tomblyn, W T C Yuh, and I J Chetty. "Image guided radiation therapy (IGRT) technologies for radiation therapy localization and delivery". *International Journal of Radiation Oncology Biology Physics* 87.1 (2013), pp. 33–45.

[48] Y D Deene, P S Skyt, R Hil, and J T Booth. "FlexyDos3D : a deformable anthropomorphic 3D radiation dosimeter : radiation properties" (2015).

[49] K H Dekker, J J Battista, and K J Jordan. "Optical CT imaging of solid radiochromic dosimeters in mismatched refractive index solutions using a scanning laser and large area detector". *Medical Physics* 43.8 (2016), pp. 4585–4597.

[50] G Delaney, S Jacob, C Featherstone, and M Barton. "The role of radiotherapy in cancer treatment: Estimating optimal utilization from a review of evidence-based clinical guidelines". *Cancer* 104.6 (2005), pp. 1129–1137.

[51] G Delpon, A Escande, T Ruef, J Darréon, J Fontaine, C Noblet, S Supiot, T Lacornerie, and D Pasquier. "Comparison of Automated Atlas-Based Segmentation Software for Postoperative Prostate Cancer Radiotherapy". *Frontiers in Oncology* 6.August (2016), pp. 1–6.

[52] R Y J F Dempsey. "WECAUD04: Monte Carlo Simulations of Air Cavities in Phantoms Submerged in Magnetic Fields". *Medical physics.* 2007.

175

[53] T Depuydt, A Van Esch, and D P Huyskens. "A quantitative evaluation of IMRT dose distributions: refinement and clinical assessment of the gamma evaluation". *Radiotherapy and Oncology* 62.3 (2002), pp. 309–319.

[54] T Depuydt, K Poels, D Verellen, B Engels, C Collen, M Buleteanu, R Van Den Begin, M Boussaer, M Duchateau, T Gevaert, G Storme, and M De Ridder. "Treating patients with real-time tumor tracking using the Vero gimbaled linac system: Implementation and first review". *Radiotherapy and Oncology* 112.3 (2014), pp. 343–351.

[55] S Devic, J Seuntjens, E Sham, E B Podgorsak, C R Schmidtlein, A S Kirov, and C G Soares. "Precise radiochromic film dosimetry using a flat-bed document scanner". *Medical Physics* 32.7 (2005), p. 2245.

[56] S J Doran. "How to perform an optical CT scan: an illustrated guide". *Journal of Physics: Conference Series* 444 (2013), p. 012004.

[57] S J Doran. "The history and principles of chemical dosimetry for 3-D radiation fields: Gels, polymers and plastics". *Applied Radiation and Isotopes* 67.3 (2009), pp. 393–398.

[58] S J Doran and N Krstajić. "The history and principles of optical computed tomography for scanning 3-D radiation dosimeters". *Journal of Physics: Conference Series* 56 (2007), pp. 45–57.

[59] S J Doran and D N B Yatigammana. "Eliminating the need for refractive index matching in optical CT scanners for radiotherapy dosimetry: I. Concept and simulations". *Phys. Med. Biol. Phys. Med. Biol* 57.57 (2012), pp. 665–665.

[60] S J Doran, A T A Rahman, E Bräuer-Krisch, T Brochard, J Adamovics, A Nisbet, and D Bradley. "Establishing the suitability of quantitative optical CT microscopy of PRESAGE® radiochromic dosimeters for the verification of synchrotron microbeam therapy." *Physics in medicine and biology* 58.18 (2013), pp. 6279–97.

[61] S Dorsch, P Mann, C Lang, P Haering, A Runz, and C P Karger. "Feasibility of polymer gel-based measurements of radiation isocenter accuracy in magnetic fields". *Physics in Medicine and Biology* 63.11 (2018), p. 9.

[62] S Dorsch, P Mann, A Elter, A Runz, C K Spindeldreier, S Klüter, and C P Karger. "Measurement of isocenter alignment accuracy and image distortion of an 0.35 T MR-Linac system". *Phys. Med. Biol* 64.20 (2019), p. 205011.

[63] W D D'Souza, S A Naqvi, and C X Yu. "Real-time intra-fraction-motion tracking using the treatment couch: A feasibility study". *Physics in Medicine and Biology* 50.17 (2005), pp. 4021–4033.

[64] W van Elmpt, L McDermott, S Nijsten, M Wendling, P Lambin, and B Mijnheer. "A literature review of electronic portal imaging for radiotherapy dosimetry". *Radiotherapy and Oncology* 88.3 (2008), pp. 289–309.

[65] A Elter, S Dorsch, P Mann, A Runz, W Johnen, C K Spindeldreier, S Klüter, and C P Karger. "End-to-end test of an online adaptive treatment procedure in MR-guided radiotherapy using a phantom with anthropomorphic structures". *Phys Med Bio* 15;64.22 (2019), p. 225003.

[66] B G Fallone, B Murray, S Rathee, T Stanescu, S Steciw, S Vidakovic, E Blosser, and D Tymofichuk. "First MR images obtained during megavoltage photon irradiation from a prototype integrated linac-MR system." *Medical physics* 36.6 (2009), pp. 2084–2088.

[67] B Farhood, G Geraily, S Mohammad, and M Abtahi. "A systematic review of clinical applications of polymer gel dosimeters in radiotherapy". *Applied Radiation and Isotopes* 143.February 2018 (2019), pp. 47–59.

[68] M F Fast, S Nill, J L Bedford, and U Oelfke. "Dynamic tumor tracking using the Elekta Agility MLC". *Medical Physics* 41.11 (2014), p. 111719.

References

[69] M F Fast, B Eiben, M J Menten, A Wetscherek, D J Hawkes, J R McClelland, and U Oelfke. "Tumour auto-contouring on 2d cine MRI for locally advanced lung cancer: A comparative study". *Radiotherapy and Oncology* 125.3 (2017), pp. 485–491.

[70] M Glitzner, P L Woodhead, P T S Borman, J J W Lagendijk, and B W Raaymakers. "Technical note: MLC-tracking performance on the Elekta unity MRI-linac". *Physics in Medicine & Biology* 64.15 (2019), 15NT02.

[71] J C Gore, Y S Kang, and R J Schulz. "Measurement of radiation dose distributions by NMR imaging". *Magnetic Resonance Imaging* 2.3 (2004), p. 244.

[72] J C Gore, M Ranade, M J Maryanski, and R J Schulz. "Radiation dose distributions in three dimensions from tomographic optical density scanning of polymer gels: II. Optical properties of the BANG polymer gel." *Physics in medicine and biology* 41.12 (1996), pp. 2705–2717.

[73] M Guckenberger. "Image-guided Radiotherapy Based on Kilovoltage Cone-beam Computed Tomography A Review of Technology and Clinical Outcome". *European Oncology & Haematology* 07.02 (2011), p. 121.

[74] P Y Guo, J A Adamovics, and M Oldham. "A practical three-dimensional dosimetry system for radiation therapy". *Medical Physics* 33.10 (2006), p. 3962.

[75] P Y Guo, J A Adamovics, and M Oldham. "Characterization of a new radiochromic three-dimensional dosimeter". *Medical Physics* 33.5 (2006), pp. 1338–1345. arXiv: NIHMS150003.

[76] X Han. "MR-based synthetic CT generation using a deep convolutional neural network method:" *Medical Physics* 44.4 (2017), pp. 1408–1419.

[77] E K Hansen, M K Bucci, J M Quivey, V Weinberg, and P Xia. "Repeat CT imaging and replanning during the course of IMRT for head-and-neck cancer". *International Journal of Radiation Oncology Biology Physics* 64.2 (2006), pp. 355–362.

[78] U A van der Heide, A C Houweling, G Groenendaal, R G H Beets-Tan, and P Lambin. "Functional MRI for radiotherapy dose painting". *Magnetic Resonance Imaging* 30.9 (2012), pp. 1216–1223.

[79] S T Heijkoop, T R Langerak, S Quint, L Bondar, J W M Mens, B J M Heijmen, and M S Hoogeman. "Clinical implementation of an online adaptive plan-of-the-day protocol for nonrigid motion management in locally advanced cervical cancer IMRT". *International Journal of Radiation Oncology Biology Physics* 90.3 (2014), pp. 673–679.

[80] T C F van Heijst, M D den Hartogh, J J W Lagendijk, H J G D van den Bongard, and B van Asselen. "MR-guided breast radiotherapy: feasibility and magnetic-field impact on skin dose." *Physics in medicine and biology* 58.17 (2013), pp. 5917–30.

[81] S Hissoiny, A J E Raaijmakers, B Ozell, P Després, and B W Raaymakers. "Fast dose calculation in magnetic fields with GPUMCD". *Physics in Medicine and Biology* 56.16 (2011), pp. 5119–5129.

[82] S Hissoiny, B Ozell, H Bouchard, and P Després. "GPUMCD: A new GPU-oriented Monte Carlo dose calculation platform". *Medical Physics* 38.2 (2011), pp. 754–764.

[83] S Höfel, M K Fix, F Zwicker, E Sterpin, and M Drescher. "EPR imaging of magnetic field effects on radiation dose distributions around millimeter-size air cavities". *Physics in Medicine & Biology* 64.17 (2019), p. 175013.

[84] D Hoffmans, O Bohoudi, N Niebuhr, A Pfaffenberger, L Battum, B Slotman, M Palacios, A Bruynzeel, and F Lagerwaard. "OC-0409: A film-based end-to-end test for MR-guided online adaptive radiotherapy". *Radiotherapy and Oncology,* 127 (2018), S209 –S210.

[85] P Hoskin. *External Beam Therapy (Radiotherapy in Practice).* 2 edition. OUP Oxford, 2012.

[86] A C Houweling, J H W De Vries, J Wolthaus, S Woodings, J G M Kok, B Van Asselen, K Smit, A Bel, J J W Lagendijk, and B W Raaymakers. "Performance of a cylindrical diode array for use in a 1.5 T MR-linac". *Physics in Medicine and Biology* 61.3 (2016), N80–N89.

[87] E M Høye, P Balling, E S Yates, L P Muren, J B B Petersen, and P S Skyt. "Eliminating the dose-rate effect in a radiochromic silicone-based 3D dosimeter". *Physics in Medicine and Biology* 60.14 (2015), pp. 5557–5570.

[88] A Hunt, V N Hansen, U Oelfke, S Nill, and S Hafeez. "Adaptive Radiotherapy Enabled by MRI Guidance". *Clinical Oncology* 30.11 (2018), pp. 711–719.

[89] Coen W. Hurkmans, Peter Remeijer, Joos V. Lebesque, and Ben J. Mijnheer. "Set-up verification using portal imaging; review of current clinical practice". *Radiotherapy and Oncology* 58.2 (2001), pp. 105–120.

[90] G S Ibbott, Y Roed, H Lee, M Alqathami, J Wang, L Pinsky, and A Blencowe. "Gel dosimetry enables volumetric evaluation of dose distributions from an MR-guided linac". *AIP Conference Proceedings* 1747 (2016).

[91] G S Ibbott, A Molineu, and D S Followill. "Independent evaluations of IMRT through the use of an anthropomorphic phantom". *Technology in Cancer Research and Treatment* 5.5 (2006), pp. 481–487.

[92] G S Ibbott, H J Le, and Y Roe. "The MD Anderson experience with 3D dosimetry and an MR-linac". *Journal of Physics: Conference Series* 1305 (2019), p. 012011.

[93] International Atomic Energy Agency. *International Atomic Energy Agency (IAEA). Accuracy Requirements and Uncertainties in Radiotherapy*. Tech. rep. 2. Vienn, 2014, pp. 320–322.

[94] J Jackson, T Juang, J Adamovics, and M Oldham. "An investigation of PRESAGE 3D dosimetry for IMRT and VMAT radiation therapy treatment verification". *Physics in Medicine and Biology* 60.6 (2015), pp. 2217–2230.

[95]   D A Jaffray, D G Drake, M Moreau, A A Martinez, and J W Wong. "A ra-diographic and tomographic imaging system integrated into a medical linear accelerator for localization of bone and soft-tissue targets". *International Journal of Radiation Oncology Biology Physics* 45.3 (1999), pp. 773–789.

[96]   H James, A Beavis, G Budgell, C Clark, D Convery, and J Mott. *IPEM Report 96: Guidance for the clinical implementation of intensity modulated radiation therapy*. Tech. rep. York, 2008.

[97]   U Jelen and J Begg. "Dosimetry needs for MRI-linacs". *Journal of Physics: Conference Series* 1305 (2019), p. 012010.

[98]   J H Jonsson, M G Karlsson, M Karlsson, and T Nyholm. "Treatment planning using MRI data: An analysis of the dose calculation accuracy for different treatment regions". *Radiation Oncology* 5.1 (2010), pp. 1–8.

[99]   K Jordan and N Avvakumov. "Radiochromic leuco dye micelle hydrogels: I. Initial investigation". *Physics in Medicine and Biology* 54.22 (2009), pp. 6773–6789.

[100] T Juang, J Newton, M Niebanck, R Benning, J Adamovics, and M Oldham. "Customising PRESAGE®️ for diverse applications". *Journal of physics. Conference series* 444 (2013), p. 012029.

[101] C Kamerling, M Fast, P Ziegenhein, M Menten, S Nill, and U Oelfke. "TH-AB-303-06: Real-time 4D dose reconstruction for tracked dynamic MLC deliveries in the presence of respiratory motion". *Med. Phys.* 2015, 42:3712.

[102] W Kaplan. *Background Paper 6.5 Cancer and Cancer Therapeutics*. Tech. rep. April. 2013.

[103] I Kawrakow, E Mainegra-Hing, F Tessier, and B R B Walters. *The EGSnrc C++ class library, NRC Report PIRS-898 (rev A)*. Tech. rep. Ottawa, Canada, 2009.

[104] I. Kawrakow, E. Mainegra-Hing, D.W.O. Rogers, F. Tessier, and B.R.B. Walters. *The EGSnrc Code System : Monte Carlo Simulation of Electron and Photon Transport*. 2016. ISBN: {NRCC} {REPORT} {PIRS-701}.

[105] P J Keall, M Barton, and S Crozier. "The Australian Magnetic Resonance Imaging-Linac Program". *Seminars in Radiation Oncology* 24.3 (2014), pp. 203–206.

[106] P J Keall, E Colvill, R O'Brien, J A Ng, P R Poulsen, T Eade, A Kneebone, and J T Booth. "The first clinical implementation of electromagnetic transponder-guided MLC tracking". *Medical Physics* 41.2 (2014), pp. 020702–1.

[107] R G Kelly, K J Jordan, and J J Battista. "Optical CT reconstruction of 3D dose distributions using the ferrous- benzoic-xylenol (FBX) gel dosimeter". *Medical Physics* 25.9 (1998), pp. 1741–1750.

[108] D Khezerloo, H A Nedaie, A Takavar, A Zirak, B Farhood, H Movahedinejhad, N Banaee, I Ahmadalidokht, and C Knuap. "PRESAGE® as a solid 3-D radiation dosimeter: A review article". *Radiation Physics and Chemistry* 141 (2017), pp. 88–97.

[109] W Kilby, J R Dooley, G Kuduvalli, S. Sayeh, and C R Maurer. "The CyberKnife® robotic radiosurgery system in 2010". *Technology in Cancer Research and Treatment* 9.5 (2010), pp. 433–452.

[110] C Kirkby, T Stanescu, S Rathee, M Carlone, B Murray, and B G Fallone. "Patient dosimetry for hybrid MRI-radiotherapy systems". *Medical Physics* 35.3 (2008), p. 1019.

[111] E E Klein, J Hanley, J Bayouth, F F Yin, W Simon, S Dresser, C Serago, F Aguirre, L Ma, B Arjomandy, C Liu, C Sandin, and T Holmes. "Task Group 142 report: Quality assurance of medical accelerators". *Medical Physics* 36.9 (2009), p. 4197.

[112] C Kontaxis, G H Bol, J J W Lagendijk, and B W Raaymakers. "A new methodology for inter- and intrafraction plan adaptation for the MR-linac". *Physics in Medicine and Biology* 60.19 (2015), pp. 7485–7497.

[113] A Krauss, S Nill, M Tacke, and U Oelfke. "Electromagnetic real-time tumor position monitoring and dynamic multileaf collimator tracking using a siemens 160 MLC: Geometric and dosimetric accuracy of an integrated system". *International Journal of Radiation Oncology Biology Physics* 79.2 (2011), pp. 579–587.

[114] N Krstajić and S J Doran. "Focusing optics of a parallel beam CCD optical tomography apparatus for 3D radiation gel dosimetry." *Physics in medicine and biology* 51.8 (2006), pp. 2055–2075.

[115] J J W Lagendijk and C J G Bakker. "MRI guided radiotherapy - A MRI based linear accelerator". *Radiotherapy and Oncology Volume 56, Supplement 1, ESTRO, Istanbul.* 2000.

[116] J J W Lagendijk, B W Raaymakers, C A T Van Den Berg, M A Moerland, M E Philippens, and M Van Vulpen. "MR guidance in radiotherapy". *Physics in Medicine and Biology* 59.21 (2014), R349–R369.

[117] J J W Lagendijk, B W Raaymakers, A J E Raaijmakers, J Overweg, K J Brown, E M Kerkhof, R W van der Put, B Hårdemark, M van Vulpen, and U A van der Heide. "MRI/linac integration". *Radiotherapy and Oncology* 86.1 (2008), pp. 25–29.

[118] T Landberg, J Chavaudra, J Dobbs, G Hanks, K A Johansson, T Möller, and J Purdy. *ICRU Report 50: Prescribing, Recording, and Reporting Photon-Beam Intensity-Modulated Radiation Therapy.* Tech. rep. 1993.

[119] T Landberg, J Chavaudra, J Dobbs, J P Gerard, G Hanks, J C Horiot, K A Johansson, T Möller, J Purdy, N Suntharalingam, and H Svensson. *ICRU Report 62: Prescribing, Recording, and Reporting Photon-Beam Intensity-Modulated Radiation Therapy (Supplement to ICRU Report 50).* Tech. rep. 1999.

[120] H J Lee. "Volumetric, Magnetic Resonance-Visible, and Radiation-Sensitive Detectors for Magnetic Resonance Image-Guided Radiation Therapy". PhD thesis. 2017.

[121] H J Lee, Y Roed, S Venkataraman, M Carroll, and G S Ibbott. "Investigation of magnetic field effects on the dose-response of 3D dosimeters for magnetic resonance - image guided radiation therapy applications". *Radiotherapy and Oncology* 125.3 (2017), pp. 426–432.

[122] H J Lee, M Kadbi, G Bosco, and G S Ibbott. "Real-time volumetric relative dosimetry for magnetic resonance - Image-guided radiation therapy (MR-IGRT)". *Physics in Medicine and Biology* 63.4 (2018), p. 045021.

[123] H J Lee, G W Choi, M Alqathami, M Kadbi, and I Geoffrey. "Using 3D dosimetry to quantify the Electron Return Effect (ERE) for MR-image-guided radiation therapy (MR-IGRT) applications". *IOP Conf. Series: Journal of Physics: Conf. Series 847* 012057 (2017).

[124] H H Li, V L Rodriguez, O L Green, Y Hu, R Kashani, H O Wooten, D Yang, and S Mutic. "Patient-specific quality assurance for the delivery of 60 Co intensity modulated radiation therapy subject to a 0.35 T lateral magnetic field". *Int J Radiat Oncol Biol Phys* 91.1 (2015), pp. 67–72.

[125] S C Lillicrap. *IPEM Report No. 81: Physics Aspects of Quality Control in Radiotherapy*. Tech. rep. 3. 2000, pp. 815–815.

[126] S C Lillicrap, B Owen, J R Williams, and P C Williams. "Code of Practice for high-energy photon therapy dosimetry based on the NPL absorbed dose calibration service". *Physics in Medicine and Biology* 35.10 (1990), pp. 1355–1360.

[127] D A Low, W B Harms, S Mutic, and J A Purdy. "A technique for the quantitative evaluation of dose distributions". *Med Phys* 25.5 (1998), pp. 656–661.

[128] C Ma and D W O Rogers. "BEAMDP Users Manual". *National Research Council of Canada Report PIRS-0509(C) revA* (2016).

[129] V N Malkov and D W O Rogers. "Charged particle transport in magnetic fields in EGSnrc". *Medical Physics* 43.7 (2016), pp. 4447–4458.

[130] P Mann, M Witte, T Moser, C Lang, A Runz, W Johnen, M Berger, J Biederer, and C P Karger. "3D dosimetric validation of motion compensation concepts in radiotherapy using an anthropomorphic dynamic lung phantom". *Physics in Medicine and Biology* 62.2 (2017), pp. 573–595.

[131] M Mathis, G Sawakuchi, D Flint, R Tailor, S Beddar, G Ibbott, and Z Wen. "Effects of a strong magnetic field on selected radiation dosimeters (TLD , OSLD , EBT3 film , PRESAGE)". *Electronic Presentation Online System* (2014), pp. 1–8.

[132] P Mayles, A Nahum, and J C Rosenwald. *Handbook of Radiotherapy Physics: Theory and Practice*. CRC Press, 2007. ISBN: 9788578110796. arXiv: `arXiv:1011.1669v3`.

[133] B A McDonald, H J Lee, and G S Ibbott. "Low-Density Gel Dosimeter for Measurement of the Electron Return Effect in an MR-Linac". *Phys Med Bio* December 2016 (2018), pp. 11–14.

[134] C M McErlean. "Quantitative three-dimensional imaging in cancer research using optical computed tomography A Thesis submitted for the degree of". PhD thesis. 2016, pp. 1–166.

[135] C M McErlean, E Bräuer-Krisch, J Adamovics, and S J Doran. "Assessment of optical CT as a future QA tool for synchrotron x-ray microbeam therapy." *Physics in medicine and biology* 61.1 (2016), pp. 320–37.

[136] H A McNair, J Brock, J R N Symonds-Tayler, S Ashley, S Eagle, P M Evans, A Kavanagh, N Panakis, and M Brada. "Feasibility of the use of the Active Breathing Co ordinator (ABC) in patients receiving radical radiotherapy for non-small cell lung cancer (NSCLC)". *Radiotherapy and Oncology* 93.3 (2009), pp. 424–429.

[137] D W McRobbie, E A Moore, M J Graves, and M R Prince. *MRI: From Picture to Proton*. 2nd editio. 2007, p. 402. ISBN: 9780521865272. arXiv: `arXiv:1011.1669v3`.

[138] I Meijsing, B W Raaymakers, A J E Raaijmakers, J G M Kok, L Hogeweg, B Liu, and J J W Lagendijk. "Dosimetry for the MRI accelerator: the impact of a magnetic field on the response of a Farmer NE2571 ionization chamber." *Physics in medicine and biology* 54.10 (2009), pp. 2993–3002.

[139] S Mein, L Rankine, J Adamovics, H Li, and M Oldham. "Development of a 3D remote dosimetry protocol compatible with MRgIMRT". *Medical Physics* (2017).

[140] M J Menten, M Guckenberger, C Herrmann, A Krau, S Nill, U Oelfke, and J Wilbert. "Comparison of a multileaf collimator tracking system and a robotic treatment couch tracking system for organ motion compensation during radiotherapy". *Medical Physics* 39.11 (2012), pp. 7032–7041.

[141] M J Menten, M F Fast, S Nill, C P Kamerling, F McDonald, and U Oelfke. "Lung stereotactic body radiotherapy with an MR-linac Quantifying the impact of the magnetic field and real-time tumor tracking". *Radiotherapy and Oncology* 119.3 (2016), pp. 461–466.

[142] M J Menten, M F Fast, A Wetscherek, C M Rank, M Kachelrieß, D J Collins, S Nill, and U Oelfke. "The impact of 2D cine MR imaging parameters on automated tumor and organ localization for MR-guided real-time adaptive radiotherapy". *Physics in Medicine and Biology* 63.23 (2018), p. 16.

[143] M J Menten, M F Fast, C P Kamerling, P Ziegenhein, S Nill, and U Oelfke. "Validation of the accuracy of a novel online dose reconstruction method using linac log files". *Proceedings of the International Conference on the use of Computers in Radiation Therapy*. 2016.

[144] A Micke, D F Lewis, and X Yu. "Multichannel film dosimetry with nonuniformity correction". *Medical Physics* 38.5 (2011), p. 2523.

[145]   B J Mijnheer. *Clinical 3D Dosimetry in Modern Radiation Therapy (Imaging in Medical Diagnosis and Therapy)*. 1 edition. CRC Press, 2017.

[146]   A Mostaar, B Hashemi, M H Zahmatkesh, S M R Aghamiri, and S R Mahdavi. "A basic dosimetric study of PRESAGE: the effect of different amounts of fabricating components on the sensitivity and stability of the dosimeter." *Physics in medicine and biology* 55.3 (2010), pp. 903–912.

[147]   S Mutic and J F Dempsey. "The ViewRay System: Magnetic Resonance-Guided and Controlled Radiotherapy". *Seminars in Radiation Oncology* 24.3 (2014), pp. 196–199.

[148]   R Nath, P J Biggs, F J Bova, C C Ling, J A Purdy, J Van de Geijn, and M S Weinhous. "AAPM code of practice for radiotherapy accelerators: Report of AAPM Radiation Therapy Task Group No. 45". *Medical Physics* 21.7 (1994), pp. 1093–1121.

[149]   B E Nelms, M F Chan, G Jarry, M Lemire, J Lowden, C Hampton, and V Feygelman. "Evaluating IMRT and VMAT dose accuracy: practical examples of failure to detect systematic errors when applying a commonly used metric and action levels." *Medical physics* 40.11 (2013), p. 111722.

[150]   L I C No, J Du, and S B Jiang. "MRI-guided tumor tracking in lung cancer radiotherapy". *Phys Med Bio* 56.13 (2011), pp. 3773–3785.

[151]   P Norlin, O Öberg, S Junique, W Kaplan, J Y Andersson, and G Nilsson. "A cubic isotropic X-ray dose detector diode fabricated by DRIE of SOI substrates". *Sensors and Actuators, A: Physical* 213 (2014), pp. 116–121.

[152]   D J O'Brien and G O Sawakuchi. "Monte Carlo study of the chamber-phantom air gap effect in a magnetic field:" *Medical Physics* 44.7 (2017), pp. 3830–3838.

[153]   D J O'Brien, D A Roberts, G S Ibbott, and G O Sawakuchi. "Reference dosimetry in magnetic fields: formalism and ionization chamber correction factors". *Medical Physics* 43.8 (2016), pp. 4915–4927.

[154]   M Oldham, A Thomas, J O Daniel, T Juang, G S Ibbott, J Adamovics, and J P Kirkpatrick. "A Quality Assurance Method that Utilizes 3D Dosimetry and Facilitates Clinical Interpretation". *Radiation Oncology Biology* 84.2 (2012), pp. 540–546.

[155]   M Oldham, H Sakhalkar, P Guo, and J Adamovics. "An investigation of the accuracy of an IMRT dose distribution using two- and three-dimensional dosimetry techniques." *Medical physics* 35.2008 (2008), pp. 2072–2080.

[156]   K Otto. "Volumetric modulated arc therapy: IMRT in a single gantry arc". *Medical Physics* 35.1 (2008), pp. 310–317.

[157]   Alexander P, Charlesby A, and Ross M. "The degradation of solid poly-methylmethacrylate by ionizing radiation". *Proceedings of the Royal Society* A223.392 (1954).

[158]   E Pappas, G Kalaitzakis, T Boursianis, E Zoros, K Zourari, E P Pappas, D Makris, I Seimenis, E Efstathopoulos, and T G Maris. "Dosimetric performance of the Elekta Unity MR-linac system: 2D and 3D dosimetry in anthropomorphic inhomogeneous geometry". *Physics in Medicine & Biology* 22;64.22 (2019), p. 225009.

[159]   J F Pavoni, W F P Neves-Junior, M A Da Silveira, C M K Haddad, and O Baffa. "Evaluation of a composite Gel-Alanine phantom on an end-to-end test to treat multiple brain metastases by a single isocenter VMAT technique". *Medical Physics* 44.9 (2017), pp. 4869–4879.

[160]   T J Perik, J J Kaas, S Greilich, J W H Wolthaus, and F W Wittkamper. "The characterization of a large multi-axis ionization chamber array in a 1.5 T MRI linac". *Physics in Medicine and Biology* 63.22 (2018), p. 225007.

[161]   E B Podgorsak. *Radiation Oncology Physics : A Handbook for Teachers and Students.* Vienna, 2005.

[162]   A J E Raaijmakers, B Hårdemark, B W Raaymakers, C P J Raaijmakers, and J J W Lagendijk. "Dose optimization for the MRI-accelerator: IMRT in the presence of a magnetic field". *Physics in Medicine and Biology* 52.23 (2007), pp. 7045–7054.

[163]   A J E Raaijmakers, B W Raaymakers, and J J W Lagendijk. "Integrating a MRI scanner with a 6 MV radiotherapy accelerator: dose increase at tissue-air interfaces in a lateral magnetic field due to returning electrons." *Physics in medicine and biology* 50.7 (2005), pp. 1363–1376.

[164]   A J E Raaijmakers, B W Raaymakers, S van der Meer, and J J W Lagendijk. "Integrating a MRI scanner with a 6 MV radiotherapy accelerator: impact of the surface orientation on the entrance and exit dose due to the transverse magnetic field". *Physics in medicine and biology* 52.4 (2007), 929–939 PHYSICS.

[165]   B W Raaymakers, I M Jürgenliemk-Schulz, G H Bol, M Glitzner, A N T J Kotte, B van Asselen, J C J de Boer, J J Bluemink, S L Hackett, M A Moerland, S J Woodings, J W H Wolthaus, H M van Zijp, M E P Philippens, R Tijssen, J G M Kok, E N de Groot-van Breugel, I Kiekebosch, L T C Meijers, C N Nomden, G G Sikkes, P A H Doornaert, W S C Eppinga, N Kasperts, L G W Kerkmeijer, J H A Tersteeg, K J Brown, B Pais, P Woodhead, and J J W Lagendijk. "First patients treated with a 1.5 T MRI-Linac : clinical proof of concept of a high-precision , high-field MRI guided radiotherapy treatment". *Phys Med Bio* 62.23 (2017), pp. L41–L50.

[166]   B W Raaymakers, J J W Lagendijk, J Overweg, J G M Kok, A J E Raaijmakers, E M Kerkhof, R W van der Put, I Meijsing, S P M Crijns, F Benedosso, M van Vulpen, C H W de Graaff, J Allen, and K J Brown. "Integrating a 1.5 T MRI scanner with a 6 MV accelerator: proof of concept." *Physics in medicine and biology* 54.12 (2009), N229–N237.

[167]   B W Raaymakers, A J E Raaijmakers, A N T J Kotte, D Jette, and J J W Lagendijk. "Integrating a MRI scanner with a 6 MV radiotherapy

accelerator: dose deposition in a transverse magnetic field". *Phys. Med. Biol* 49.17 (2004), pp. 4109–18.

[168]   L Rankine and M Oldham. "On the feasibility of optical-CT imaging in media of different refractive index". *Med Phys* 40.5 (2013), p. 051701.

[169]   L J Rankine, S Mein, B Cai, A Curcuru, T Juang, D Miles, S Mutic, Y Wang, M Oldham, and H H Li. "Three-Dimensional Dosimetric Validation of a Magnetic Resonance-Guided Intensity Modulated Radiation Therapy System". *International Journal of Radiation Oncology*Biology*Physics* 97.5 (2017), pp. 1095–1104.

[170]   J Rehman, T Iqbal, R Tailor, A Majid, J Ashraf, I Khan, M Afzal, and G S Ibbott. "Dosimetric comparison among different head and neck radiotherapy techniques using PRESAGE® dosimeter". *international journal of Cancer Therapy and Oncology* 3.4 (2015), pp. 1–9.

[171]   S Reinhardt, M Hillbrand, J J Wilkens, and W Assmann. "Comparison of Gafchromic EBT2 and EBT3 films for clinical photon and proton beams". *Med. Phys.* 39.8 (2012), pp. 5257–5262.

[172]   M Reynolds, B G Fallone, and S Rathee. "Dose response of selected ion chambers in applied homogeneous transverse and longitudinal magnetic fields M." *Medical Physics* 40.4 (2013), p. 042102.

[173]   F J Reynoso, A Curcuru, O Green, S Mutic, I J Das, and L Santanam. "Technical Note: Magnetic field effects on Gafchromic-film response in MR-IGRT". *Medical Physics* 43.12 (2016), pp. 6552–6556.

[174]   A E Saarnak, M Boersma, B N F M van Bunningen, R Wolterink, and M J Steggerda. "Inter-observer variation in delineation of bladder and rectum contours for brachytherapy of cervical cancer". *Radiotherapy and Oncology* 56.1 (2000), pp. 37–42.

[175]   H S Sakhalkar and M Oldham. "Fast, high-resolution 3D dosimetry utilizing a novel optical-CT scanner incorporating tertiary telecentric collimation". *Medical Physics* 35.1 (2008), pp. 101–111.

[176] H S Sakhalkar, J Adamovics, G S Ibbott, and M Oldham. "A comprehensive evaluation of the PRESAGE/optical-CT 3D dosimetry system." *Medical physics* 36.1 (2009), pp. 71–82.

[177] H S Sakhalkar, D Sterling, J Adamovics, G Ibbott, and M Oldham. "Investigation of the feasibility of relative 3D dosimetry in the Radiologic Physics Center Head and Neck IMRT phantom using Presage/optical-CT". *Medical Physics* 36.7 (2009), p. 3371.

[178] A A Schoenfeld, D Poppinga, R P Kapsch, P Jiang, and D Harder. "Magnetic fields are causing small , but significant changes of the radiochromic EBT3 film response to 6 MV photons Magnetic fields are causing small , but significant changes of the radiochromic EBT3 film response to 6 MV photons". *Phys Med Bio* 63.3 (2018), p. 035028.

[179] L J Schreiner. "Review of Fricke gel dosimeters". *Journal of Physics: Conference Series* 3 (2004), pp. 9–21.

[180] L J Schreiner. "Reviewing three dimensional dosimetry: Basics and utilization as presented over 17 Years of DosGel and IC3Ddose". *Journal of Physics: Conference Series* 847.1 (2017).

[181] L J Schreiner. "True 3D chemical dosimetry (gels, plastics): Development and clinical role". *J. Phys.: Conf. Ser* 573 (2015).

[182] M Schwab. *Encyclopedia of cancer.* Springer Science & Business Media, 2008.

[183] H Schweitzer, J W Bell, and F Wu. "Very fast template matching". *Lecture Notes in Computer Science (including subseries Lecture Notes in Artificial Intelligence and Lecture Notes in Bioinformatics)* 2353 (2002), pp. 358–372.

[184] J Seco, B Clasiee, and M Partridge. "Review on the characteristics of radiation detectors for dosimetry and imaging". *Physics in Medicine and Biology* 59.20 (2014), R303–R347.

[185] A Sibtain, A Morgan, and N MacDougall. *Physics for Clinical Oncology (Radiotherapy in Practice)*. 1 edition. OUP Oxford, 2012.

[186] T A Simon, J Kozelka, W E Simon, D Kahler, J Li, and C Liu. "Characterization of a multi-axis ion chamber array". *Medical Physics* 37.11 (2010), pp. 6101–6111.

[187] P S Skyt, J B B Petersen, E S Yates, P R Poulsen, T L Ravkilde, P Balling, and L P Muren. "Dosimetric verification of complex radiotherapy with a 3D optically based dosimetry system: Dose painting and target tracking". *Acta Oncologica* 52.7 (2013), pp. 1445–1450.

[188] K Smit, J G M Kok, J J W Lagendijk, and B W Raaymakers. "Performance of a multi-axis ionization chamber array in a 1.5 T magnetic field." *Physics in medicine and biology* 59.7 (2014), pp. 1845–55.

[189] K Smit, B van Asselen, J G M Kok, a H L Aalbers, J J W Lagendijk, and B W Raaymakers. "Towards reference dosimetry for the MR-linac: magnetic field correction of the ionization chamber reading." *Physics in medicine and biology* 58.17 (2013), pp. 5945–57.

[190] R L Smith, K Lechleiter, K Malinowski, D M Shepard, D J Housley, M Afghan, J Newell, J Petersen, B Sargent, and P Parikh. "Evaluation of Linear Accelerator Gating With Real-Time Electromagnetic Tracking". *International Journal of Radiation Oncology Biology Physics* 74.3 (2009), pp. 920–927.

[191] J Son, T Baek, B Lee, D Shin, S Y Park, J Park, Y K Lim, Se Byeong Lee, Jooyoung Kim, and Myonggeun Yoon. "A comparison of the quality assurance of four dosimetric tools for intensity modulated radiation therapy". *Radiology and Oncology* 49.3 (2015), pp. 307–313.

[192] C K Spindeldreier, O Schrenk, A Bakenecker, I Kawrakow, L Burigo, C P Karger, S Greilich, and A Pfaffenberger. "Radiation dosimetry in magnetic fields with Farmer-type ionization chambers: Determination of magnetic field correction factors for different magnetic field strengths and

field orientations". *Physics in Medicine and Biology* 62.16 (2017), pp. 6708–6728.

[193] J Sun, J Dowling, P Pichler, F Menk, D Rivest-Henault, J Lambert, J Parker, J Arm, L Best, J Martin, J W Denham, and P B Greer. "MRI simulation: End-to-end testing for prostate radiation therapy using geometric pelvic MRI phantoms". *Physics in Medicine and Biology* 60.8 (2015), pp. 3097–3109.

[194] M B Tacke, S Nill, A Krauss, and U Oelfke. "Real-time tumor tracking: Automatic compensation of target motion using the Siemens 160 MLC". *Medical Physics* 37.2 (2010), pp. 753–761.

[195] R Thiyagarajan, A Nambiraj, S N Sinha, G Yadav, A Kumar, V Subramani, and Kothandaraman. "Analyzing the performance of ArcCHECK diode array detector for VMAT plan". *Reports of Practical Oncology and Radiotherapy* 21.1 (2016), pp. 50–56.

[196] A Thomas, M Niebanck, T Juang, Z Wang, and M Oldham. "A comprehensive investigation of the accuracy and reproducibility of a multitarget single isocenter VMAT radiosurgery technique". *Med Phys* 40.12 (2013), p. 1217251.

[197] A Thomas, J Newton, J Adamovics, and M Oldham. "Commissioning and Benchmarking a 3D Dosimetry System for Clinical Use". *Medical Physics* 38.6 (2011), p. 3817.

[198] R H N Tijssen, M E P Philippens, E S Paulson, M Glitzner, B Chugh, A Wetscherek, M Dubec, J Wang, and U A van der Heide. "MRI commissioning of 1.5T MR-linac systems a multi-institutional study". *Radiotherapy and Oncology* 132 (2019), pp. 114–120.

[199] J Uh, T E Merchant, Y Li, X Li, and C Hua. "MRI-based treatment planning with pseudo CT generated through atlas registration". *Med Phys* 41.5 (2014), pp. 1–8.

[200] S Uilkema, U van der Heide, J J Sonke, M Moreau, B van Triest, and J Nijkamp. "A 1 . 5 T transverse magnetic field in radiotherapy of rectal cancer : Impact on the dose distribution". *Med Phys* 42.12 (2015), pp. 7182–9.

[201] J Vandecasteele and Y De Deene. "Evaluation of radiochromic gel dosimetry and polymer gel dosimetry in a clinical dose verification". *Physics in Medicine and Biology* 58.18 (2013), pp. 6241–6262.

[202] A K Vidovic, T Juang, S Meltsner, J Adamovics, J Chino, B Steffey, O Craciunescu, and M Oldham. "An investigation of a PRESAGE® in vivo dosimeter for brachytherapy". *Physics in Medicine and Biology* 59.14 (2014), pp. 3893–3905.

[203] J H W de Vries, E Seravalli, A C Houweling, S J Woodings, R Van Rooij, J W H Wolthaus, J J W Lagendijk, and B W Raaymakers. "Characterization of a prototype MR-compatible Delta4 QA system in a 1.5 tesla MR-linac". *Phys Med Bio* 63.2 (2018), 02NT02.

[204] Y Watanabe. "Derivation of linear attenuation coefficients from CT numbers for low-energy photons". *Phys Med Bio* 44 (1999), pp. 2201–2211.

[205] S Webb. "The physical basis of IMRT and inverse planning". *British Journal of Radiology* 76.910 (2003), pp. 678–689.

[206] S Webb. *The Physics of Medical Imaging.* 2nd Editio. Taylor & Francis, 2012.

[207] J Weygand, C D Fuller, G S Ibbott, A S R Mohamed, Y Ding, J Yang, K P Hwang, and J Wang. "Spatial precision in magnetic resonance imaging-guided radiation therapy: The role of geometric distortion". *International Journal of Radiation Oncology Biology Physics* 95.4 (2016), pp. 1304–1316.

[208] D Winkel, G H Bol, P S Kroon, B Van Asselen, S S Hackett, A M Werensteijn-honingh, M P W Intven, W S C Eppinga, R H N Tijssen, L G W Kerkmeijer, H C J De Boer, S Mook, G J Meijer, J Hes, M

Willemsen-bosman, E N De Groot-van Breugel, I M Jürgenliemk-schulz, and B W Raaymakers. "Adaptive radiotherapy : The Elekta Unity MR-linac concept". *Clinical and Translational Radiation Oncology* 18 (2019), pp. 54–59.

[209]   J G Wolodzko, C Marsden, and A Appleby. "CCD imaging for optical tomography of gel radiation dosimeters". *Medical Physics* 26.11 (1999), pp. 2508–2513.

[210]   W Woon, P B Ravindran, P Ekanayake, S Vikraman, Y Y F Lim, and J Khalid. "A study on the effect of detector resolution on gamma index passing rate for VMAT and IMRT QA". *Journal of Applied Clinical Medical Physics* 19.2 (2018), pp. 230–248.

[211]   U J Yeo, M L Taylor, L Dunn, T Kron, R L Smith, and R D Franich. "A novel methodology for 3D deformable dosimetry". *Medical physics* 39.4 (2012), pp. 2203 –2213.

[212]   H Zhen, B E Nelms, and W A Tomé. "Moving from gamma passing rates to patient DVH-based QA metrics in pretreatment dose QA". *Medical Physics* 38.10 (2011), pp. 5477–5489.

Appendix A

PRESAGEⓇ *Formulations*

Table A.1: Composition of batches/*Formulations* used in chapter 4

	Batch 1	Batch 2
Solvent name (s) and wt/wt %	Cyclohexanone/Dibutylphthalate/DMSO (5/10/2)	Acetone/Dibutylphthalate/DMSO (5/10/2)
Leucodye	2% 2,4 DiMeLMG-DEA	2% 2,4 DiMeLMG-DEA
Initiator	0.85%	0.85%
Polyurethane	BJB 782	BJB 782
Diameter dosimeters	2cm	2cm

Table A.2: Composition of *Formulation a, b, c, d* (chapter 5) and *e* (chapter 6).

	Formulation *a*	Formulation *b, c* and *d*	Formulation e
Solvent name (s) and wt/wt %	2% DCM / 1% Toluene	10%, 15%, 20% Dimethylphthalate	3% Dimethylphthalate
Leucodye	1% 2-methyl LMG-DEA	1% 2,4 dimethyl LMG-DMA	1% 2,4 dimethyl LMG-DMA
Initiator	0.4% CBr4	0.4% CBr4	0.4% CBr4
Polyurethane	BJB - 782	BJB - 782	BJB - 782
Diameter dosimeters	3.5 cm	3.5 cm	6 cm

Appendix B

Conferences and publications

B.1 Journal paper and conference proceedings

F Costa, S.J. Doran, I.M. Hanson, S. Nill, I. Billas, D. Shipley, S. Duane, J.Adamovics, and U. Oelfke (2018). "Investigating the effect of a magnetic field on dose distributions at phantom-air interfaces using PRESAGE® 3D dosimeter and Monte Carlo simulations". Physics in Medicine and Biology 63 05NT01.

Oral Presentation at the 9th International Conference on 3D Radiation Dosimetry (IC3DDose), November 2016. Texas, USA, November 2016:

F Costa, S.J. Doran, S. Nill, S. Duane, D. Shipley, I. Billas, J.Adamovics, and U. Oelfke (2017). "Development of a methodology to study the effect of magnetic field on dose distributions in an MR-linac, using and Monte Carlo calculations". Journal of Physics: Conference Series 847, p012058. [Best Student Paper award]

Oral Presentations at the 10th International Conference on 3D Radiation Dosimetry (IC3DDose), September 2018. Kunshan, China, September 2018:

F Costa, S J Doran, J Adamovics, S Nill, I M Hanson, U Oelfke (2019). Characterization of small PRESAGE® samples for measurements near the dosimeter edges". Journal of Physics: Conference Series 1305, p. 012009. [Best Student Paper award]

F Costa, M J Menten, S J Doran, J Adamovics, I M Hanson, S Nill, U Oelfke (2019). Dose verification of dynamic MLC-tracked radiotherapy using small PRESAGE® 3D dosimeters and a motion phantom. IOP Conf. Series: Journal of Physics: Conf. Series 1305, p. 012068.

Other collaborations in the field of 3D dosimetry: **Costa, F**, E Kousi, A Gasnier, E Wells, C Lamb, M A Schmidt, R Moore "Verification of stereotactic cranial radiotherapy treatments with MR-based gel dosimeters : practical aspects". OP Conf. Series: Journal of Physics: Conf. Series 1305, p. 012025.

B.2   Conference presentations

Poster oral presentation at the 5th Magnetic Resonance in Radiation Therapy Symposium (MRinRT), June 2017. Sydney, Australia, June 2017.

F Costa, I M Hanson, S J Doran, S Nill, I Billas, D Shipley, S Duane, J Adamovics, U Oelfke. "Investigate the use of PRESAGE® 3D dosimeter as a QA tool for an MR-linac"

Oral presentation at the AAPM Annual Meeting 2018. Tennessee, USA.

F Costa, M J Menten, S J Doran, J Adamovics, I M Hanson, S Nill, U Oelfke. "Use of Small 3D Radiochromic Dosimeters and a Motion Phantom for Dose Verification of Dynamic MLC Tracking Radiotherapy."

Poster oral presentation at ESTRO 38, April 2019. Milan, Italy.

F Costa, I M Hanson, S Doran, J Adamovics, S Nill, U Oelfke. "Dosimetric verification of Elekta MR-linac adaption workflow using 3D dosimeters"